

# 2017

## Annual Report Jahresbericht

### Remote Sensing Technology Institute

Department  
Atmospheric Processors



**Published by** **German Aerospace Center (DLR)**  
A member of the Helmholtz Association

**Remote Sensing Technology Institute**  
Institut für Methodik der Fernerkundung (IMF)

Department  
**Atmospheric Processors (IMF-ATP)**

**Department Head** Prof. Dr. Thomas Trautmann

**Editorial Team** Prof. Dr. Thomas Trautmann  
Dr. Manfred Gottwald  
Dr. Franz Schreier

**Layout** Dr. Manfred Gottwald

**Cover** Mosaic of sulfur dioxide (SO<sub>2</sub>) plumes from the Ambae volcanic eruption on the archipelago of Vanuatu over the period November 8-13, 2017 (see chapter 4.1).

## Contents

<b>2.</b>	<b>Atmospheric Remote Sensing – Missions and Sensors</b> .....	<b>5</b>
2.1	Sentinel-5 Precursor Level 2 Project.....	5
2.2	Sentinel-4 and the Sentinel-4 Level 2 Project.....	8
2.3	SCIAMACHY Processor Updates .....	10
2.4	Calibration Data Handling in Level 0-1 Processing .....	14
2.5	Remote Sensing from High Altitude Platforms .....	18
2.6	Retrieval of Aerosol Profiles from the MAX-DOAS Measurement at the UFS .....	20
<b>3.</b>	<b>Atmospheric Remote Sensing – Methods</b> .....	<b>25</b>
3.1	Operational Atmospheric Composition SAF Trace Gas Column Products from GOME-2 .....	25
3.2	Improvement of Total and Tropospheric NO <sub>2</sub> Column Retrieval for GOME-2.....	26
3.3	OCRA Cloud Fractions for GOME-2 and TROPOMI – Imager Resolution Capabilities .....	28
3.4	Double-cloud Layer Presence in the Cloud Parameters Retrieved from ROCINN .....	30
3.5	CO Total Column Retrievals from SCIAMACHY.....	32
3.6	Estimating Ground Level NO <sub>2</sub> Concentrations from Satellite Observations .....	36
3.7	Aeolus Mie and Rayleigh Algorithm Performance Assessment .....	38
3.8	VirES for Aeolus .....	40
3.9	Linearized Radiative Transfer Model for the Retrieval of Cloud Properties from DSCOVER-EPIC .....	41
3.10	UPAS-2 Parallelization Concept.....	43
3.11	Estimating Ozone Profile Shapes from GOME-2 Measurements using FP-ILM .....	45
3.12	Stochastic Radiative Transfer Models .....	47
3.13	Intercomparison of 3 Microwave/Infrared High Resolution LbL Radiative Transfer Codes.....	49
3.14	Atmosphere-water Coupled Radiative Transfer – Actual Status of Validation .....	51
3.15	Sound Scattering on Bispheres.....	52
<b>4.</b>	<b>Atmospheric Remote Sensing – Applications</b> .....	<b>55</b>
4.1	First Results: SO <sub>2</sub> Emissions Detected by Sentinel-5 Precursor .....	55
4.2	The GOME-type Total Ozone Essential Climate Variable .....	59
4.3	The Textbook “Green’s Functions in Classical Physics” .....	61
4.4	Exoplanet Transit Spectroscopy with the ACE-FTS Infrared Spectral Atlas of Earth.....	62
4.5	Molecular-Level Computational Astrobiology at ELSI .....	65
<b>5.</b>	<b>Documentation</b> .....	<b>67</b>
5.1	Books.....	67
5.2	Journal Papers.....	67
5.3	Conference Presentations.....	68
5.4	Attended Conferences .....	70
5.5	Academic Degrees.....	71
	<b>Annex: Abbreviations and Acronyms</b> .....	<b>73</b>



## 1. Foreword

2017 was the beginning of what we hope will be the “Golden Decade” for space-borne atmospheric sounding. On October 13, 2017, Sentinel-5 Precursor with the TROPOMI sensor aboard lifted off from the launch pad at the Plesetsk Cosmodrom, atop a Rockot launcher. TROPOMI’s very high spatial resolution will usher our research field in a new phase. And in the coming years we will see more than a handful new instruments, some with unprecedented capabilities, for the purpose of monitoring and understanding our atmosphere from space.

In reports for the previous years we often described how we prepared for those missions. This time, the first results of Sentinel-5 Precursor can be shown. They illustrate that our expectations were indeed not unrealistic. Where sensors from the pre-Sentinel era covered the ground swath with pixels of considerable size, Sentinel-5 Precursor allows detailed views of trace gas and cloud distributions. Once the commissioning phase will have been successfully accomplished, a continuous stream of raw data will feed our processing systems to yield the specified high-quality geophysical products.

Our experts for radiative transfer and retrievals have meanwhile adapted the theoretical foundations to cope with new challenges while our software engineers cast the resulting algorithms into efficient processing systems. Even though, as the data pour in and new requirements will emerge, the initial Sentinel-5 Precursor results demonstrate that we have achieved the first step of being ready for the next generation atmospheric missions.

The start of the phase E activities of Sentinel-5 Precursor was an important milestone for us. We hope that we can add more and more of such achievements to our records in the coming years. They are only possible with the high dedication of the people involved.

We like to thank our staff for these efforts in the past year and their contributions to the present report.

Prof. Dr. Thomas Trautmann  
Dr. Manfred Gottwald

Up and away. Lifting space-borne atmospheric sounding to new heights – the launch of Sentinel-5 Precursor (Photo: ESA / S. Corvaja).





## 2. Atmospheric Remote Sensing – Missions and Sensors

### 2.1 Sentinel-5 Precursor Level 2 Project

*D. Loyola, P. Hedelt, and the S5P-Team*

The first scientific-technical chapter of our annual report continues what the foreword has already addressed – the start of the Sentinel-5 Precursor's (S5P) in orbit phase on October 13, 2017 and how we are involved in this groundbreaking undertaking. Its importance for us cannot be overstated; it is the beginning of the new era on atmospheric composition measurements from space where the Copernicus Sentinels will provide worldwide unprecedented capabilities for monitoring the state of the Earth's atmosphere.



Fig. 2-1: Artist's impression of the moment when Sentinel-5P atop the Rocket launcher reaches space (image: ESA).

The Tropospheric Monitoring Instrument (TROPOMI) is the only payload aboard of S5P. It is conceived as a partnership between ESA and Dutch Space, KNMI, SRON and TNO, on behalf of NSO. TROPOMI is a spaceborne nadir viewing spectrometer with bands in the ultraviolet and visible (270-495 nm), the near infrared (675-775 nm) and the shortwave infrared (2305-2385 nm). TROPOMI combines daily global coverage with a high spatial resolution of  $3.5 \times 7 \text{ km}^2$  for focusing on the troposphere where concentrations of trace gas and aerosol species rapidly change.

The superior spatial resolution is one of the big assets of TROPOMI when compared with the present sensor generation as represented by GOME-2 on the MetOp platforms where ground pixels are larger by two orders of magnitude (see also chapters 3.3 and 4.1).

TROPOMI delivers 20 million measurements every day, equivalent to a data volume increase of a factor  $\sim 100$  compared with GOME-2 (Fig. 2-2). In 2017, and before, we had worked very successfully on the second generation of the UPAS level 2 (L2) processor suite to master this Big Data challenge by significantly speeding up all the retrieval routines (DOAS fit, optimal estimation inversion, etc.) and additionally taking full advantage of multiprocessor parallelization using OpenMP. Moreover the very complex interfaces with the usually time consuming radiative transfer models like LIDORT were generalized and optimized for the processing of data from all Copernicus atmospheric sensors.

#### ***S5P geophysical products***

Presently S5P delivers level 2 products for ozone ( $\text{O}_3$ ),  $\text{NO}_2$ , sulfur dioxide ( $\text{SO}_2$ ), formaldehyde (HCHO), carbon monoxide (CO), methane ( $\text{CH}_4$ ), as well as UV, cloud and aerosol properties. The work on these products is funded by ESA together with national contributions from The Netherlands, Germany, Belgium and Finland. DLR is tasked with a subset of the products mentioned above, namely ozone ( $\text{O}_3$  – total and tropospheric), sulfur dioxide ( $\text{SO}_2$ ), formaldehyde (HCHO) and cloud properties such as fraction, top pressure and optical thickness. They are produced with the second generation of UPAS which is integrated in the S5P Payload Data Ground Segment (PDGS) system developed and operated at DLR-DFD.

The commission phase, of 6 months duration, aims at bringing the spacecraft and the instrument to full functionality and adjust, where necessary the in-orbit operations and sub-system settings. Meanwhile the S5P ground segment processes the incoming measurement data on a regular basis. Our share is made available via <https://atmos.eoc.dlr.de/>. It reflects the current settings of the instrument and the processor configuration. The excellent performance of the UPAS processor suite was demonstrated shortly after the first TROPOMI level 1b (L1b) data became available. ESA presented the first images of

Sentinel-5 Precursor during an event that took place at DLR on December 1, 2017, only a few weeks after the satellite launch. Even though TROPOMI and the L1b products are not fully calibrated the early commissioning phase results already illustrated the quantum leap which will be achieved in atmospheric composition monitoring by S5P.

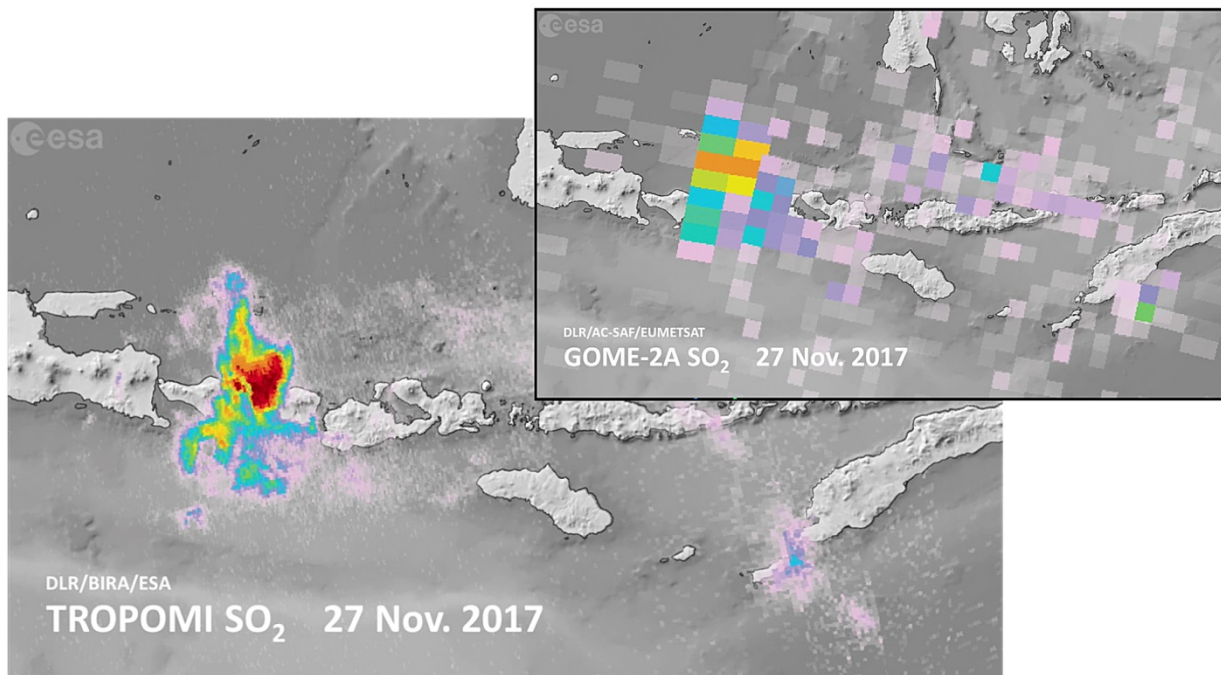


Fig. 2-2: SO<sub>2</sub> from the Mt. Agung volcanic eruption measured on November 27, 2017 by TROPOMI/Sentinel-5 Precursor with its superior spatial resolution. The top inset shows in comparison the GOME-2/MetOp-A measurements. TROPOMI takes 20 million measurements per day, i.e. it produces factor 100 more data than GOME-2.

Fig. 2-3 illustrates the S5P level 2 products from December 28, 2017 under the responsibility of our department and generated with UPAS. Immediately obvious is the wide swath of TROPOMI which permits a global coverage within a single day. Fine detail can be discerned on these timescales already, most noticeable for the cloud properties and for SO<sub>2</sub> where faint plumes from volcanic eruptions can be seen at the west coast of South America, over the Caribbean and in the South Pacific.

### **ESA Projects and DLR role**

The development of S5P retrieval algorithms and operational processors at DLR is being funded via national and ESA projects. ESA/ESTEC initiated the S5P level 2 working group (L2WG). The L2WG, co-lead by KNMI and DLR, coordinates the scientific work needed for developing and validating the retrieval algorithms, and the engineering work required for developing the operational processors and integrating them into the Payload Data Ground Segment (PDGS). The successful work of L2WG was demonstrated not only during the developing phase, but also with the arrival of the first (not fully calibrated) TROPOMI L1b data. All products under DLR responsibility were available from the beginning of the mission. The L2WG and the related ESTEC project will finish with the S5P commissioning phase planned for April 2018. ESA/ESRIN is responsible for the S5P Mission Performance Center (MPC) that will cover the full satellite operation time of at least seven years. KNMI coordinates the overall MPC project whereas DLR coordinates the level 2 Expert Support Laboratories (L2 ESL) responsible for monitoring the quality of the L2 products, further development of the retrieval algorithms and updates of the operational processors.

After the end of the S5P commissioning phase, the TROPOMI L1b and the operational L2 products will be released to the public following the Copernicus open access and free data policy.

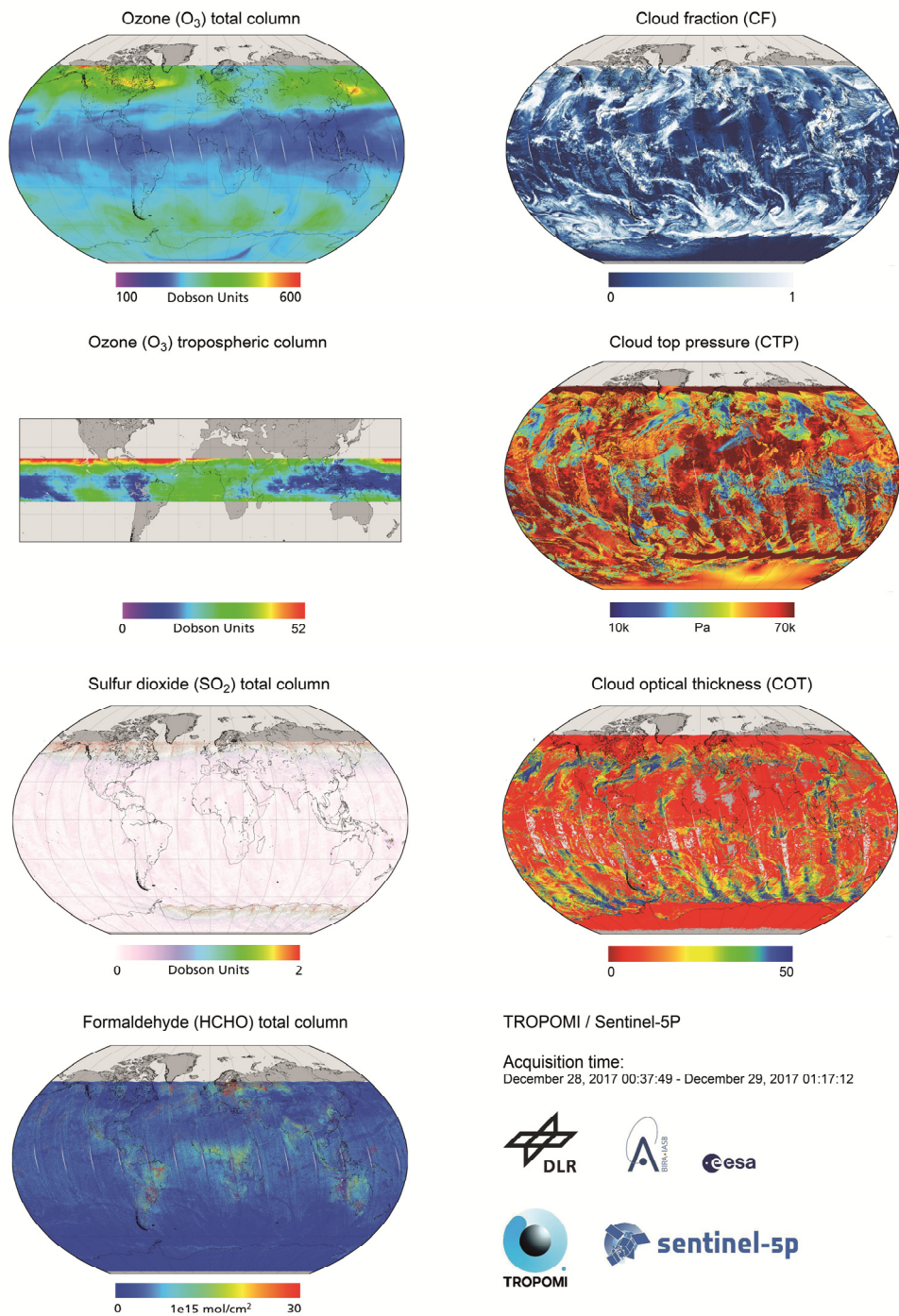


Fig. 2-3: The S5P geophysical product portfolio under the responsibility of DLR. The global trace gas and cloud maps are retrieved from a single day of TROPOMI measurements.

## 2.2 Sentinel-4 and the Sentinel-4 Level 2 Project

*D. Loyola, R. Lutz, M. Pedernana, and the S4-Team*

### **Sentinel-4**

The recent launch of Sentinel-5 Precursor (S5P) in October 2017 was the first of the next generation of atmospheric remote sensing missions. Sentinel-4 (S4) and Sentinel-5 (S5) will follow in a few years. These Copernicus Sentinels are dedicated to trace gas and air quality monitoring with unprecedented accuracy and spatial resolution. The S4 mission with its UVN instrument is particularly interesting because it will be the first atmospheric composition sensor in a geostationary orbit providing hourly measurements of the air quality over Europe.

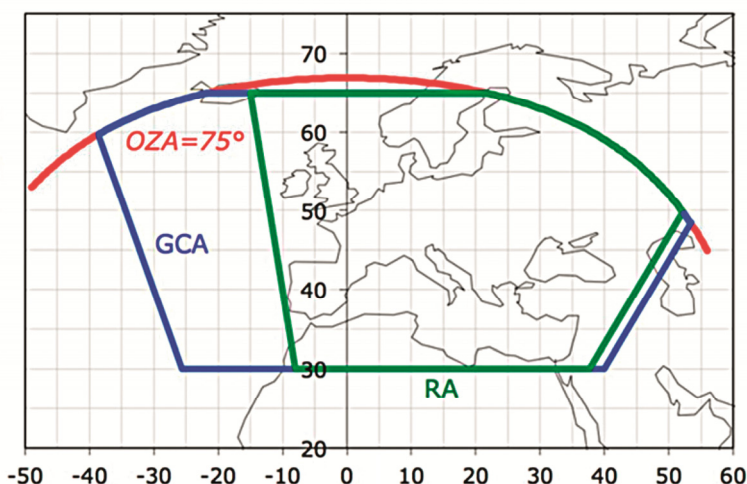


Fig. 2-4: Sentinel-4 geographic coverage area (GCA), reference area (RA) and limiting observation zenith angle (OZA) (image: ESA).

Sentinel-4 will be carried on EUMETSAT's Meteosat Third Generation Sounder (MTG-S) platform with an anticipated first launch around 2022 and a second in 2029. The S4 spatial coverage focused on central Europe (Fig. 2-4 and 2-5) with a high spatial ( $8 \times 8 \text{ km}^2$ ) and moderate spectral (0.12-0.5 nm) resolution. The UVN instrument covers the UV/VIS spectral region (305-500 nm) as well as the NIR region (750-775 nm). This setup will allow to study in more detail the diurnal variation of the important atmospheric constituents  $\text{O}_3$ ,  $\text{SO}_2$ ,  $\text{NO}_2$ , HCHO, CHOCHO, together with cloud-, aerosol-, and surface properties (Table 2-1).

Product	Threshold	Goal
$\text{O}_3$ total column	4%	3%
Tropospheric $\text{O}_3$	40%	25%
Tropospheric $\text{NO}_2$	troposphere 50 %	troposphere $1.5 \cdot 10^{15} \text{ molec/cm}^2$ or 30%
$\text{SO}_2$	total column 100%	total column $1.0 \cdot 10^{16} \text{ molec/cm}^2$ or 80 %
HCHO	total column 100%	total column $1.5 \cdot 10^{16} \text{ molec/cm}^2$ or 50%
CHOCHO	n/a	total column $7.0 \cdot 10^{14} \text{ molec/cm}^2$ or 50%
Aerosol properties	1 km (ALH), 0.5 (Index), 0.05 (AOD)	n/a, 0.3 (Index), n/a
Cloud properties	20% (CF), 1 km (CTH), 30% (COT)	10% (CF), 0.5 km (CTH), 20% (COT)
Surface	0.01 (first BRDF parameter)	n/a

Table 2-1: Sentinel-4 level 2 operational products and expected threshold and goal performances.

Obtaining trace gas measurements over Europe each hour will help understanding rapidly varying photochemical processes that affect and control the atmospheric composition. A better understanding of these processes and timely measurements are also a crucial precondition for an accurate data-assimilation based monitoring and forecasting, e.g. within the framework of the Copernicus Atmosphere Monitoring Service (CAMS).

### **Sentinel-4 Level 2 project**

DLR leads the ESA funded S4 level 2 project initiated in June 2015 (S4L2). This project includes the commissioning phase of the first MTG-S satellite and comprises the development of the prototype algorithms, scientific verification and ultimately the operational processors for all products mentioned in Table 2-1. The overall project coordination has been assigned to DLR, leading an international consortium of experts in the fields of algorithm development, independent verification and processor development for the retrieval of trace gases. These expert groups include the Rutherford Appleton Laboratory (RAL, UK), responsible for coordinating the algorithm bread-boarding activities and the Max-Planck Institute for Chemistry (MPIC, D) tasked with the coordination of the independent verification. DLR, on top of our overall coordination role, also coordinates the processor suite activities of the various processor teams.

The remaining expert groups contributing to algorithm and processor development are in Belgium the Belgian Institute for Space Aeronomie (BIRA-IASB) and Rayference, the University of Lille in France (LOA), Catalysts Austria, the University of Bremen (IUP-IFE), the Royal Dutch Meteorological Institute (KNMI) and S&T Norway.

The S4L2 project successfully passed the preliminary design review (PDR) in summer 2017. Since then three contract change notes were activated by ESA for the generation of scientifically realistic level 0 test datasets, extending CHOCHO as a full product and adding a pre-processing step for optimally handling auxiliary data, and adapting the processor interfaces following the agreement reached between ESA and EUMETSAT.

After developing the Sentinel-4 level 2 bread-boarding algorithms, independent verification algorithms and prototype processors in an L2PP prototype environment (L2 Prototype Processor), the operational L2OP (L2 Operational Processor) will ultimately be integrated into the MTG L2 Processing Facility (MTG L2PF) at EUMETSAT. The main challenges for the retrieval algorithms are the extreme viewing conditions induced by the geostationary orbit and the proper handling of the continuous changes in surface and atmospheric properties. A particular challenge for the processors is to fulfill the strict timeliness requirements, i.e. to provide the level 2 data in near-realtime. From the total budget of 3 hours for the whole processing chain, only about 40 minutes remain for the level 1b to level 2 processing. In order to cope with these high demands, novel retrieval techniques are being developed and/or implemented such as, e.g. multi-core parallelization, optimized inversion schemes, and machine learning techniques including neural networks and smart sampling.

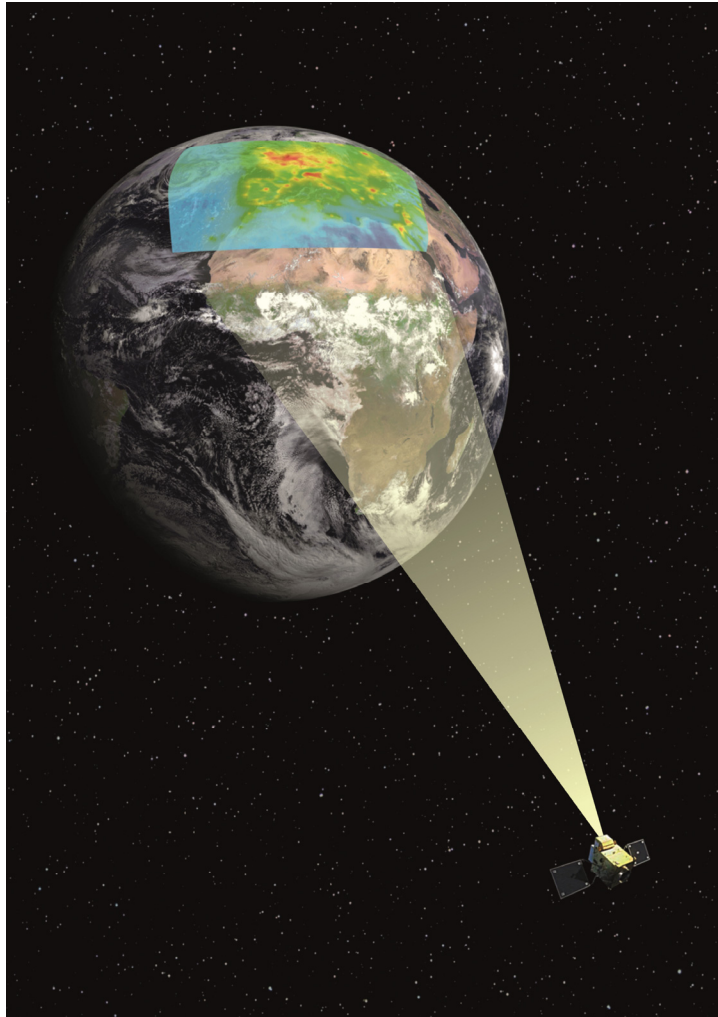


Fig. 2-5: Artist's view of Sentinel-4 with Europe in its field of view.

## 2.3 SCIAMACHY Processor Updates

*G. Lichtenberg, B. Aberle, A. Doicu, M. Hamidouche, S. Gretschan, P. Hochstaffl, M. Meringer, F. Schreier, S. Slijkhuis*

In the past year the new level 0-1b and level 1b-2 processors were verified and tested. This involved not only a test of the algorithm implementation but also testing if the processing chains work correctly with the new format.

We implemented the following changes in the level 1 processor:

- improved degradation correction using a model from SRON (*Krijger et al. 2014*)
- updated misalignment angles from in-flight calculations by IUP-IFE
- complete overhaul of the polarisation calculation using updated algorithms from IUP-IFE and IMF
- update of the dark correction in channel 8 thus improving especially the correction of the orbital variance (SRON)

Most of the changes had already been implemented in 2016 with the verification finished in 2017. The level 2 processor had two updates. The main addition was a new tropospheric BrO product based on a BIRA-IASB algorithm. The limb cloud algorithm was updated with improved parameters. In addition to the algorithmic changes, together with the SQWG we had developed a new data format for level 1 and level 2 data. The current format is still based on the original ENVISAT format and the user needs custom readers to access the data. This not only hampers the general use of the data but non-standard formats also pose a risk for long-term usage. Thus a new netCDF format had been drafted by us.

### **Test chain**

The wealth of modifications required a comprehensive test and verification scheme. Therefore we defined a test chain for the purpose to separate pure implementation issues, e.g. bugs, use of different libraries or even programming languages from effects of the new format and in case of the level 2 testing from the updated level 1 input product (Fig. 2-6). This chain included the following steps:

<i>Level 1 verification</i>	Check each changed algorithm against the reference algorithm.
<i>Level 2 verification step 1</i>	Check each changed algorithm against the reference algorithm, using the level 1 from the currently operational processor (V8).
<i>Regression test level 1 &amp; 2 (not shown)</i>	Test all unchanged algorithms if they still deliver the same result to exclude side effects.
<i>Level 2 verification step 2</i>	Compare the results of all algorithms using level 1 V8 and the new level 1 V9.
<i>Format check level 1</i>	Check if the netCDF file content is correct by comparing it to the verified ENVISAT level 1 product or an independent implementation in case the data were not part of the ENVISAT format.
<i>Format check level 2</i>	Check if the level 2 processor delivers the same result as the processing chain using the old ENVISAT format, when using level1 netCDF as input and level 2 netCDF as output.

### **The new netCDF format**

The new SCIAMACHY product format was implemented since the original ENVISAT format is neither a standard format nor is it self-descriptive. It was therefore decided to generate the products from the new processors in the netCDF format. The same format, well known in the scientific community, is also used by the Sentinel satellites in the Copernicus program. It is readable by standard tools which are readily available. The guidelines for the new product were:

- The products should have a structure similar to the Sentinel atmospheric missions (S5P, S4, S5).
- All (useful) content from the old format should be contained in the new format, i.e. information must not be lost.
- All products for SCIAMACHY (level 1b, level 1c and level 2) should be aligned as far as possible (e.g. header information).

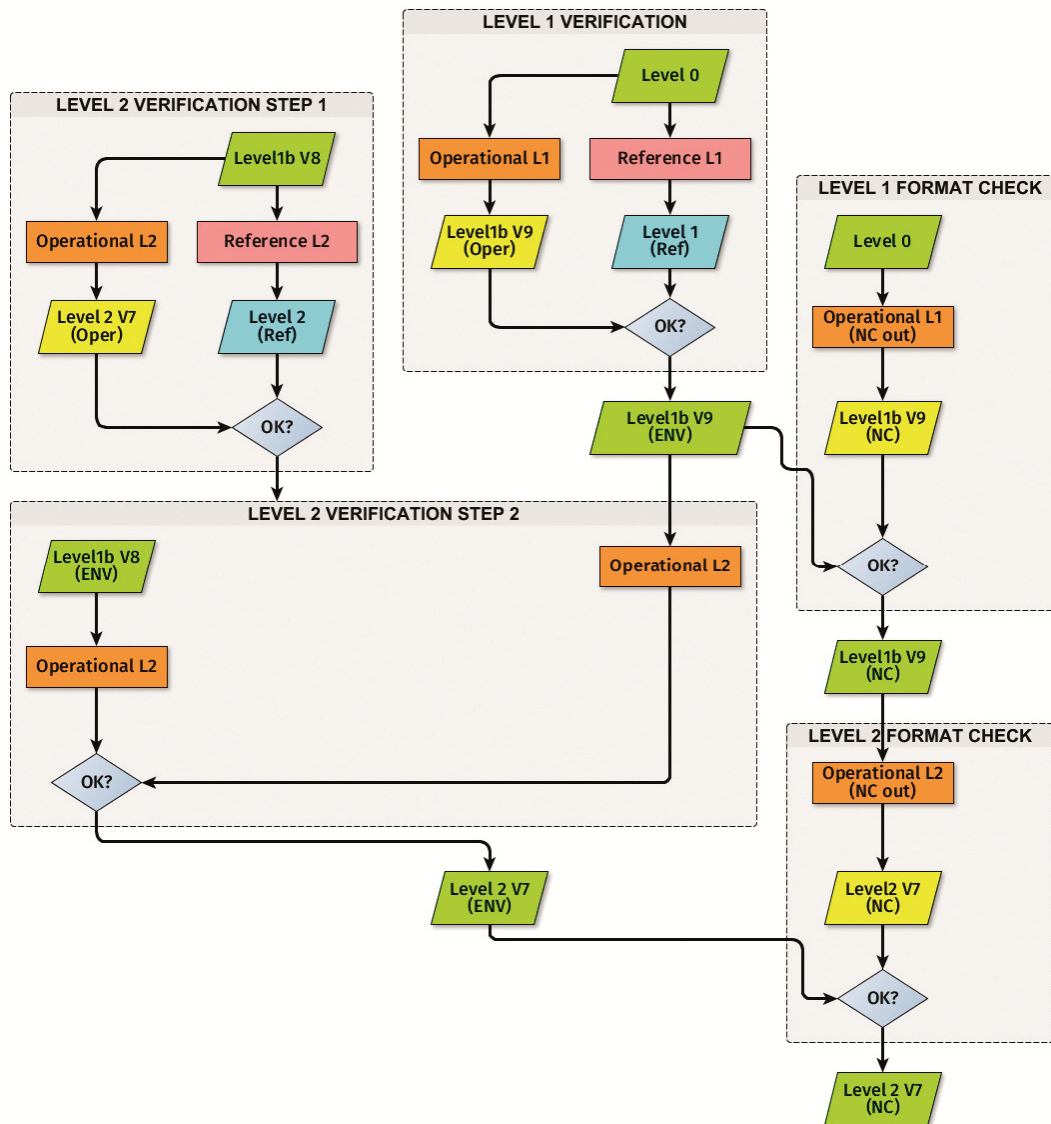


Fig. 2-6: Test chain for the level 0-1b and level 1b-2 processors, including format checks. Green shaded products are verified. ENV = ENVISAT format, NC = netCDF format. In each step two products with different origins are compared (comparisons are marked by diamonds).

SCIAMACHY observations are more complex than those of e.g. the Sentinel-5 Precursor. The observations are split up in up to 64 spectral bands, "clusters" in the SCIAMACHY terminology. The spectral bands have different integration times. Furthermore, over the orbit the integration time of a given band can change. This minimized the data rate needed for data downlink. However, it introduces a high degree of complexity to the level 1b data. In the ENVISAT format, all observations were written chronologically after each other. In the netCDF level 1b data instead, the measurements are now grouped by observation type (*nadir*, *limb*, *occultation* or *monitoring*) and then by spectral band. In a given band, all observations are now on a common grid and are stored in an array with the dimensions time x scanline x ground pixel x spectral channel with

- time = a "degenerate" dimension for SCIAMACHY that is always 1. It is used to be compatible with the Sentinel data format
- scanline = one complete cycle of forward and backward scan
- ground pixel = measurement within a scan on the ground (east to west)
- spectral channel = detector pixel

Data that are missing because of longer integration times are amended with fill values. The new format also permitted to add useful mission or sensor information. In the old format, the geolocation was only given for the minimum integration time and the user had to calculate the coordinates for larger

integration times. In the new products we provide the geolocation for each observation individually. The geolocation for the PMD measurements is also added (Fig. 2-7).

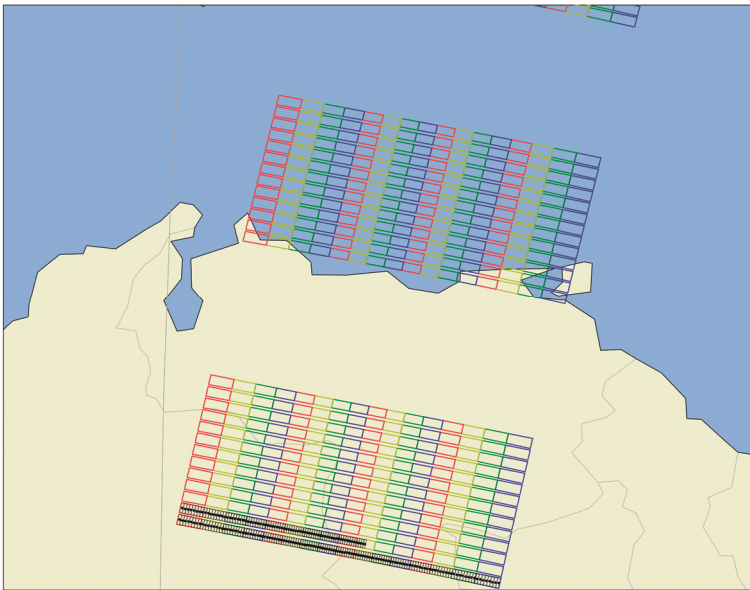


Fig. 2-7: Example for the new geolocation. Colored polygons show the extent of the ground pixel for nadir observations. In black we overplotted the extent and centre points for some PMD observations for the same nadir observation.

During the mission, information about the state of the instrument and its configuration were stored by SOST in different databases. Because with the end of Phase F also the SOST operation ends, it was decided to transfer the instrument status and configuration from the SOST databases to the level 1b files. In this way, the information is kept and available for future users.

For level 2, the overall structure of the files remained the same. The major improvement here is that important information, which was previously somewhat hidden in the field "ADDITIONAL DIAGNOSTICS" due to restrictions in the old format, now has its own netCDF variable and is easily accessible. One prominent example are the number densities for the limb profiles, which are the primary result

of the limb retrievals, but had to be extracted from the diagnostic field. The extraction was difficult because the diagnostics field contained different parameters written in sequence. Therefore complicated index operations were needed to get the number densities. In the new format, the values are directly accessible. As for the level 1 file, the level 2 file also contains now the geolocations for the individual measurements.

### **Level 1-2 feedback**

The testing of the new processor version showed again that it is essential to check the impact of a changed level 1 product on level 2 retrievals. In the new processor several improvements for the SWIR channel 8 were implemented like a new bad and dead pixel mask and a different spectral calibration. However, a comparison of the retrieved CO values using the new level 1b product yielded unrealistic results (Fig. 2-8). Since the CO retrieval algorithm itself had been unchanged, the effect must have come from the different calibration of the data and the resulting changes in the level 1 product. In a detailed investigation we varied level 1 and level 2 settings and compared the result with results from the previous level 2 processor version and also TCCON stations. This study showed that the new mask and the spectral calibration were incompatible with the retrieval algorithm. Going back to the original dead and bad pixel mask and spectral calibration gave a better result (Fig. 2-9). Other improvements for the dark correction and for the radiometric calibration could be kept. It must be emphasized, however, that these findings did not mean that original improvements were wrong; they showed instead that the level 2 retrieval algorithm responds unexpectedly to the changes in calibration. Especially for retrievals in the SWIR channel it is known that they are very sensitive to level 1 modifications.

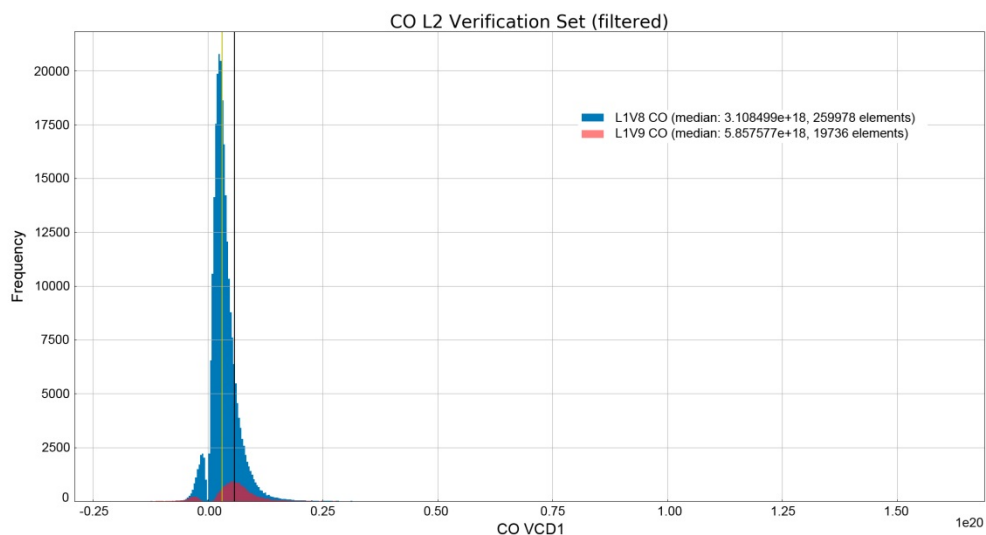


Fig. 2-8: Histogram of the CO values for the verification data set (212 orbits) using level 1 V8 (blue) and level 1 V9 (red). For the latter the number of converged retrievals has dropped by more than 90% and the retrieved values are much too high.

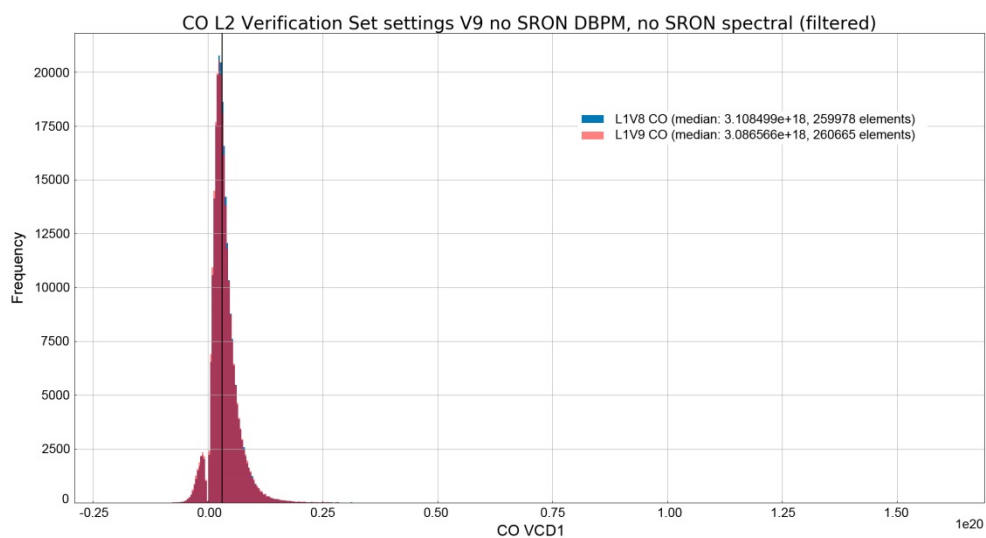


Fig. 2-8: Same as Fig. 2-8, but now using the original bad and dead pixel mask and spectral calibration for level 1 V9. The CO values and convergence rate are back to normal. The result was confirmed with a comparison against TCCON stations.

### References

*Krijger, J.M., Snel, R., van Harten, G. et al.:* Mirror contamination in space I: mirror modelling. *Atmos. Meas. Tech.*, 7, 3387-3398, 2014.

## 2.4 Calibration Data Handling in Level 0-1 Processing

*G. Lichtenberg, B. Aberle, M. Meringer, S. Slijkhuis*

The handling of calibration data can be a challenging task for level 0-1 processing. Calibration measurements will be done on time scales different from science measurements, which are usually made with the highest possible frequency. Therefore, the calibration data must be stored and tagged for later usage. The level 0-1 processor must then select the appropriate calibration data for each science measurement – typically the calibration measurement nearest to the science measurement or the most recent calibration measurement. In the processing of satellite data currently two approaches are used to store and use calibration data:

- File based storage: A given calibration parameter derived from a measurement is saved in files that are read by the calibration algorithms. Sometimes several calibration data are stored in one file.
- Database storage: All calibration data are saved in a database together with metadata that allow tracing back the data to measurements and that allow the selection of the appropriate calibration for a given Earth measurement.

### **Categorizing measurement information**

The information needed for processing can be split into four types:

- 1) Measurement Information: This is the information that can be directly derived from the individual measurements, the house keeping data of the instrument, and data of the platform. Usually this will be the detector signals, instrument parameters as far as relevant for calibration (e.g. instrument mode) and orbit position or viewing direction. Typically this information is contained in the level 0 product that serves as the primary input for level 1b processing.
- 2) Asynchronous Measurement Information: This is information that is needed for the calibration of all measurements, but does not come with the same frequency as the measurements to be processed.
- 3) External Information: This is all information that cannot be derived from the input level 0 product. Typical examples are on-ground calibration data or reference data, e.g. topographic height at the observed ground pixel.
- 4) Aggregated Information: This information can only be derived from several measurements. A typical example is the degradation of the instrument that is calculated by analyzing measurements from the begin of life and comparing them to measurements at different points in time.

Most calibration data are asynchronous or are based on aggregated information. Fig. 2-10 illustrates a simple example for the application of calibration data to Earth measurements:

- We have only one type of calibration measurement.
- The calibration measurement does not need other calibration data for a processing before deriving the calibration parameter.
- We have only one processor instance.

Each calibration measurement is used for the following Earth measurements, until the next calibration measurement comes along. This is the selection rule “most recent” that is usually applied during forward processing. The calibration measurements are processed to derive a calibration parameter (“CalPar from Cal x”), which is stored with a unique ID for later use. Earth measurements 1..... n are then read and processed using the appropriate calibration parameter, which is selected using the ID and, e.g. measurement time.

Fig. 2-11 shows an example for the data flows that must be handled by the processor for a database solution.

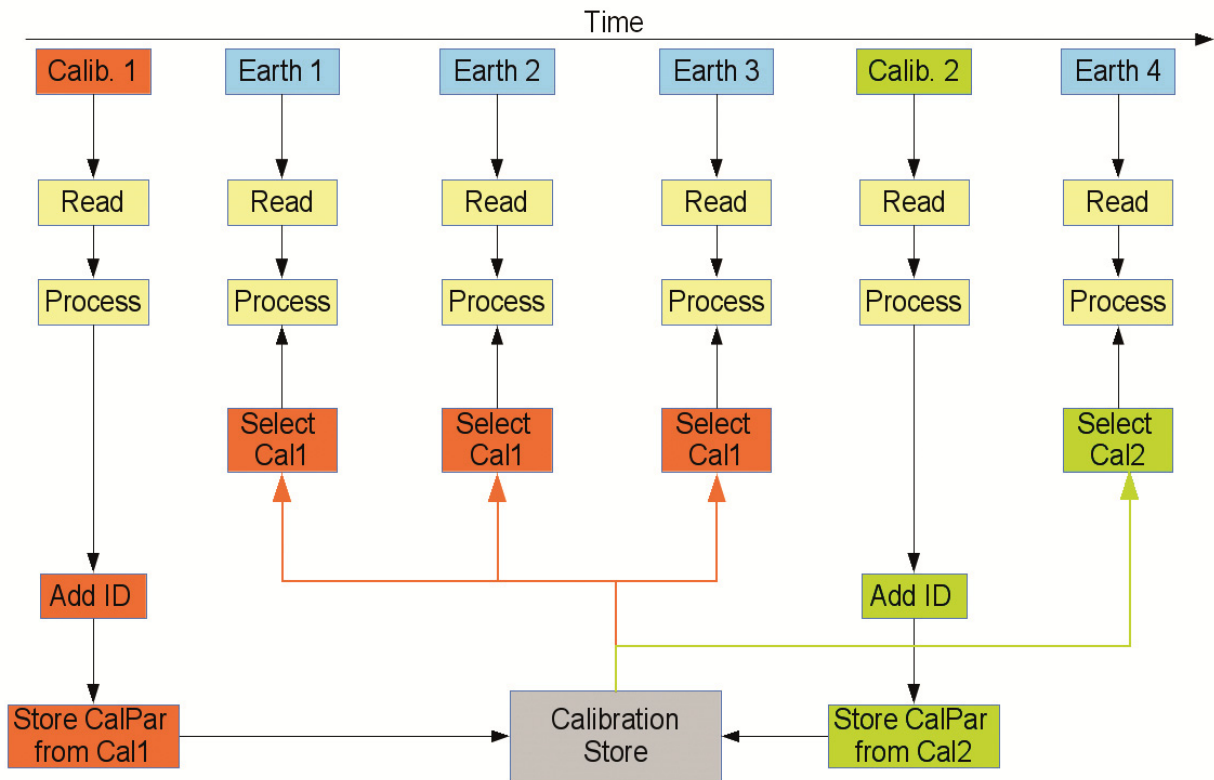


Fig. 2-10: Scheme describing the high level processing using in-flight calibration data. Note that this is the simplest possible case. Time goes from left to right. For details see text.

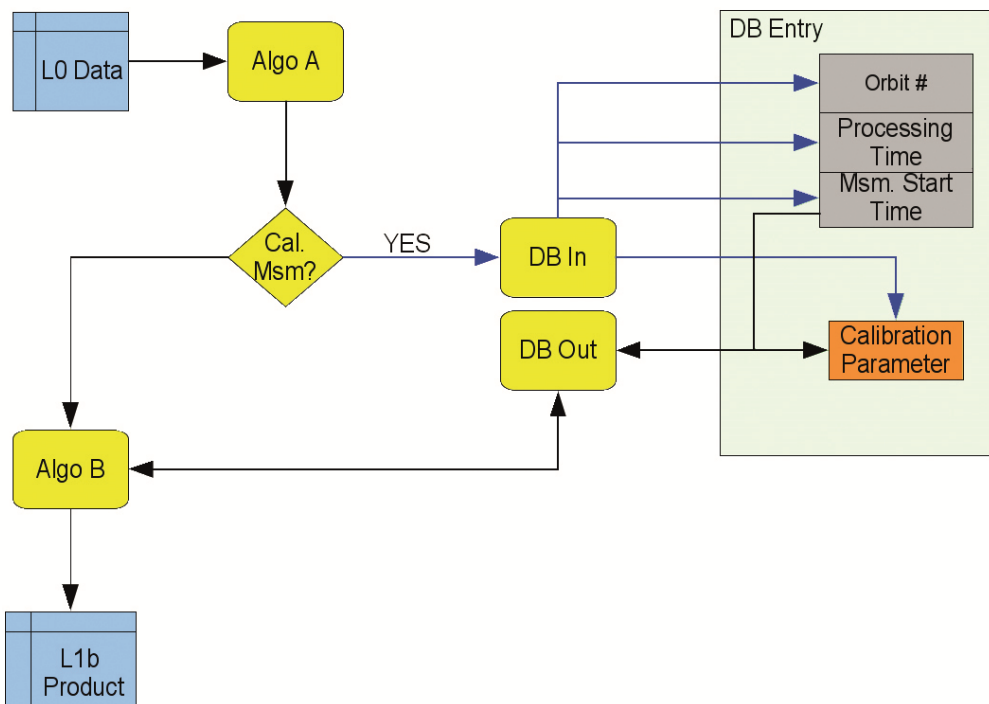


Fig. 2-11: Data flow for the case: **Algorithm A** needs no input from database, **Algorithm B** needs input. If the production unit contains a calibration measurement (dark blue arrows), data are written via the **database write** function to the database. The processor continues with **algorithm B**, which needs input from the database and communicates this to the **database read** function. The function looks up the correct parameter and time and returns it to B where it is used in processing. Note that more complicated cases might occur, e.g. an algorithm needs input from the database and also writes to the database.

### **Requirements for the calibration data handling**

In today's space-borne missions the most important requirements for the calibration data handling are *traceability* and *reproducibility*. Traceability has to ensure that all data products and their content are fully traceable. The traceability chain roughly comprises

- 1) The level 0-1 algorithm description and the instrument calibration documents describe the algorithms that are needed to be implemented.
- 2) The verification checks that all algorithms are implemented correctly.
- 3) The level 0 product contains all information to trace back the data to
  - name of the ground station
  - processor version raw  $\Rightarrow$  level 0
  - external input data used.
- 4) The level 1 product contains
  - input level 0 product name (must be unique)
  - version of the calibration on-ground data that were used
  - in-flight calibration measurements that were used identified by measurement time and processing time
  - processor version level 0-1.

Reproducibility has to ensure that a certain result (level 1 product) can be re-produced again at any time. In order to guarantee this, the following is required

- 1) Traceability information in the product that should be re-produced.
- 2) All processor elements are under full version control. Older processor versions can be re-created at any time.
- 3) Data that are generated by the different processors are never changed manually, but always by the processor.
- 4) External data that are not generated by processors are kept under tight configuration control and always follow a pre-defined approval cycle.
- 5) Input data used for the generation of a valid product must not be overwritten but must be kept. This is also important for anomaly investigations.

The last requirement might be considered optional in the sense that for the reproducibility it is not strictly needed: The regeneration of, e.g. a level 1 product then simply has to start at level 0 and go through the whole chain (including all level 0 data that were used for the asynchronous calibration data). However, this would cost significantly more effort and would lengthen the update and maintenance cycle. Note that for the maintenance of the processing chain it is beneficial when as much as possible data can be created by automated processes or software. This minimizes the need that human intervention has to be thoroughly logged. Additionally, to cope with the amount of data of modern satellite missions, it is required that several processor instances can run in parallel in order to meet timeliness requirements.

### **File based or database storage?**

The main difference between a file based approach and a database approach is the effort in guaranteeing traceability, reproducibility, error analyses and to ensure that different instances of the processor can read the needed data without file corruption. For file based storage the latter has to be, in addition, taken care of in the processor. In principle, two approaches are possible here to ensure that parallel access to files is safe: (1) make a copy of the data for all instances and (2) implement file locking. In the copying approach each processor instance has its own local copy of the calibration files. This implies that new calibration parameters that are generated by a given instance are copied to the file space of the other instances, because otherwise they are not available there and outdated data might be used. Using outdated calibration data would lead to varying quality of the generated level 1b product. Note that the copying of data to the file space of all instances will take some time. We will call this "dead time" here. During this dead time, level 1b data generated by the other instances possibly use outdated data. While this is also the case for the database approach (before the calibration data can be used, they have to be written to the database), the writing of the database is much quicker and the dead time in which outdated data are possibly used is much shorter. Furthermore, in the copying approach, the dead time is a function of the instance, i.e. for some processor instances the data might already have arrived and can be used while for others this is not yet the case. In the database approach,

the dead time is the same for all instances, because all instances access the same pool of data. If a given update becomes available at a certain point in time, it is immediately available for all instances. The copying of files also requires that the processor “knows” about the other processor instances and their calibration file spaces. However, the design must not make assumptions about the number of instances. Also, adding a varying number of calibration file space locations to the processor configuration is cumbersome and complicates the configuration. Therefore, the copying approach needs a “master file space”. All instances write their result to the master file space. An independent process monitors the file space and as soon as a new file appears on the master file space, it triggers another process that copies the new file to the dedicated calibration file space of a given instance. This has also to be done for each instance.

The file locking approach uses only one calibration file space that serves all processor instances. In order to prevent simultaneous access to files the files are locked during the time that one of the instances accesses the file. Note that each calibration parameter file has to have a dedicated lock. Otherwise it would be possible that the master file space is continuously locked, if always one processor instance tries to write to the file space. While this approach is technically possible, it has some disadvantages. If one processor instance locks a certain file and dies before it can unlock the file again, the file stays locked and none of the other instances can access the associated calibration parameter. To solve this situation automatically, time out mechanisms have to be implemented that free the lock and clean up data that were not fully written or are in other ways corrupt. While this is possible, the software will never be able to solve all conflicts while at the same time guarantee the best quality. Therefore, in addition, some manual activity is needed, in which the processing is stopped and locks are cleaned manually. Another problem with the file locking approach is that the slowest instance of the processor will determine the processing time. While the master file space is locked for a certain parameter, all other instances have to wait.

Using a database eliminates all problems of parallel access “out-of-the-box”, since modern databases handle parallel access automatically. The database approach has additional advantages:

- Tagging the data with time and give them a unique ID can be handled automatically by the database, while for a file base approach this has to be handled by e.g. file naming or a specific directory structure.
- Extraction of a subset of data is easier in the database approach. For example, the extraction of data for one spectral band over the whole mission is one database query. In a file based approach all files have to be looked up, read in and the region of interest has to be extracted.
- The application of multiple filters to extract data is built into standard databases.
- Some statistical operations like averaging, standard deviations, minimum and maximum etc. are built into many available databases.
- Version history is automatically available in databases which ensures traceability.

In the SCIAMACHY project we migrated from a pure file based approach to a database approach (using a postgres database). The primary reason at that time was that because of the file based approach calibration data were not properly updated during re-processing, requiring a costly repetition of the processing of the whole mission. The database is part of the operational processor since V8 and based on this experience we made the following observations:

- Anomaly investigations, which require processing a file in the reference and the operational environment with exactly the same inputs, can be done much quicker.
- The quality control and visualization of the calibration data can easily be automated. After the initial setup of the visualization and analyses tools the generation of the quality report was a matter of less than a day for the whole mission that encompasses 50000 orbits. With the file based approach this took much longer mainly because before analysis the data had to be extracted from several 10000 files.

While the first setup of the database may cost some time and also the transfer to the ground segment has to be carefully planned, our experience has shown that the database approach is superior to the file based approach. Therefore we recommended to use a database for the level 0-1 processing for other space-borne missions. In consequence, we developed the calibration data base that will be an integral

part of the Sentinel-4 UVN level 0-1b prototype processor and the database approach will also be used in the operational level 0-1b processor for the MERLIN mission to be developed by us.

## 2.5 Remote Sensing from High Altitude Platforms

*K.-P. Heue, T. Trautmann, T. Erbertseder (DFD-AT), S. Wlach (RM-MSY)*

Unmanned high altitude platforms (HAP) recently gained increasing interest by both potential industrial and scientific users. Possible applications range from Earth Observation as on traditional aircraft to telecommunications knots in remote areas similar to telecommunication satellites. The relative low costs and the high flexibility compared to satellites are a clear advantage of the HAP. Moreover, compared to aircraft, HAP's long flight duration of several days (in the current planning) certainly is a big asset. DLR develops a high altitude platform for scientific applications (Fig. 2-12). In total 18 DLR institutes contribute to the development of the platform and its instrumentation. Among other missions this platform will be used for remote sensing of the atmospheric composition.

### **High Altitude Platform**

Traditional aircraft fly at 10 to 15 km altitudes. In contrast, the unmanned HAP will reach about 20 km altitude. It is planned that the plane will be propelled by electric engines and solar panels shall provide the necessary energy during the day and charge battery for the night. This combination will allow flight durations of several days or longer and hence open unique possibilities for all kind of scientific measurements, e.g. monitoring the trace gas distribution of a certain area or city for several days. Thus observations of how a smog situation develops or the weekend effect can be accomplished in detail.

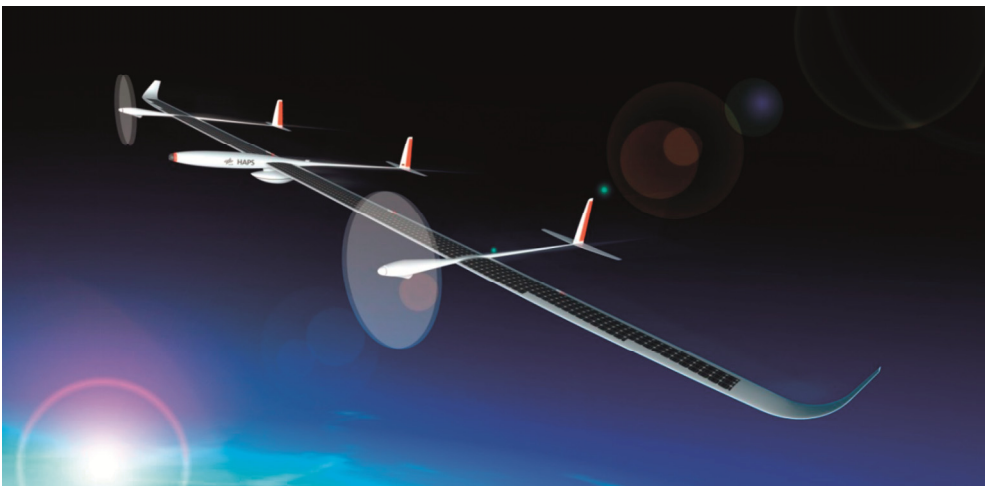


Fig. 2-12: Illustration of a possible DLR-HAP.

Continuous flying at 15-20 km altitude is on the edge of what is currently possible with existing technologies. Every aspect of the aircraft has to be optimized for mass, power and performance. This includes synergetic optimizations between payload and airframe.

### **DOAS on HAPs**

For differential optical absorption spectroscopy (DOAS) the reflected and scattered sunlight is spectrally analyzed. The spectra are measured by a detector and saved for subsequent analysis. They comprise absorption features of individual trace gases according to the Beer-Lambert law. By fitting the absorption cross sections of trace gases like SO<sub>2</sub>, O<sub>3</sub>, HCHO, NO<sub>2</sub> or water vapor to the ratio of two spectra, the trace gases can be identified and quantified.

The principle setup will be as follows: The reflected or scattered sunlight is reflected by a scanning mirror onto a lens, which focuses the light onto the entrance slit of a spectrometer or a fibre that guides the light to the spectrometer (Fig. 2-13). The data is stored on a computer and if possible directly transferred to the ground. The mirror scans a line perpendicular to the flight direction, which, in combination with the forward movement along the flight path, allows mapping the trace gas

distribution below the flight altitude. From time to time the mirror will be turned around for zenith measurements through a second window in the top of the plane. It can be assumed that these spectra contain only the absorption features of the trace gases above the flight altitude, hence they can be used as reference in the DOAS retrieval.

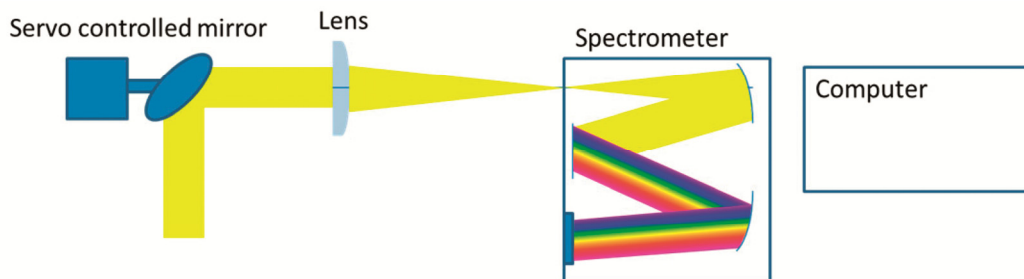


Fig. 2-13: Systematic setup of the DOAS instrument.

The instrument shall fit in a tube of 10 cm diameter and a length of less than 60 cm, which will limit the size of the spectrometer. Airborne DOAS measurements have been performed by several research groups (Heue et al. 2008, Meier et al. 2017). Merlaud et al. (2017) recently used an UAV (unmanned aerial vehicle) to perform measurements around a power station. Their DOAS instrument is of great interest as it weighs less than 1kg. Therefore it is very well suited for measurements on high altitude platforms. A similar but improved system is planned for application on the DLR-HAP.

### Aims of DOAS measurements

Currently often an observation gap between the ground based in-situ measurements and satellite observations exist. Fig. 2-14 illustrates a simulation of the NO<sub>2</sub> distribution for Brussels with different resolution sampling. The spaceborne TROPOMI sensor on Sentinel-5P has a resolution of 3.5 × 7 km<sup>2</sup>, slightly better than the right subfigure. This is insufficient for comparison with high resolution chemical transport models. A DOAS instrument on a HAP will have a much better resolution of less than 1 km or even 100 m per pixel. Observing a city with such a fine resolution over a longer period would be extremely helpful to study atmospheric chemical processes or validate chemical transport models. The data might also be used for the validation of upcoming satellite mission like Sentinel-4 or -5.

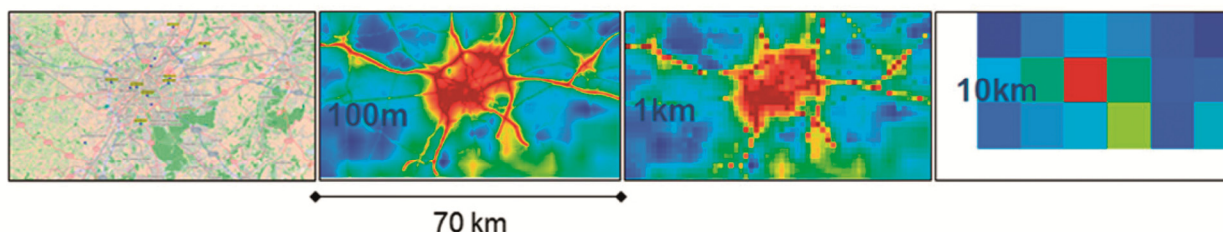


Fig. 2-14: Simulated NO<sub>2</sub> distribution over Brussels as it would be detected with different resolutions. From the left to the right with decreasing spatial resolution: point measurements, 100m, 1km and 10 km resolution.

### References

Heue, K.-P., Wagner, T., Broccardo, S.P., Walter, D., et al.: Direct observation of two dimensional trace gas distributions with an airborne imaging DOAS instrument. *Atmos. Chem. Phys.*, 8, 6707-6717, <https://doi.org/10.5194/acp-8-6707-2008>, 2008.

Meier, A. C., Schönhardt, A., Bösch, T., Richter, A., et al.: High-resolution airborne imaging DOAS measurements of NO<sub>2</sub> above Bucharest during AROMAT. *Atmos. Meas. Tech.*, 10, 1831-1857, <https://doi.org/10.5194/amt-10-1831-2017>, 2017.

Merlaud, A., Tack, F., Constantin, D., et al.: The Small Whiskbroom Imager for atmospheric composition monitoring (SWING) and its operations from an Unmanned Aerial Vehicle (UAV) during the AROMAT campaign. *Atmos. Meas. Tech. Discuss.*, <https://doi.org/10.5194/amt-2017-211>, in review, 2017.

## 2.6 Retrieval of Aerosol Profiles from the MAX-DOAS Measurement at the UFS

Z. Wang, K.-P. Heue, K.L. Chan, A. Doicu, T. Wagner (MPIC), N. Hao (EUMETSAT)

The UFS (Umweltforschungsstation Schneefernerhaus), located directly below the summit of Germany's highest mountain Zugspitze (2962 m), is a background observation site with mostly clean and unpolluted air. It is ideal for the measurement of the stratosphere and the free troposphere (see annual report 2009). The MAX-DOAS (Multi-AXis Differential Optical Absorption Spectroscopy) instrument at the UFS has been working since 2011 (see annual report 2015). MAX-DOAS is a ground-based remote sensing technique which can measure the vertical profiles of aerosol and trace gases. It measures the spectra of scattered sunlight at different elevation angles, and then the DSCDs (differential slant column densities) of trace gases are calculated from the spectra using the DOAS method.

The retrieval of aerosol profiles takes advantage of the absorption of  $O_4$  (oxygen dimer). The concentration of  $O_4$  is in direct proportion to the square of the concentration of  $O_2$ . Therefore, the concentration of  $O_4$  decreases rapidly with increasing altitude, and the vertical profile is well-known and stable. Based on the principle that aerosols in the atmosphere can change the light path of scattered sunlight and hence change the  $O_4$  absorption, the aerosol profile can be retrieved from the DSCDs of  $O_4$  measured by the MAX-DOAS instrument. Having the aerosol profiles known, the profiles of trace gases can also be retrieved.

### **Problem with the commonly used algorithms**

Most MAX-DOAS studies usually retrieve the aerosol profiles with the optimal estimation method. However, as the UFS MAX-DOAS instrument is located at a very high altitude (2650 m above sea level) where the  $O_4$  concentration is much lower than at low altitude areas, the sensitivity of the aerosol retrieval is also much lower. Moreover, as the ground surface around the UFS is very undulated and complicated, it is difficult to make an accurate radiative transfer simulation, which is required for aerosol retrieval. Therefore, retrieving aerosol profiles from the UFS MAX-DOAS data with the commonly used algorithms can often get unreasonable results.

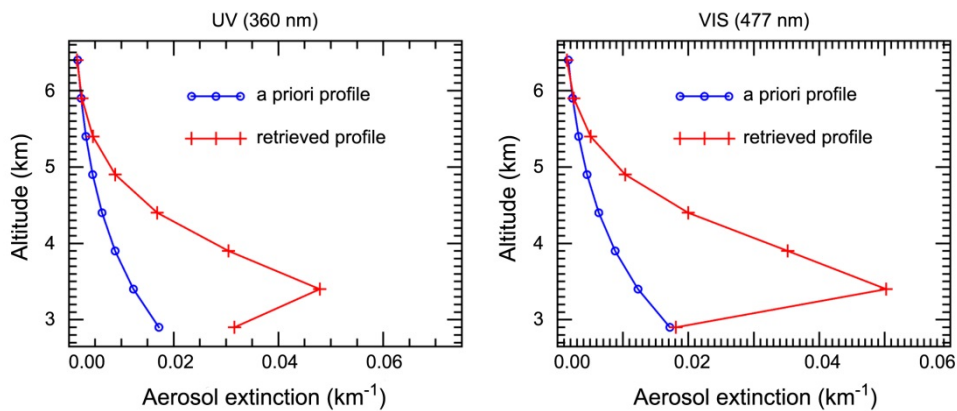


Fig. 2-15: Aerosol profile in a cloud free period (August 30, 2015 11:47 UTC) retrieved with bePRO.

Fig. 2-15 shows an example of the aerosol profile retrieved from the UFS MAX-DOAS measurement using the commonly established algorithm bePRO (Cl mer *et al.* 2010, Hendrick *et al.* 2014), which is developed by BIRA-IASB. It uses the optimal estimation method of Rodgers (2000), and includes LIDORT as the forward model. The spectra were measured at a cloud free moment, but the retrieved aerosol profiles of both UV and VIS band show a significant elevated aerosol layer between 500 and 1000 m above ground, which ought not to exist.

Fig. 2-16 displays the  $O_4$  DSCDs simulated by LIDORT with box-shaped profiles that have the same surface extinction but different scaling heights. It can be seen that  $O_4$  DSCD has hardly any sensitivity for aerosol higher than 2 km above ground. Hence the upper part of the retrieved profiles would be mostly determined by the a priori profiles if the retrieval is only based on  $O_4$  DSCDs. However, according to the ceilometer measurement at the UFS, the scaling height of aerosol at the UFS is usually larger than 2 km.

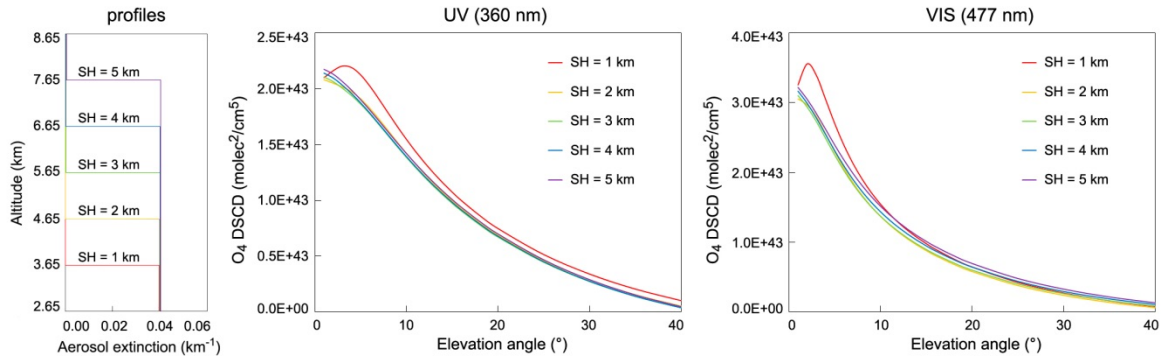


Fig. 2-16: Simulated  $O_4$  DSCDs for box-shaped profiles with the same surface aerosol extinction but different scaling heights (SZA =  $39^\circ$ , RAA =  $8^\circ$ ).

### **Aerosol retrieval using DSCD and RI look-up table**

Although insensitive to the aerosol at high altitude, simulation results show that for a fixed set of SZA (solar zenith angle) and RAA (relative solar azimuth angle), the  $O_4$  DSCDs of all elevation angles decrease monotonically with increasing surface aerosol extinction (an example is shown in Fig. 2-19). We also found that during cloud free moments, the measured  $O_4$  DSCDs of all elevation angles usually agree well with the simulated results of aerosol profiles with tangent curve shape and proper surface aerosol extinction (Fig. 2-17 illustrates an example). In order to obtain more aerosol information from the MAX-DOAS measurement, the relationship between RI (relative light intensity, i.e. the ratio between the light intensities at a certain wavelength of the non-zenith measurement and the zenith measurement of the same scanning cycle) and the aerosol profile is also studied. The simulation results show that RI is insensitive to the shape of the aerosol profile (Fig. 2-18), while RI at some elevation angles is sensitive to the total AOD (aerosol optical depth) (an example is shown in Fig. 2-19).

Therefore, it is feasible to obtain aerosol profile information from  $O_4$  DSCDs and RIs measured by MAX-DOAS by building a look-up table. We simulated the  $O_4$  DSCDs and RIs at 22 different elevation angles for 100 different aerosol profiles with surface extinction varying between 0 and  $0.3 \text{ km}^{-1}$  and a scaling height fixed to 3 km, and every profile was calculated with all the possible combinations of SZA and RAA with  $1^\circ \times 1^\circ$  resolution. From the look-up table, the surface aerosol extinctions can be obtained by using the  $O_4$  DSCDs of one or more elevation angles as the key value, and the total AODs can be obtained by using the RIs as the key value. Afterwards, the aerosol profiles can be derived. Fig. 2-19 shows an example of deriving the aerosol information from a set of MAX-DOAS results. It is the same scanning cycle as the example shown in Fig. 2-15. The curves are simulated results, and the squares refer to the look-up results corresponding to the  $O_4$  DSCDs and RIs actually measured. It can be seen that in both UV and VIS bands, the surface extinction results derived from the  $O_4$  DSCDs of three different elevation angles agree well with each other. Regarding the look-up result of total AOD, the agreement between different elevation angles is less good as the surface extinction, but still in reasonable range. Taking the average value, the surface extinctions and total AODs at 360 and 477 nm can be derived, and then the aerosol profiles can be determined accordingly (Fig. 2-20). Due to the lack of information, the exact shape of the profiles is decided somewhat arbitrarily, but they are already much more reasonable and more convincingly than the former results shown in Fig. 2-15.

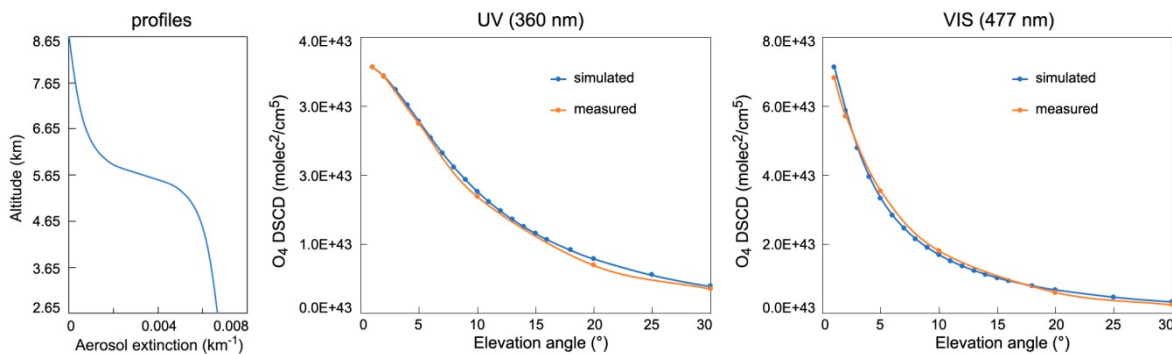


Fig. 2-17: Comparison of measured and simulated  $O_4$  DSCDs (December 7, 2015 11:42 UTC).

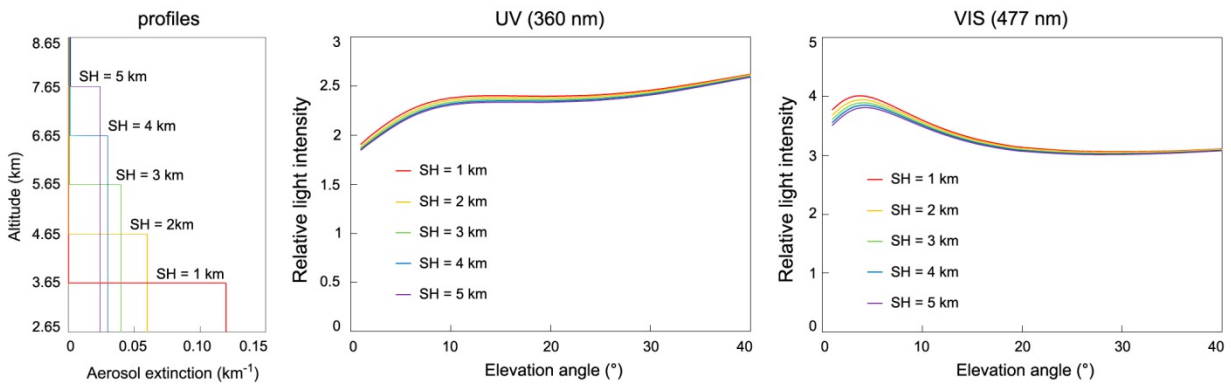


Fig. 2-18: Simulated relative light intensities for box-shaped profiles with the same total AODs but different scaling heights (SZA = 39°, RAA = 8°).

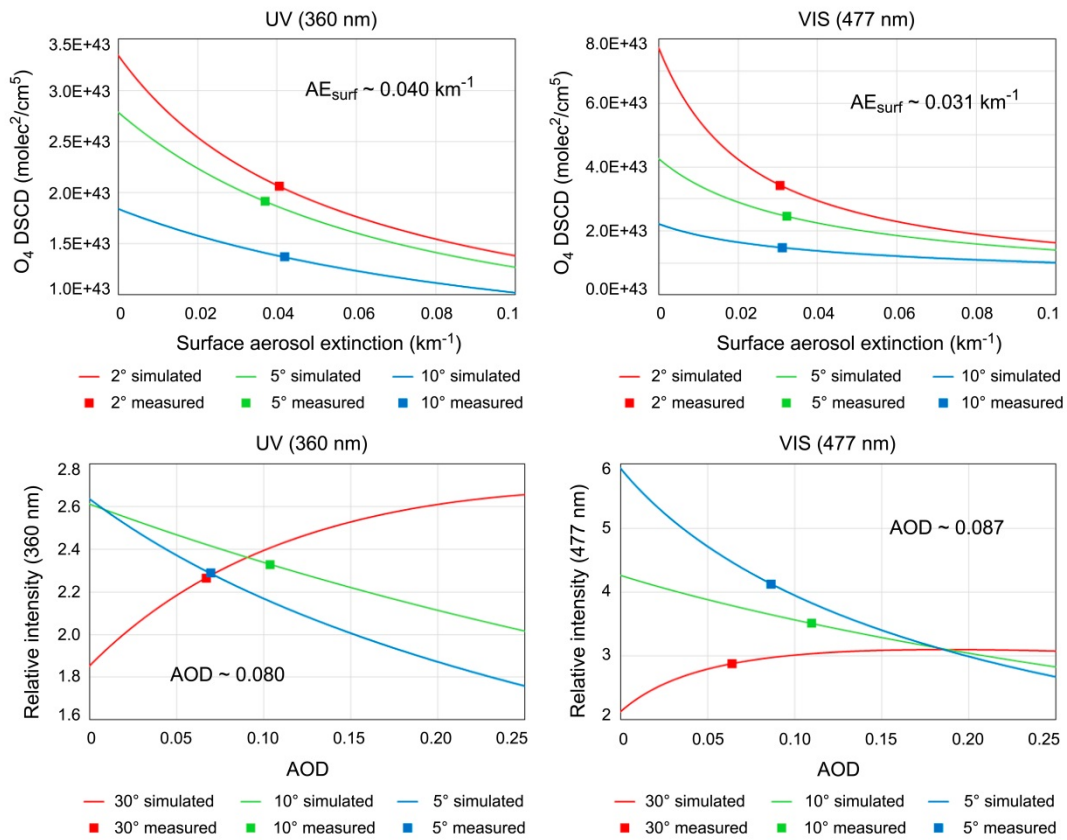


Fig. 2-19: Example of deriving surface aerosol extinction and total AOD from the look-up table (August 30, 2015 11:47 UTC).

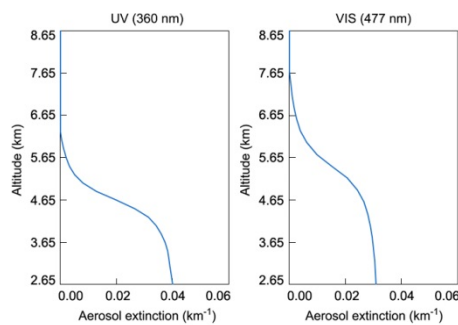


Fig. 2-20: Aerosol profiles derived from the LUT results (August 30, 2015 11:47 UTC).

## References

*Clémer, K., Van Roozendaal, M., Fayt, C., et al.*: Multiple wavelength retrieval of tropospheric aerosol optical properties from MAXDOAS measurements in Beijing. *Atmos. Meas. Tech.*, 3, 863-878, doi:10.5194/amt-3-863-2010, 2010.

*Hendrick, F., Müller, J.-F., Clémer, K., et al.*: Four years of ground-based MAX-DOAS observations of HONO and NO<sub>2</sub> in the Beijing area. *Atmos. Chem. Phys.*, 14, 765-781, doi:10.5194/acp-14-765-2014, 2014.

*Rodgers, C.D.*: Inverse methods for atmospheric sounding: theory and practice. Ser. Atmos. Oceanic Planet. Phys – Vol. 2, World Scientific Publishing, 2000.



### 3. Atmospheric Remote Sensing – Methods

#### 3.1 Operational Atmospheric Composition SAF Trace Gas Column Products from GOME-2

*P. Valks, P. Hedelt, S. Liu, K.-P. Heue, K.L. Chan, R. Lutz, D. Loyola*

The operational GOME-2 trace gas column and cloud products from MetOp-A and MetOp-B are provided by IMF-ATP in the framework of EUMETSAT's Satellite Application Facility on Atmospheric Composition Monitoring (AC SAF). The current GOME-2 trace gas products include total ozone, total and tropospheric NO<sub>2</sub>, SO<sub>2</sub>, BrO, formaldehyde (HCHO) and water vapor. The AC SAF trace gas column products are generated operationally at DLR using the GOME Data Processor (GDP) version 4.8 and are used in the near-realtime (NRT) system of the Copernicus Atmospheric Monitoring Service (CAMS). In 2017, the improved GOME-2 OCIO product has become operational, and the OCIO data set has been processed for the complete MetOp-A and -B missions (*Valks et al. 2017*)

In the first year of the third Continuous Development and Operation Phase (CDOP-3) of the AC SAF, the focus was on the development of new GOME-2 trace gas products, including glyoxal and tropospheric BrO columns, as well as NO<sub>2</sub> and water vapor climate products (*Grossi et al. 2017*). In addition, EPS-SG preparations have started for the Day-1 Sentinel-4 and Sentinel-5 trace gas column products to be provided by the AC SAF (H<sub>2</sub>O, BrO and OCIO) in the future.

##### **GOME-2 glyoxal columns**

Glyoxal (CHOCHO) is produced in the troposphere by oxidation of NMVOCs (non-methane volatile organic compounds), which are emitted naturally and by human activities. In addition, direct emissions (vegetation fires, fossil fuel and biofuel combustion) contribute also to the glyoxal abundance in the troposphere.

The retrieval of glyoxal from GOME-2 is based on the DOAS technique and optimized settings have been used to determine glyoxal slant and vertical columns (*Lerot et al. 2010, Hao et al. 2016*). To reduce the interference between glyoxal and liquid water vapor absorption features, a two-step DOAS fit retrieval has been implemented. Firstly, the liquid water columns are fitted in the large wavelength range 405-490 nm. Then glyoxal columns are retrieved in the wavelength range 435-460 nm, using the liquid water determined in the first step. In DOAS retrievals, usually daily irradiance spectra measured by GOME-2 are used as reference. However, their usage introduces yearly reproducible time-dependent offsets in the retrieved glyoxal slant columns. Therefore, daily averaged Earth shine radiances selected in the remote Pacific Ocean region (between 45° S - 45° N) are used as the reference in the DOAS retrieval. In addition, a daily normalization procedure based on measurements in the Pacific is applied, as commonly used for minor trace gas retrievals. This procedure uses the retrieved glyoxal slant columns in the Pacific reference sector (between 135° W and 180° W) to remove possible systematic biases and to ensure that the mean vertical column of the clear sky pixels in the reference sector is equal to  $1 \times 10^{14}$  molec/cm<sup>2</sup>.

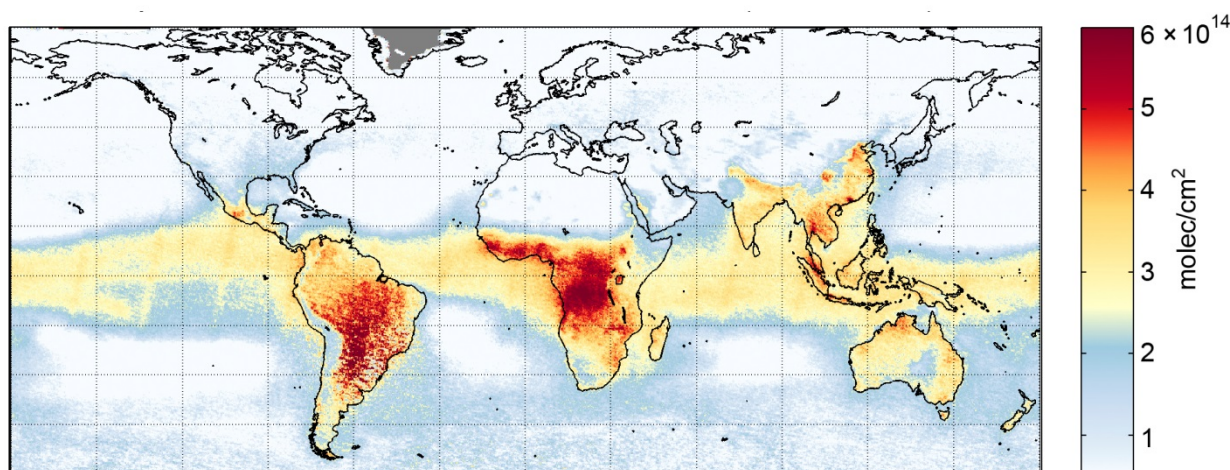


Fig. 3-1: Global tropospheric glyoxal columns for the period 2007-2015 as retrieved from GOME-2 on Metop-A (from *Lerot et al. 2017*).

For the conversion of the glyoxal slant columns to vertical columns, an accurate air mass factor is required. The air mass factor depends strongly on the vertical profile shape of glyoxal in the troposphere, the surface albedo and the presence of clouds. A look-up table of altitude dependent air mass factors has been calculated with the LIDORT radiative transfer model and combined with a priori glyoxal vertical distributions provided by the IMAGES V2 chemical transport model. For many measurements over cloudy scenes, the cloud-top is well above the glyoxal abundance in the boundary layer, and when the clouds are optical thick, the enhanced tropospheric glyoxal concentrations cannot be detected by GOME-2. Therefore, vertical columns retrieved for observations with cloud fraction > 20% are flagged in the GOME-2 Level-2 product.

Fig. 3-1 shows the average tropospheric glyoxal columns for the period 2007-2015 as retrieved from GOME-2 on Metop-A. Highest glyoxal vertical columns are mainly observed in continental tropical regions, while the mid-latitude columns strongly depend on the season with maximum values during warm months. Anthropogenic emissions are also observed in highly populated regions of Asia.

### References

Grossi, M., Valks, P., Liu, S.: Algorithm Theoretical Basis Document for GOME-2 NO<sub>2</sub> and H<sub>2</sub>O Level 3 Climate Products. SAF/O3M/DLR/ATBD/Clim, Issue 1/C, March 2017.

Hao, N., Lerot, C., Valks, P.: Algorithm Theoretical Basis Document for the GOME-2 Glyoxal Product. SAF/O3M/DLR/ATBD/03, Issue 1/A, June 2016.

Lerot, C., Stavrou, T., De Smedt, I., Müller, J.-F., and Van Roozendael, M.: Glyoxal vertical columns from GOME-2 backscattered light measurements and comparisons with a global model. *Atmos. Chem. Phys.*, 10, 12059-12072, 2010.

Valks, P., Loyola, D., Hao, N., Hedelt, P., Slijkhuis, S., Grossi, M., Begoin, M., Gimeno Garcia, S., Lutz, R.: Algorithm Theoretical Basis Document for GOME-2 Total Column Products of Ozone, Minor Trace Gases and Cloud Properties (GDP 4.8 for O3M-SAF OTO and NTO). DLR/GOME-2/ATBD/01, Issue 3/A Rev. 2, June 2017.

## **3.2 Improvement of Total and Tropospheric NO<sub>2</sub> Column Retrieval for GOME-2**

*S. Liu, P. Valks*

The retrieval algorithm of total and tropospheric NO<sub>2</sub> column for GOME-2 consists of several steps.

- 1) The differential optical absorption spectroscopy (DOAS) method is applied to determine the NO<sub>2</sub> slant columns from GOME-2 in the visible wavelength region. NO<sub>2</sub> slant columns are converted to initial total NO<sub>2</sub> vertical columns by dividing with a stratospheric air mass factor (AMF). The AMF is determined using the LIDORT radiative transfer model (RTM) based on various input parameters, including the GOME-2 viewing geometry, surface height, and surface albedo (described by surface Lambertian equivalent reflectivity (LER)).
- 2) Stratospheric NO<sub>2</sub> columns are estimated using NO<sub>2</sub> measurements over clean regions based on the assumption of longitudinally homogeneous stratospheric NO<sub>2</sub>.
- 3) Tropospheric NO<sub>2</sub> columns are derived by a tropospheric AMF based on a priori NO<sub>2</sub> profiles from chemistry transport model. The calculation of the tropospheric AMF requires the same input parameters as for the stratospheric AMF, but its dependency on these parameters is much stronger.

The operational retrieval algorithm as implemented in the GDP 4.8 was introduced by *Valks et al. (2011)*. Table 3-1 summarizes our main improvements to the operational (GDP 4.8) algorithm.

To calculate the NO<sub>2</sub> slant columns, a large 425-497 nm wavelength fitting window is used in the DOAS fit to increase the signal-to-noise ratio. Absorption cross-sections are updated and a linear intensity offset correction is applied. The long-term variations of the GOME-2 slit function, resulting from the temperature change of instrument, are treated by deriving effective slit functions with a stretched preflight line shape. Comparing to the operational algorithm, the improved NO<sub>2</sub> columns are higher by

$\sim 1\text{-}3 \times 10^{14}$  molec/cm<sup>2</sup> (up to 27%) over Pacific, as illustrated in Fig. 3-2, and the slant column errors are lower by  $\sim 24\%$ . The effect of using the new version 6.1 GOME-2 level 1b data is analyzed for our level 1-2 algorithm, which reduces largely the offset between GOME-2A and GOME-2B data by decreasing more significantly the NO<sub>2</sub> columns for GOME-2B ( $\sim 6\text{-}11\%$  for GOME-2A and  $\sim 15\text{-}23\%$  for GOME-2B).

Steps	Parameter	GDP 4.8	Improved Algorithm
DOAS	Wavelength range	420-450 nm	425-497 nm
	Cross-sections	NO <sub>2</sub> , H <sub>2</sub> O <sub>vap</sub> , O <sub>3</sub> , O <sub>4</sub> , Ring	NO <sub>2</sub> , H <sub>2</sub> O <sub>vap</sub> , O <sub>3</sub> , O <sub>4</sub> , Ring, H <sub>2</sub> O <sub>liq</sub> , Eta, Zeta
	Polynomial degree	3	5
	Intensity offset	constant	linear
	Slit function	preflight	stretched preflight (fitted)
Stratospheric NO <sub>2</sub> estimation		Spatial filtering method	STREAM
(Tropospheric) AMF calculation	RTM	LIDORT v2.2+	VLIDORT v2.7
	Surface LER	TOMS/GOME	GOME-2 ( <i>Tilstra et al. 2017</i> )
	a priori NO <sub>2</sub> profiles	monthly MOZART-2	daily TM5-MP

Table 3-1: Overview of the operational (GDP 4.8) and improved algorithm.

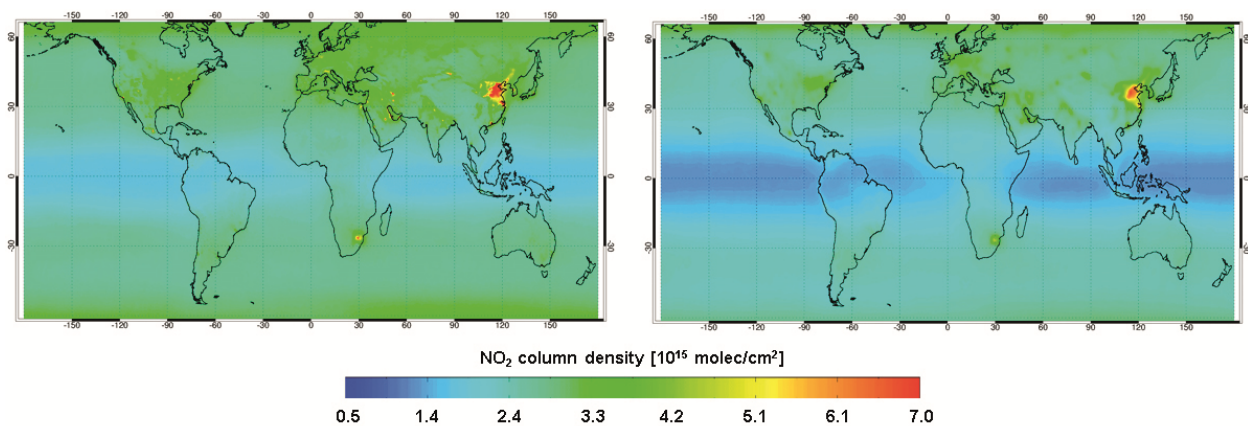


Fig. 3-2: Global total NO<sub>2</sub> column distribution in 2008 as measured by GOME-2/MetOp-A using the improved algorithm (left) and operational (GDP 4.8) algorithm (right).

To resolve the stratospheric NO<sub>2</sub>, the algorithm STRatospheric Estimation Algorithm from Mainz (STREAM, *Beirle et al. 2016*), which was originally designed for TROPOMI, is optimized for the GOME-2 instrument and tested with GOME-2 synthetic data. Comparing to the operational spatial filtering method, STREAM provides an improved treatment of cloudy and polluted pixels by defining weighting factors for each clean measurement based on polluted situation and cloudy information. The GOME-2 synthetic data is calculated from a chemistry model, which extends the tropospheric chemistry module in a CAMS model with the stratospheric chemistry from the BASCOE system (C-IFS-CB05-BASCOE experiment). Based on the GOME-2 synthetic data, the use of STREAM overestimates the stratospheric NO<sub>2</sub> by  $\sim 2 \times 10^{14}$  molec/cm<sup>2</sup> over tropical ocean and  $\sim 5 \times 10^{14}$  molec/cm<sup>2</sup> at high latitudes with stronger natural variations on a daily basis. The differences are reduced to  $\sim 1\text{-}2 \times 10^{14}$  molec/cm<sup>2</sup> in monthly averages. The stripes of larger overestimation at low latitudes in winter are largely removed by an improved latitudinal correction. Based on the GOME-2 measurements, the application of STREAM

slightly reduces the stratospheric NO<sub>2</sub> columns by  $\sim 1 \times 10^{14}$  molec/cm<sup>2</sup> and largely removes the artefacts in the operational algorithm.

To improve the calculation of NO<sub>2</sub> AMFs, a new box-AMF LUT is generated with the latest version of VLIDORT RTM with an increased number of forward model parameters and vertical layers to reduce profile interpolation errors. The new GOME-2 surface LER climatology (Tilstra et al. 2017) is derived with a high resolution longitude  $\times$  latitude grid of  $1^\circ \times 1^\circ$  ( $0.25^\circ \times 0.25^\circ$  at coastlines) and an improved LER algorithm based on observations for 2007-2013. The TM5-MP daily a priori NO<sub>2</sub> profiles capture the short-term variability in the NO<sub>2</sub> fields with a resolution of  $1^\circ \times 1^\circ$  and updated emissions. The effect of the updated surface LER and a priori NO<sub>2</sub> profiles on the retrieved tropospheric NO<sub>2</sub> is significant (more than 10%) especially over polluted area, as shown in Fig. 3-3.

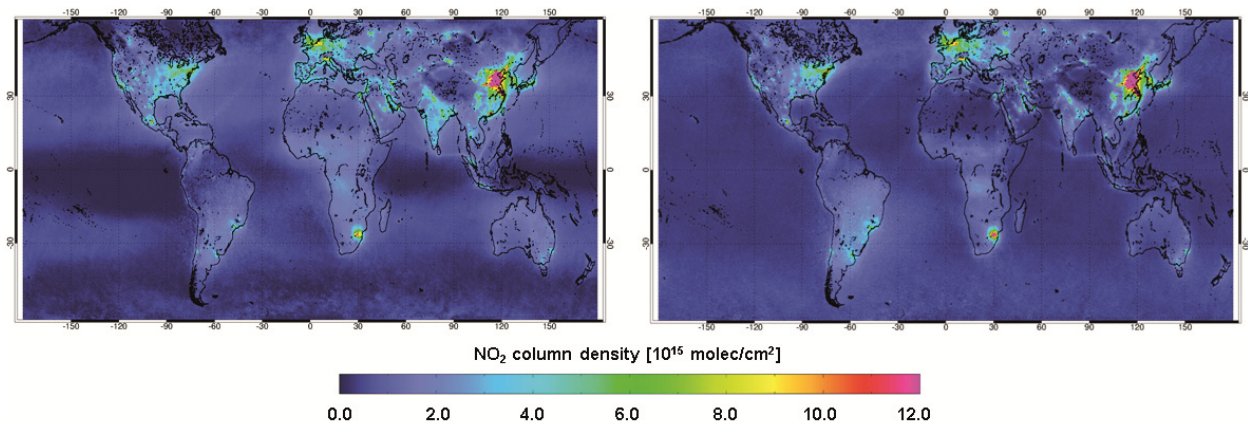


Fig. 3-3: Global tropospheric NO<sub>2</sub> column distribution in 2008 as measured by GOME-2/MetOp-A using the improved algorithm (left) and operational (GDP 4.8) algorithm (right).

### References

Beirle, S., Hörmann, C., Jöckel, P., Liu, S., Penning de Vries, M., Pozzer, A., Sihler, H., Valks, P., and Wagner, T.: The STRatospheric Estimation Algorithm from Mainz (STREAM): estimating stratospheric NO<sub>2</sub> from nadir-viewing satellites by weighted convolution. *Atmos. Meas. Tech.*, 9, 2753-2779, 2016.

Tilstra, L., Tuinder, O.N.E., Wang, P., and Stammes, P.: Surface reflectivity climatologies from UV to NIR determined from Earth observations by GOME-2 and SCIAMACHY. *Journal of Geophysical Research: Atmospheres*, 122, 4084-4111, 2017.

Valks, P., Pinardi, G., Richter, A., Lambert, J.-C., Hao, N., Loyola, D., Van Roozendael, M., Emmadi, S.: Operational total and tropospheric NO<sub>2</sub> column retrieval for GOME-2. *Atmos. Meas. Tech.*, 4, 1491-1514, 2011.

### 3.3 OCRA Cloud Fractions for GOME-2 and TROPOMI – Imager Resolution Capabilities

R. Lutz, D. Loyola, F. Romahn

Accurate trace gas retrievals from spectrometers dedicated to measure the atmospheric composition require a precise knowledge of cloud properties in the UV/VIS spectral region, i.e. where most of the trace gases like ozone, nitrogen dioxide, sulphur dioxide, formaldehyde etc. are retrieved. Furthermore, cloud information from the UV/VIS spectral range is complementary to the information retrieved using imagers operating in the VIS, NIR, SWIR and thermal IR (like e.g. MODIS on Aqua/Terra or VIIRS on Suomi-NPP).

The cloud fraction is generated using the Optical Cloud Recognition Algorithm (OCRA), which has already been successfully applied to the operational processing of GOME/ERS-2 and GOME-2/MetOp-A/B data, and also to the TROPOMI/S5P mission, launched recently on October 13, 2017. A detailed description of the color space approach used by OCRA to retrieve the cloud fraction can be found in Lutz et al. (2016) and its adaptation to the TROPOMI instrument is outlined in Loyola et al. (2017). In a

nutshell, the measured reflectances in three broad wavelength bands within the UV/VIS spectral region are transformed to a 3-color RGB space where clouds appear white assuming that the spectral signature of a cloud does not show a significant wavelength dependency across these three channels. Given a cloud-free reflectance composite map, the cloud fraction can be obtained by scaling the measured reflectances between the extreme cases of cloud-free and fully cloudy scenarios.

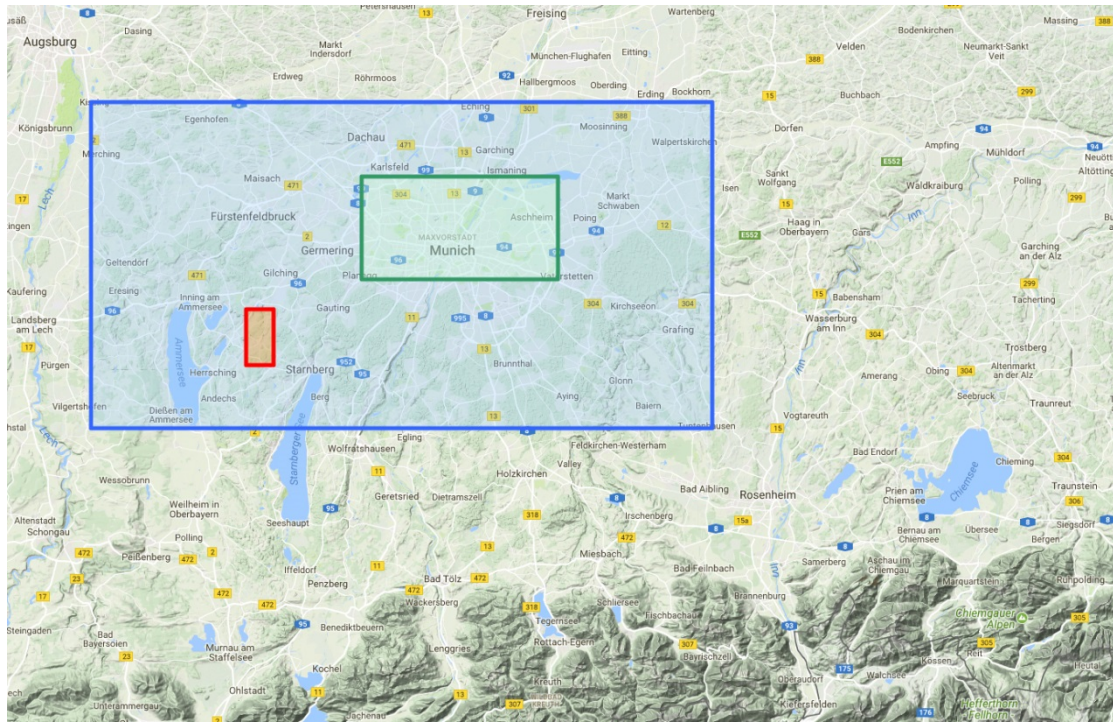


Fig. 3-4: Comparison of the footprint sizes for GOME-2 (80 × 40 km<sup>2</sup>, blue box), OMI (24 × 13 km<sup>2</sup>, green box) and TROPOMI (3.5 × 7 km<sup>2</sup>, red box).

The most evident improvement from GOME-2 to TROPOMI is the increase in spatial resolution, as it can clearly be seen in Fig. 3-4, which shows the area north of the Alps and around Munich along with the footprint sizes of a single ground pixel as measured with the GOME-2 (blue), OMI (green) and TROPOMI (red) instruments. Roughly 130 TROPOMI pixels fit into one GOME-2 pixel. Apart from providing information also on small scale cloud structures, this unprecedented spatial resolution of TROPOMI ensures a much larger number of completely cloud-free pixels, which represents the optimal scenario for a trace gas retrieval being least error prone to enhanced uncertainties due to the presence of clouds.

Fig. 3-5 demonstrates the quantum leap in terms of spatial resolution by showing the cloud fraction for a scene along the west coast of Africa for GOME-2 and TROPOMI data, both retrieved with the OCRA algorithm (panels a and b). The same scene was captured with an imager instrument (panel c). In this case the VIIRS instrument aboard the Suomi-NPP satellite which is flying in close formation with Sentinel-5P. While the coarse resolution of GOME-2 only allows to identify large and medium scale cloud structures, it is evident that TROPOMI comes close to revealing also very small scale cloud structures that so far could only be seen with imagers. Up to now such structures were hidden for spectrometers primarily dedicated to the detection and retrieval of trace gases.

It is worthwhile to emphasize that an accurate cloud parameter determination marks the first step in most trace gas retrievals. OCRA along with the ROCINN (Retrieval Of Cloud Information using Neural Networks) algorithm not only provides cloud fraction but also cloud height, cloud albedo and cloud optical thickness. Embedded in an operational chain, the OCRA/ROCINN combination is ideal for near-realtime applications, as it has already been shown for several missions (GOME, SCIAMACHY, GOME-2, TROPOMI).

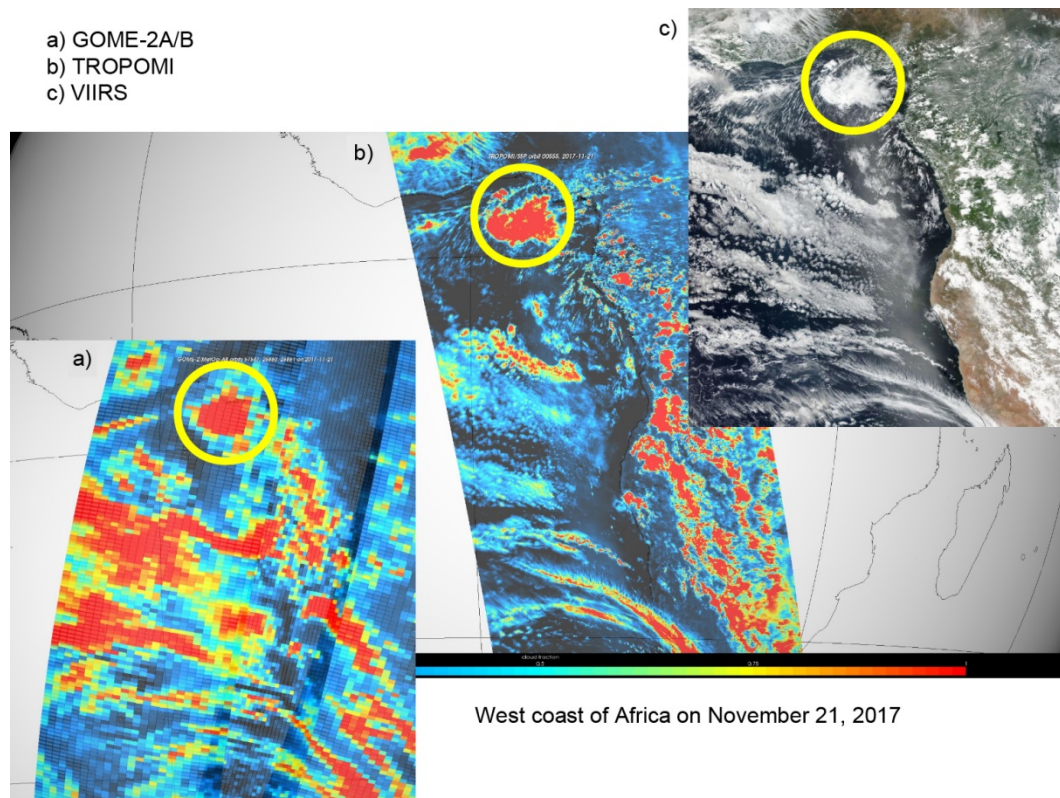


Fig. 3-5: The cloud fraction for the same region around the west coast of Africa seen with a) GOME-2A/B, b) TROPOMI (both based on the OCRA algorithm) and c) VIIRS (corrected reflectance true color RGB image) on November 21, 2017. The yellow circle highlights a common cloud structure and is intended to guide the reader's eye for comparison of the pictures. Also note that there is a time difference of about four hours between GOME-2 and TROPOMI, hence structures might have shifted a bit between a) and b). TROPOMI and VIIRS fly in close formation and therefore panels b) and c) can be regarded as simultaneous.

### References

- Lutz, R., Loyola, D., Gimeno García, S., Romahn, F.: OCRA radiometric cloud fractions for GOME-2 on MetOp-A/B. *Atmos. Meas. Tech.*, 9, 2357-2379, 2016.
- Loyola, D. G., Gimeno García, S., Lutz, R., Romahn, F., Spurr, R. J. D., Pedergnana, M., Doicu, A., and Schüssler, O.: The operational cloud retrieval algorithms from TROPOMI on board Sentinel-5 Precursor. *Atmos. Meas. Tech. Discuss.*, in press, 2017.

## 3.4 Double-cloud Layer Presence in the Cloud Parameters Retrieved from ROCINN

*A. Argyrouli, D. Loyola, R. Spurr (RT Solutions)*

Clouds are important regulators of solar fluxes in Earth's atmosphere. The accurate information of their physical and optical properties allows for the determination of trace gases and aerosol concentrations from space-borne sensors. ROCINN (Retrieval of Cloud Information using Neural Networks) is an algorithm developed for the retrieval of cloud properties such as cloud height ( $h$ ) and cloud optical thickness ( $\tau$ ) or cloud albedo ( $\omega$ ) from NIR spectrometers. The algorithm consists of two different cloud model representations: (a) CAL (Clouds As Layers) which assumes that the cloud is a cluster of spherical scatterers, and (b) CRB (Clouds as Reflecting Boundaries) which assumes that the cloud is a Lambertian reflector.

Simulated Sun-normalized radiances in and around the O<sub>2</sub> A-band (758-771 nm) are produced by the forward radiative transfer model (RTM) VLIDORT (Spurr 2006). The atmosphere in RTM consists of only air molecules (clear-sky radiance) or air molecules and a cloud layer (cloudy-sky radiance). The outgoing radiances are then normalized to the solar irradiance reference spectra from Chance and Kurucz (2010).

The assumption of a single cloud layer is not always true for real atmospheres. Frequently, multi-cloud layers appear with the most common situation being a low-level cloud and a second mid-level cloud (Wang *et al.* 1999). As an attempt to evaluate the impact of a double-cloud layer on ROCINN retrieved cloud parameters, VLIDORT simulations have been performed in order to produce the Sun-normalized radiances resulting by the presence of two clouds in the atmosphere. In Fig. 3-6 the Sun-normalized radiances in the spectral window of the ROCINN algorithm are shown for the case of a single-cloud layer and a double-cloud layer. The geometrical thickness of the low and the mid-level cloud has been assumed equal to 1 and 2 km, respectively.

The first group of simulations corresponds to a double-cloud layer model with an optically thick low cloud layer ( $\tau = 25$ ,  $h$  ranging between 2-4 km) and a second optically thinner cloud layer at mid-altitude ( $\tau = 10$ ,  $h = 6$  km). The sensitivity study, depicted in Fig. 3-7, showed that the retrieved optical thickness is not affected by the altitude of the low cloud. On the contrary, the retrieved cloud top height is quite sensitive to the separation distance between the two clouds. The comparison between the retrieved cloud heights from both the CAL and CRB model provides evidence that the CAL model is more realistic than CRB since the latter is not so sensitive to the presence of the second cloud.

The second group of simulations represents the following double-cloud layer: (1) low cloud at an altitude of 2 km and a thickness between 2 and 30, and (2) mid-level cloud with  $h = 6$  km and  $\tau = 10$ . This sensitivity study demonstrated the linear dependency between the optical thickness of the low cloud and the retrieved optical thickness from the ROCINN-CAL algorithm (left panel of Fig. 3-8). Another important conclusion which can be drawn from the simulations is that the difference between the retrieved cloud heights from ROCINN-CAL and ROCINN-CRB decreases exponentially as the optical thickness of the underlying cloud layer gets enhanced (right panel of Fig. 3-8). Provided that in real atmospheres the underlying cloud is usually optically thicker, the retrieved properties correspond mostly to those of the low cloud.

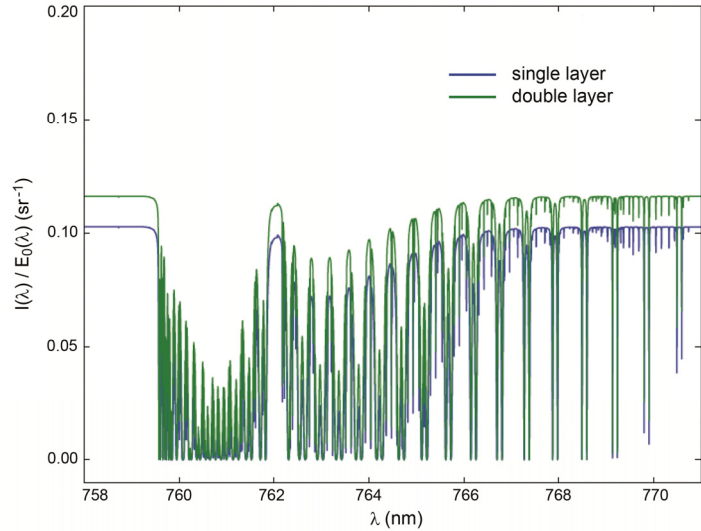


Fig. 3-6: Sun-normalized radiances over the complete ROCINN spectral window (758-771 nm) produced by the radiative transfer model VLIDORT for a single-cloud layer and a double-cloud layer model.

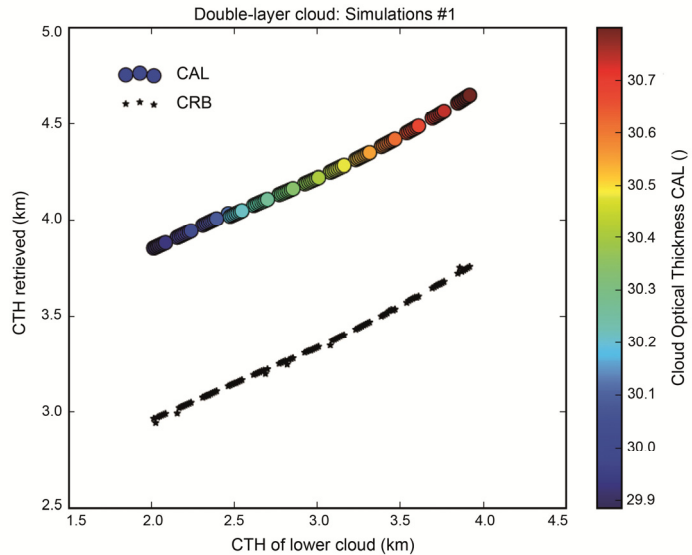


Fig. 3-7: ROCINN retrieved cloud properties for the first group of simulations. The low cloud has an optical thickness of 25, a geometrical thickness of 1 km and a cloud top height in the range 2-4 km. The second cloud is a mid-level cloud with an optical thickness of 10, a cloud top height of 6 km and a geometrical thickness of 2 km.

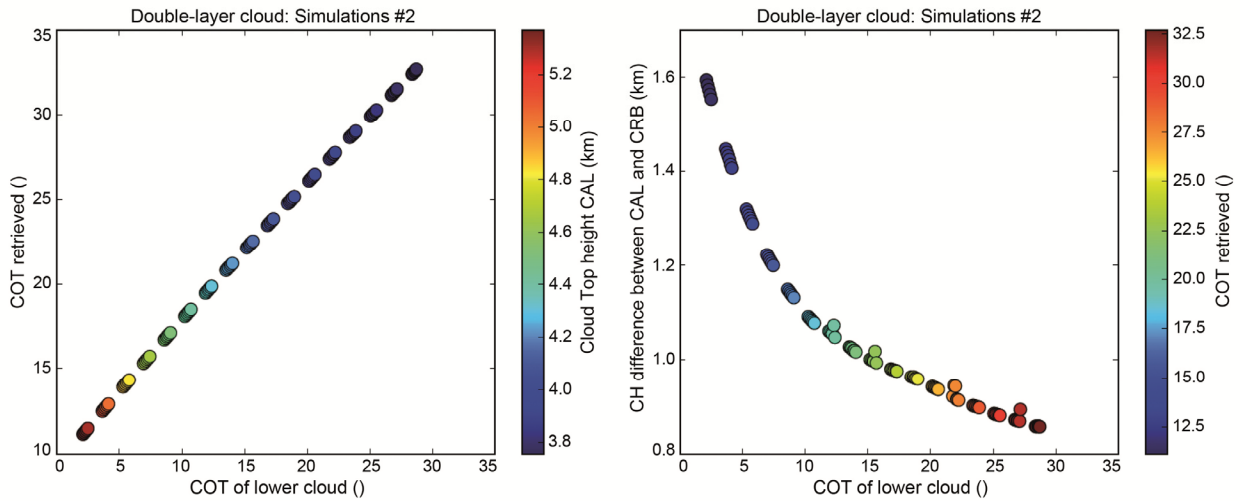


Fig. 3-8: ROCINN retrieved cloud properties for the second group of simulations. The low cloud has a cloud top height of 2 km, a cloud geometrical thickness of 1 km and a cloud optical thickness in the range 2-30. The second cloud is a mid-level cloud with an optical thickness of 10, a cloud top height of 6 km and a cloud geometrical thickness of 2 km. Left panel: Retrieved cloud top height and cloud optical thickness from ROCINN-CAL. Right panel: Differences in cloud top height retrieval between CAL and CRB as a function of the optical thickness of the low cloud.

### References

Chance, K. and Kurucz, R. L.: An improved high-resolutions solar reference spectrum for earth's atmosphere measurements in the ultraviolet, visible, and near infrared. *J. Quant. Spectros. & Radiat. Transfer*, 111, 1289-1295, 2010.

Spurr, R. J. D.: VLIDORT: A linearized pseudo-spherical vector discrete ordinate radiative transfer code for forward model and retrieval studies in multilayer multiple scattering media. *J. Quant. Spectros. & Radiat. Transfer*, 102, 316-342, <https://doi.org/10.1016/j.jqsrt.2006.05.005>, 2006.

Wang, J., Rossow, W. B., Uttal, T., and Rozendaal, M.: Variability of cloud vertical structure during ASTEX observed from a combination of rawinsonde, radar, ceilometer and satellite. *Mon. Weather Rev.*, 127, 2484-2502, 1999.

## 3.5 CO Total Column Retrievals from SCIAMACHY

P. Hochstaffl, F. Schreier

### **Full-mission validation with NDACC and TCCON**

The objective of this study was to validate the CO total column product inferred from SCIAMACHY full-mission from 2003-2011 short-wave infrared nadir observations using the Beer InfraRed Retrieval Algorithm (BIRRA, Hochstaffl et al. 2018, Gimeno García et al. 2011). Globally distributed NDACC and TCCON ground-based measurements were used as a true reference.

The bias of SCIAMACHY observations to the ground-based reference was analyzed using two different approaches, namely the classical (unweighted) and distance weighted averages. Fig. 3-9 shows that the bias of CO mixing ratios for the quadratic distance weighted averages are ranging from almost 0 ppbv to -30 ppbv. In over 70% the biases are ranging from around -5 to -15%. The global bias  $b = -11.9$  ppbv represents the mean bias of all stations weighted by the respective standard deviation. The global standard deviation of  $\sigma = 20.8$  ppbv is the average with respect to all stations.

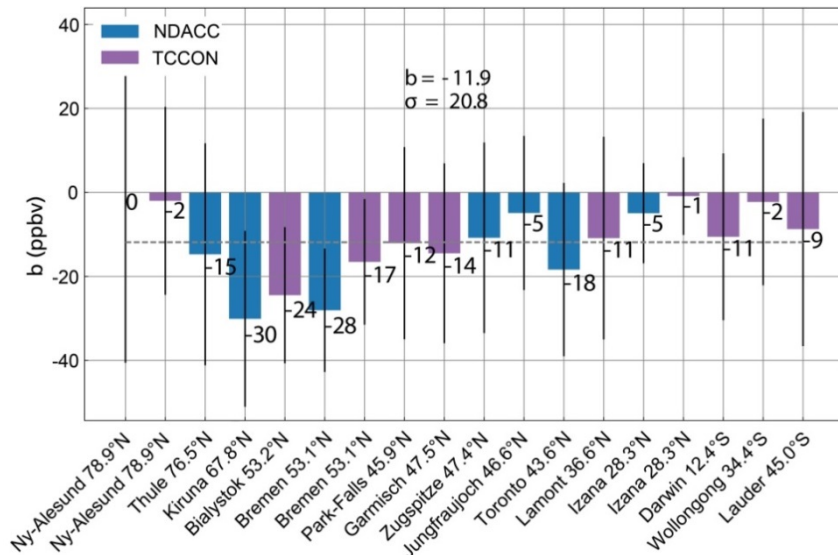


Fig. 3-9: Mean bias of NDACC (blue) and TCCON (purple) stations with co-located SCIAMACHY CO retrievals from 2003-2011. The SCIAMACHY observations were weighted inversely to the distance squared ( $r^{-2}$ ) from the reference site. The total (2003-2011) bias per site was subsequently calculated using the annual weighted biases. The dashed gray line indicates the global bias  $b$  and  $\sigma$  represents the global standard error. The dashed gray line indicates  $b$ .

The results suggest that the linear and quadratic weighted comparisons are better suited to estimate the instrument and retrieval deficiencies compared to the unweighted results (not depicted here) which might include larger fractions of representation errors. In other words, it is likely that for unweighted averages a fraction of the revealed offsets are attributed to mismatch artifacts and not only incorporate instrument or retrieval issues.

The 2003-2011 averaged CO product is shown in Fig. 3-10 with the corresponding errors in Fig. 3-11. In order to acquire representative CO mixing ratios on a regular grid globally, averaging over the complete validation period was required. Beside increased CO concentrations over China, parts of India and Indonesia due to pollution and wildfires, Fig. 3-10 also reveals valuable information of the global transport of pollution in the Earth's atmosphere. For example, the outflow of CO over the Atlantic Ocean due to biomass burning in central Africa becomes clearly visible.

In an upcoming study we aim to use model data as a reference in addition to ground-based data and examine the approach of weighted averages for other space-borne platforms such as GOSAT-2 and Sentinel-5 Precursor (S5P).

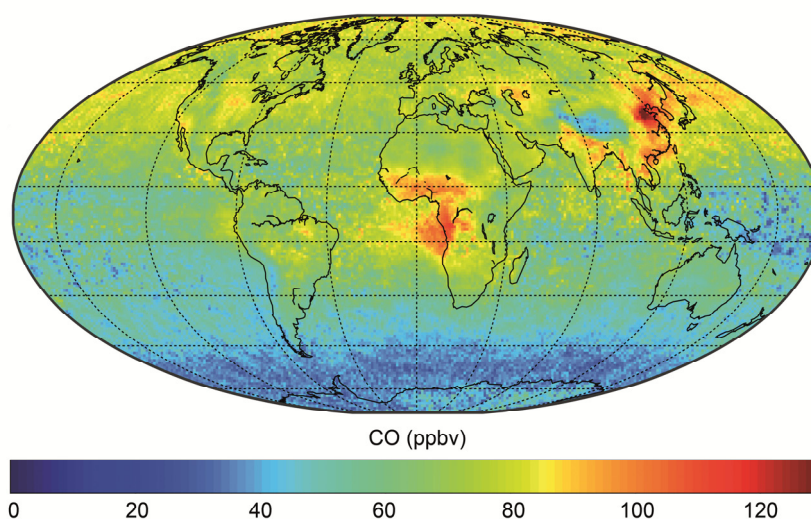


Fig. 3-10: Dry air CO column averaged mixing ratios in ppbv over land and the oceans. The values are averaged from January 2003 to December 2011 on a  $1^\circ \times 1^\circ$  latitude/longitude grid. Measurements of clear-sky scenes and optically thick cloud conditions are included.

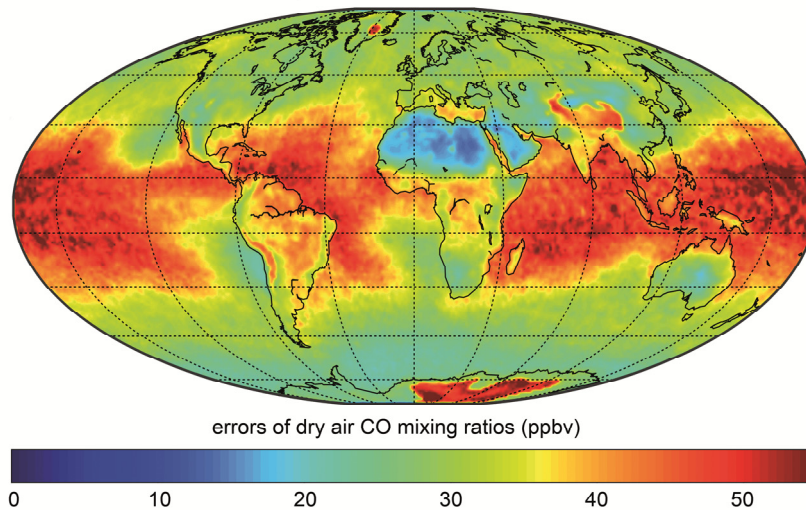


Fig. 3-11: Errors appear to be smallest in dry regions with low cloud coverage and high surface reflectivity, e.g. the Sahara Desert or the Arabian Peninsula.

**Impact of molecular absorption spectroscopy data on infrared carbon gas concentration retrievals**

The objective was to study the impact of various spectroscopic databases and their updates on BIRRA retrievals for CH<sub>4</sub> (Xu 2017) and CO (Schmidt 2014) concentrations from the short-wave infrared (SWIR) spectral range. The forward model in BIRRA is the Generic Atmospheric Radiation Line by Line Infrared Code (GARLIC) which uses molecular spectroscopic information to model the radiative transfer through the atmosphere. Parameters such as line position  $\nu$ , line strength  $S$ , and line width  $\gamma$  (air- and self-broadening) were utilized from the HITRAN (High-resolution TRANsmission molecular absorption) and GEISA (Gestion et Etude des Informations Spectroscopiques Atmospheriques) spectroscopic databases.

In a first step, SCIAMACHY observations within one orbit were used to examine the quality of the retrieval products (Fig. 3-12 and Fig. 3-13). In a second step simulated S5P observations were modeled for an ensemble of 42 different atmospheres (Fig. 3-14). The relative difference of the CH<sub>4</sub> total column between GEISA15 and GEISA11 in Fig. 3-12 shows a bimodal distribution with a median around 0.5%. The CO total columns depicted in Fig. 3-13 reveal a relative difference of about 3% between HITRAN16 and GEISA15.

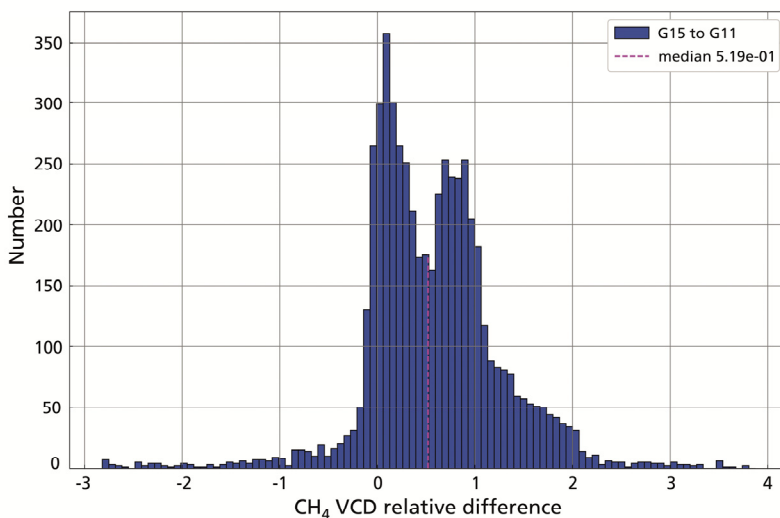


Fig. 3-12: Histogram of the CH<sub>4</sub> relative differences between GEISA15 and GEISA11. The median reveals to be around 0.5% for orbit 8663.

S5P SWIR observations were simulated using the HITRAN16 and HITRAN12 spectroscopic database. CO total columns were then retrieved from the synthetic observations using BIRRA with various spectroscopic input. No error is expected for CO columns that are retrieved with the same spectroscopic

input as the simulated observations, i.e. HITRAN16 and HITRAN12. The results indeed show that simulated SWIR observations using HITRAN16 input are retrieved successfully without introducing a bias in the CO column product. The same is true for HITRAN12. However, columns retrieved with HITRAN12 input change by about 4% with respect to the other databases. This indicates that HITRAN12 includes lines for CO in the SWIR which are not present in the other databases or vice versa and therefore impact the retrieved product.

It is planned to extend our work to other databases such as the SEOM – Improved Atmospheric Spectroscopy (SEOM-IAS) and examine its characteristics and its impact on retrievals in more detail.

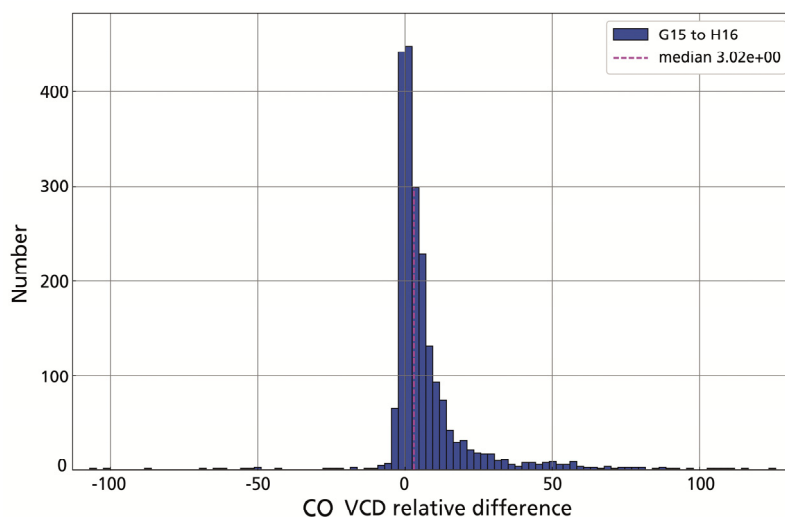


Fig. 3-13: Histogram of the CO relative differences between HITRAN16 and GEISA15. The median reveals to be around 3% for orbit 8663.

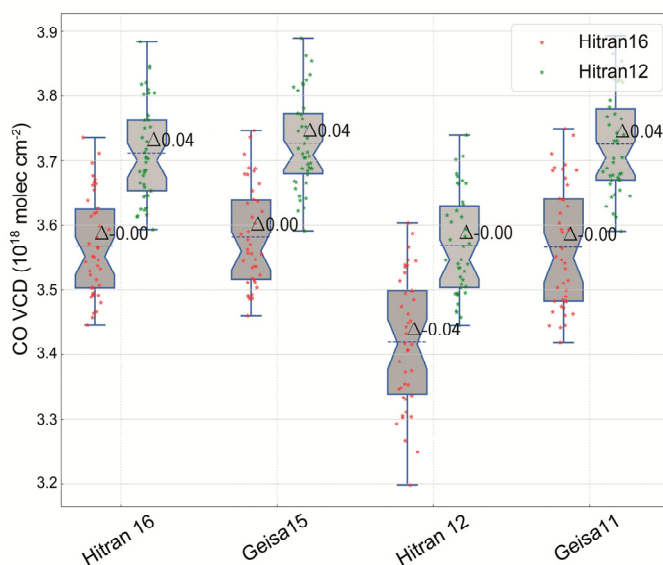


Fig. 3-14: Retrieval of CO total columns from simulated (HITRAN16 and HITRAN12) observations for an ensemble of 42 different atmospheres using various spectroscopic inputs (depicted on the x-axis). The numbers at each bar indicate the relative deviation of the retrievals from the truth, i.e. the simulated observations.

### References

- Gimeno García, S., Schreier, F., Lichtenberg, G., Slijkhuis, S.*: Near infrared nadir retrieval of vertical column densities: methodology and application to SCIAMACHY. *Atmospheric Measurement Techniques*, 4, 2633-2657, Copernicus Publications. DOI: 10.5194/amt-4-2633-2011, 2011.
- Hochstaffl, P., Schreier, F., Lichtenberg, G., Gimeno García, S.*: Validation of Carbon Monoxide Total Column Retrievals from SCIAMACHY Observations with NDACC/TCCON Ground-Based Measurements. *Remote Sens.*, 10(2), 223, 2018.
- Schmidt, D.*: Carbon Monoxide from SCIAMACHY Near Infrared Nadir Spectra: Impact of Retrieval Settings. Technical University Munich (TUM), 2014.

### 3.6 Estimating Ground Level NO<sub>2</sub> Concentrations from Satellite Observations

L. Rao, J. Xu, K. Qin (CUMT)

We performed a study for introducing a geographical and temporal weighted regression model (GTWR, Huang et al. 2010) which used OMI tropospheric NO<sub>2</sub> columns to estimate ground level NO<sub>2</sub> concentrations over central-eastern China.

#### Data

Hourly mean ground-based NO<sub>2</sub> concentrations from 715 ambient monitoring stations in central-eastern China from May 1, 2013 to April 30, 2014 (13:00-15:00 local time) were included. The NO<sub>2</sub> tropospheric column densities from the V3 Aura OMI NO<sub>2</sub> standard product (OMNO2) were filtered using a number of criteria, including

- cloud radiance fraction < 0.3
- surface albedo < 0.3
- solar zenith angles < 85°
- 10 < cross-track positions < 50, and
- root mean squared error of fit < 0.0003

Such data had been binned on to a 0.1° × 0.1° grid by calculating the area-weighted averages at each grid cell. The meteorological parameters, including relative humidity, air temperature, planetary boundary layer height, wind speed, and air pressure, were also included in the model to improve accuracy. These parameters stem from the Weather Research & Forecasting model (WRF, version 3.4.1) with the hourly mean values from 13:00 to 15:00 local time having been interpolated to a 0.1° × 0.1° grid, the same as the NO<sub>2</sub> tropospheric column products.

#### Method

The GTWR model can be expressed as

$$NO_{2\text{ ground}(i)} = \beta_0(u_i, v_i, t_i) + \beta_1(u_i, v_i, t_i) \times NO_{2\text{ Trop}(i)} + \beta_2(u_i, v_i, t_i) \times RH_{(i)} + \beta_3(u_i, v_i, t_i) \times T_{(i)} + \beta_4(u_i, v_i, t_i) \times PBLH_{(i)} + \beta_5(u_i, v_i, t_i) \times WS_{(i)} + \beta_6(u_i, v_i, t_i) \times P_{(i)} + \varepsilon_i, (i = 1, 2, 3, \dots, n) \quad (1)$$

where

$(u_i, v_i, t_i)$  = given coordinates of the training sample  $i$  in location  $(u_i, v_i)$  at time  $t_i$

$NO_{2\text{ ground}(i)}$  = ground level NO<sub>2</sub> concentration observed by the ambient monitoring station at  $(u_i, v_i, t_i)$

$\beta_0(u_i, v_i, t_i)$  = intercept of the GTWR model at  $(u_i, v_i, t_i)$ , while

$\beta_j(u_i, v_i, t_i), j = 1, 2, \dots, 6$  = slope of OMI NO<sub>2</sub> column density  $NO_{2\text{ Trop}(i)}$ ,  $RH_{(i)}$  = relative humidity,  $T_{(i)}$  = air temperature,  $PBLH_{(i)}$  = planetary boundary layer height,  $WS_{(i)}$  = wind speed and  $P_{(i)}$  = air pressure, respectively. The parameters of  $\beta(u_i, v_i, t_i)$  are determined using a local weighted least squares algorithm.  $\varepsilon_i$  is the random error.

#### Comparison between observed and estimated ground level NO<sub>2</sub> concentrations

A comparison between GTWR and three fitting models, including Ordinary Least Square (OLS), Geographical Weighted Regression (GWR), and Temporal Weighted Regression (TWR) was conducted. The Cross Validation (CV) method was used in the validation. The scattering plots between the estimated and the observed ground-level NO<sub>2</sub> concentrations are shown in Fig. 3-15. The quantitative assessment of cross-validation through the four models is shown in Table 3-2, where  $R^2$  is the coefficient of determination, RMSE is the root mean square error, MAD is the mean absolute difference and MAPE is the mean absolute percentage error.

As shown in Table 3-2, the OLS has a good performance with  $R^2$  of 0.44 for validation, which reveals that the tropospheric  $\text{NO}_2$  columns are potentially useful for estimating the ground level  $\text{NO}_2$ . The TWR outperforms the GWR with significant increases of  $R^2$  values from 0.49 to 0.55, suggesting that the temporal non-stationarity is more dominant than the spatial non-stationarity between the tropospheric  $\text{NO}_2$  columns and ground level  $\text{NO}_2$ . Among the four models, the GTWR has the best performance with the highest  $R^2$  and lowest errors (RMSE, MAD, and MAPE). In addition, the scatter plots in Fig. 3-15 illustrate the largest correlation slope and the smallest intercept for the GTWR model. It is worth noting that all of the regression line slopes for the four models are  $< 1$ .

Model	$R^2$	RMSE ( $\mu\text{g}/\text{m}^3$ )	MAD ( $\mu\text{g}/\text{m}^3$ )	MAPE (%)
OLS	0.44	0.33	12.57	73.45
GWR	0.49	0.31	12.09	68.83
TWR	0.55	0.29	11.27	64.63
GTWR	0.60	0.28	10.68	60.19

Table 3-2: Quantitative assessment of cross-validation through OLS, GWR, TWR, and GTWR.

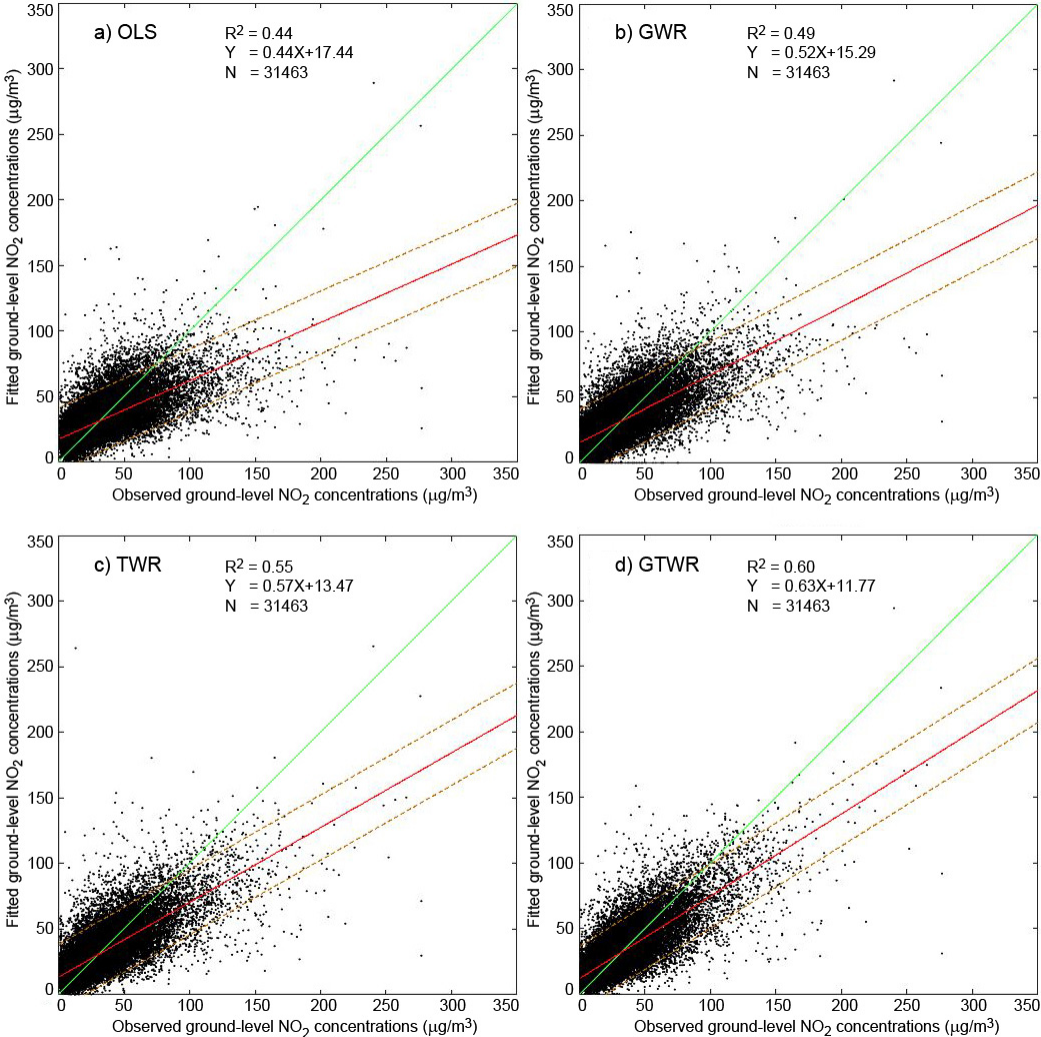


Fig. 3-15: Scatter plots between the observed  $\text{NO}_2$  and the estimated  $\text{NO}_2$  concentrations.

Fig. 3-16 displays the spatial distributions of annually mean  $\text{NO}_2$  values. The ground-observed  $\text{NO}_2$  concentrations fitted by GTWR have similar spatial patterns to the satellite tropospheric  $\text{NO}_2$  columns.

The concentrations are comparable to the interpolated in situ observations using the Kriging method over the region with high values. For the areas without monitoring stations, e.g., southern Jiangxi and northern Fujian, the GTWR method provides more reasonable estimations that are overestimated by the Kriging method. In these figures, we can see that high NO<sub>2</sub> concentrations are clustered in the regions of the North China Plain, the Yangtze River Delta, and the Pearl River Delta. Especially, the NO<sub>2</sub> concentrations over southern Hebei, northern Henan, central Shandong, and southern Shaanxi exceeded the level 2 standard of the Chinese National Ambient Air Quality Standard (40 µg/m<sup>3</sup>).

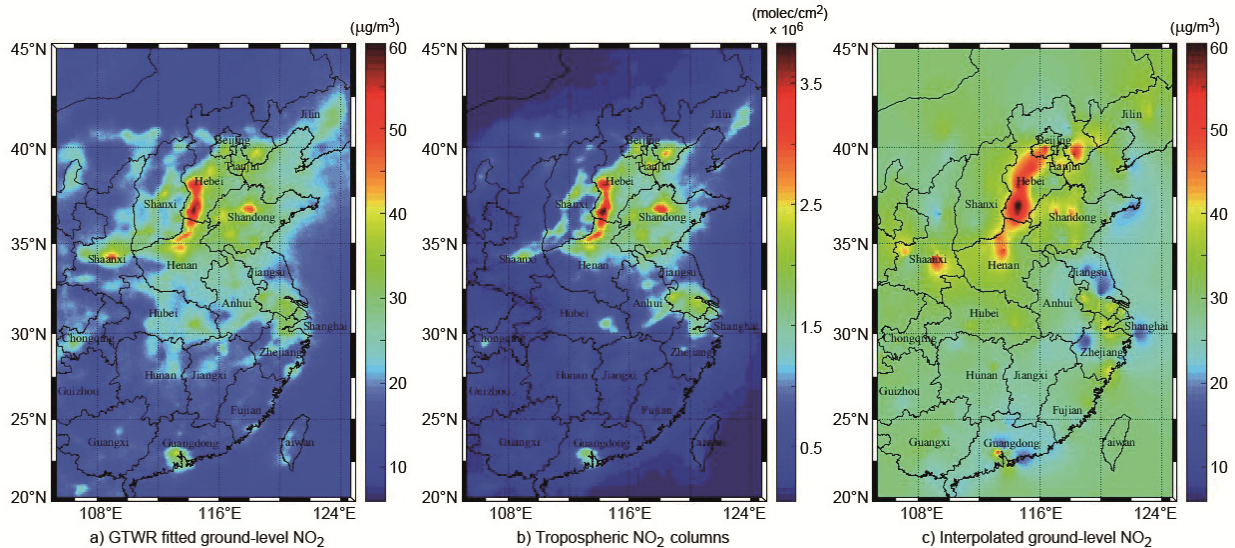


Fig. 3-16: Spatial distribution of annually mean values of (a) ground level NO<sub>2</sub> concentrations fitted by the GTWR model, (b) NO<sub>2</sub> tropospheric columns, and (c) ground level NO<sub>2</sub> concentrations interpolated by the Kriging method.

### References

- Huang, B., Wu, B., Barry, M.: Geographically and temporally weighted regression for modeling spatio-temporal variation in house prices. *Int. J. Geogr. Inf. Sci.*, 24, 383-401, 2010.
- Qin, K., Rao, L., Xu, J., Bai, Y., Zou, J., Hao, N., Li, S., Yu, C.: Estimating Ground Level NO<sub>2</sub> Concentrations over Central-Eastern China Using a Satellite-Based Geographically and Temporally Weighted Regression Model. *Remote Sensing*, 9, 950, 2017.

### 3.7 Aeolus Mie and Rayleigh Algorithm Performance Assessment

*K. Schmidt, O. Reitebuch (IPA), D. Huber (DoRIT)*

The main goal of ESA's Aeolus mission consists in the acquisition of global vertical wind profiles from space using Lidar technology to improve the accuracy of weather and climate prediction. The Aeolus satellite will carry a Doppler wind Lidar, called ALADIN, which will probe the lowermost 30 km of the atmosphere at a wavelength of 355 nm. It will measure Doppler shifts in the spectra of the laser light backscattered by moving atmospheric particles such as aerosols, cloud particles, and air molecules. Therefore both a Mie and a Rayleigh spectrometer are used and line-of-sight wind velocities can be derived. The launch is scheduled for September 2018.

In 2016, ESA decided to switch from the foreseen higher satellite orbit of about 400 km altitude to a lower one of about 320 km in order to improve the quality of the expected wind data. In 2017, a variety of platform and ALADIN instrument tests have been performed. As a result, the Aeolus End-to-End Simulator (E2S) and the processors have been adapted for the new orbit and instrument parameters. Note that the E2S simulates the measurement flow for different atmospheric scenarios including wind conditions. Annotated instrument source packet data, suitable for L0-L1A-L1B processing, are the output of these simulations. Comparisons between the E2S input and the resulting L1B Mie and Rayleigh channel winds allow assessing the algorithms and parameter settings.

In the current pre-launch phase, the E2S and the processors are further tested and updated on the basis of the new orbit and instrument parameters. In doing so, simple atmospheric conditions like constant vertical wind and temperature profiles are considered in order to see the effects of the different algorithm and instrument settings more clearly.

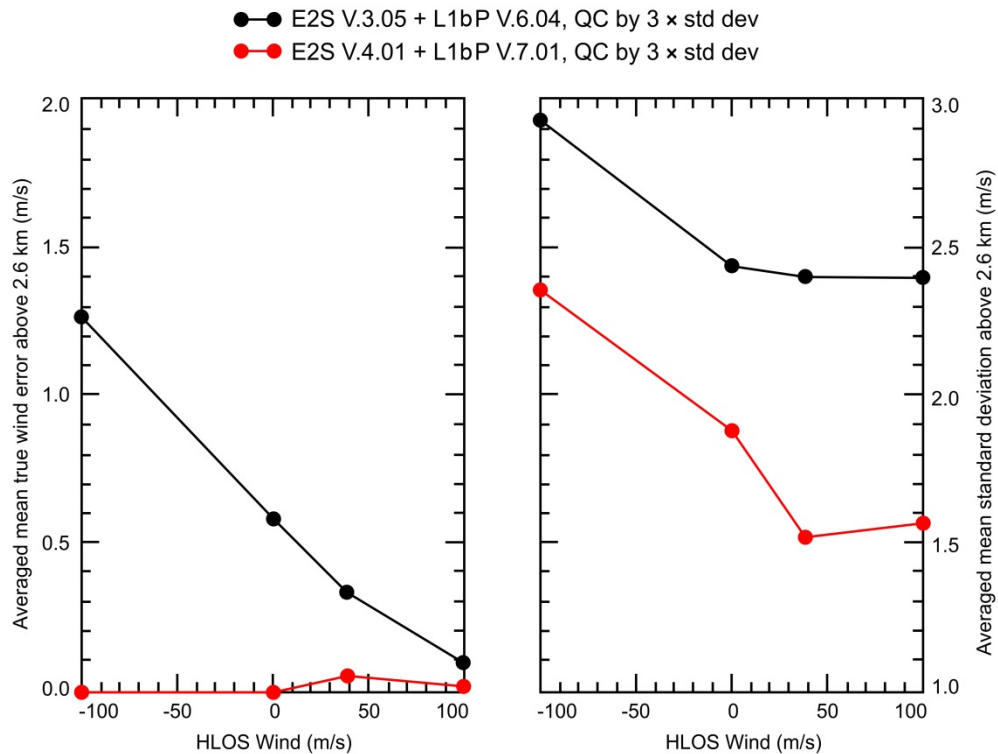


Fig. 3-17: Comparisons of the mean true wind errors (left) and standard deviations (right), both averaged over all their values above 2.6 km altitude, of the L1bP Rayleigh wind results obtained by different E2S-L1bP software versions and quality controlled (QC) by 3 × the standard deviation, for different E2S input horizontal line-of-sight (HLOS) winds.

Fig. 3-17 shows an example of such investigations. It has been obtained for constant E2S input wind profiles of 0 m/s, 38.7 m/s, and ±100 m/s, and for a constant temperature profile of -20° C. The L1bP Rayleigh wind errors, obtained by different E2S-L1bP versions and quality controlled (QC) by 3 × the standard deviation, are compared (for details concerning the quality control procedure, applied to the L1bP winds, see *Schmidt et al. (2017)*, section 6.1, the altitude averaging procedure is described there in section 6.4). Note that (E2S V.3.05 + L1bP 6.04) represents the older software version still accounting for the older higher orbit of about 400 km and the older parameter settings, while (E2S V.4.01 + L1bP 7.01) is the most recent version. It is seen that the L1bP Rayleigh wind errors, obtained by the new version, are clearly smaller than those of the older version. This shows that the combination of the lower orbit and the new instrument parameters can lead to an improved wind data quality, as expected.

### References

*Schmidt, K., Reitebuch, O., and Huber, D.*: Technical Note 51.2: Mie and Rayleigh Algorithm Performance Assessment. AE.TN.DLR.5100.2.20170207, V.1.3, February 7, 2017.

### 3.8 VirES for Aeolus

M. Meringer, T. Trautmann, D. Huber (DoRIT), O. Lux, O. Reitebuch, F. Weiler (all IPA), M. Pačes, D. Santillan, C. Schiller, F. Schindler, G. Triebnig (all EOX)

VirES is the Virtual workspace for Earth-observation Scientists, a service provided by the European Space Agency (ESA). The Austrian IT company EOX leads the development team. VirES has firstly been established for ESA's magnetic field mission SWARM as "VirES for SWARM" (Pedrosa and Triebnig 2016). VirES is a web-based service (<https://vires.services>) that enables scientists to discover, visualize, select and download data of Earth Observation missions through an easy to operate graphical user interface (GUI). In 2017 ESA/ESRIN awarded a further contract to EOX for adapting and extending VirES to provide a similar service for ESA's atmospheric dynamics mission Aeolus which is scheduled for launch in 2018. IMF, IPA and DoRIT are involved as subcontractors and cooperation partners in this project to provide mission-specific scientific and technical knowledge. The joint proposal was submitted to ESA in February 2017 and the Kick-Off meeting took place in April. First versions of the technical documentation were delivered to ESA during the following months, including the User Requirements Document (URD), the VirES Data Dictionary Aeolus (VDDA) and the Algorithm Design Technical Note (AD-TN). Further documents are in preparation or scheduled for the first quarter of 2018, such as the Acceptance Test Plan & Procedures (ATPP) and the Acceptance Test Report (ATR). The latter two are the major contributions of IMF-ATP.

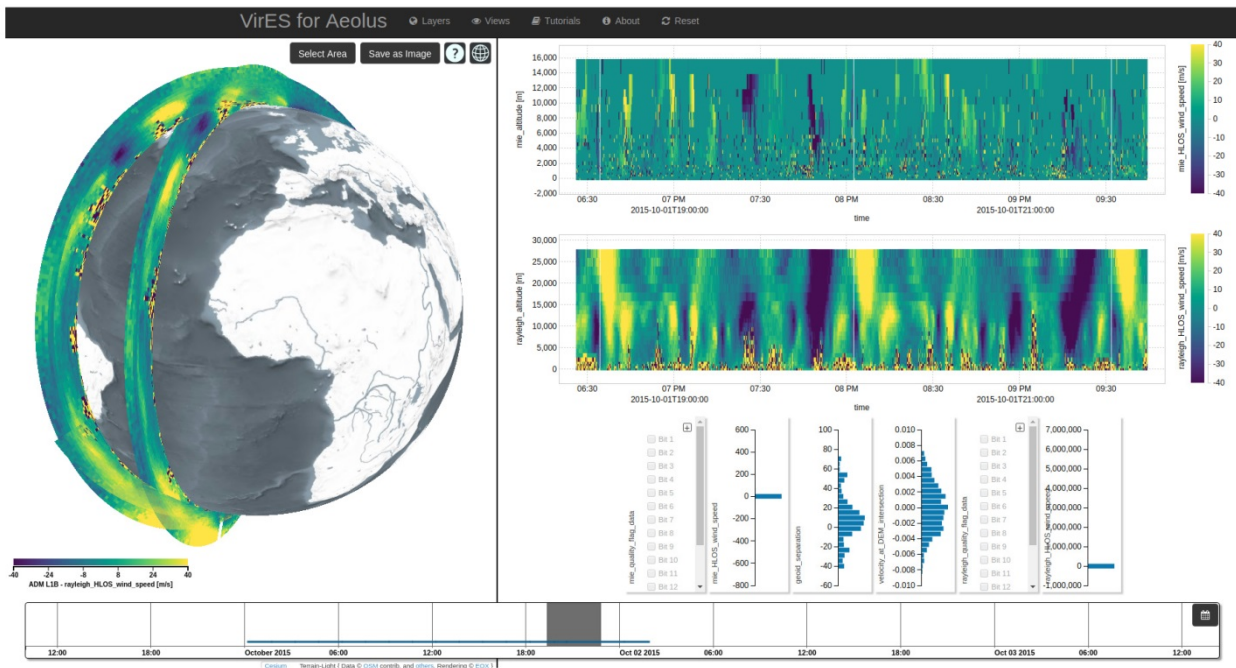


Fig. 3-18: Screenshot of the VirES-Aeolus GUI.

VirES-Aeolus will provide access to Aeolus L1B, L2A, L2B, L2C products and the very important auxiliary data (Costa *et al.* 2017). The GUI is accessible through various internet browsers. A first release for testing activities has become available for team members in December 2017. Fig. 3-18 illustrates a screenshot of the GUI, where the following control panels can be identified:

- At the bottom there is the time slider where the user selects the time range of the data to be analyzed.
- On the left hand side the VirES globe widget provides a three-dimensional visualization of the selected data corresponding to its latitude, longitude and altitude. In the screenshot we see the measurement data as vertical curtains.
- Right of the globe widget there is the VirES analytics panel widget. It is composed of two scatter plot panes on top (one for the Mie and one for the Rayleigh channel) and multi-parameter histogram displays at the bottom for data filtering purposes.

New users will be introduced to details of the GUI by tutorials that are also available online. The service is planned to be ready for operational use at the end of the mission's commissioning phase.

### References

*Pedrosa, D.S., Triebnig, G.: Visual Analysis of SWARM and Geomagnetic Model Data. Proceedings Living Planet Symposium 2016, ESA SP-740, 2016.*

*Costa, G., Reitebuch, O., Triebnig, G.: Aeolus VirES Tool. ADM-Aeolus CALVAL Rehearsal Workshop. Toulouse, France, 2017.*

## **3.9 Linearized Radiative Transfer Model for the Retrieval of Cloud Properties from DSCOVER-EPIC**

*V. Molina García, S. Sasi, D. Efremenko, A. Doicu, D. Loyola*

Previously we had analyzed exact and approximate radiative transfer models regarding their applicability to the retrieval of cloud parameters from EPIC measurements (*Molina García et al. 2017a*). We showed that the exact Discrete Ordinate method with Matrix Exponential (DOME) and the Matrix Operator method with Matrix Exponential (MOME) by using the correlated k-distribution method in conjunction with the Principal Component Analysis (PCA) technique satisfy the accuracy and efficiency requirements for this application. However, the retrieval of atmospheric properties from satellite measurements also requires the knowledge of the partial derivatives of the measured radiance with respect to the properties to be retrieved. There are two common linearization approaches, namely the

- linearized forward approach, where the partial derivatives are computed analytically, and the
- forward-adjoint approach, where the measured radiance is expressed as the scalar product of the solution of the adjoint problem and the source function of the forward problem. Using the linearization technique to the forward and adjoint problems, we can obtain analytical expressions for the partial derivatives.

One important advantage from the forward-adjoint approach is its notable efficiency, because only two radiative transfer calculations are required for computing the partial derivatives. We performed several analyses to find the optimal linearized radiative transfer model within the scope of EPIC measurements to compute the partial derivatives of the radiance with respect to the cloud optical thickness  $\tau_c$  and the cloud top height  $h_t$  (*Molina García et al. 2017b*).

For this purpose, we simulated channel 9 of the EPIC instrument (an O<sub>2</sub> A-band absorption channel at 764 nm with a bandwidth of 1.0 nm). The models analyzed are the Linearized Discrete Ordinate method with Matrix Exponential (LDOME), the Linearized Matrix Operator method with Matrix Exponential (LMOME), and the forward-adjoint approach using the Discrete Ordinate method with Matrix Exponential (FADOME). The derivatives with respect to the cloud geometrical parameters are computed by homogenizing the layers containing the cloud top and bottom heights. The water-cloud model is the same as in *Molina García et al. (2017a)*, the ground is described as a Lambertian surface with albedo  $A = 0.2$ , the solar and viewing zenith angles are  $\theta_0 = \theta = 30^\circ$ , and the relative azimuthal angle is  $\Delta\phi = 176^\circ$ . We already had found that 32 streams per hemisphere is a good compromise between an accurate description of the scattering in the backward direction and the computation time (*Molina García et al. 2017a*). Thus, we fixed the number of streams to this value for all the simulations of the partial derivatives of the measured radiance.

The numerical simulations showed that the three models provide similar results when computing the derivatives with respect to the cloud optical thickness  $\tau_c$  and the cloud top height  $h_t$ . The forward-adjoint approach based on DOME, and using the correlated k-distribution method in conjunction with the PCA technique, is an accurate and efficient tool for the offline retrieval of cloud optical thickness and cloud top height from EPIC measurements, with a speed-up factor of 2 when compared to the conventional linearization approaches (Table 3-3 and Fig. 3-19).

Acceleration techniques	Linearized models		
	LDOME	LMOME	FADOME
LBL calculation	227 min	288 min	113 min
Correlated k-distribution	42 min	54 min	21 min
PCA technique	30 s	36 s	23 s
Corr. k-distribution plus PCA	23 s	28 s	13 s

Table 3-3: Computation times to simulate the partial derivatives of the measured radiance (EPIC channel 9) with respect to the cloud optical thickness for different models (LDOME, LMOME, FADOME) and acceleration techniques.

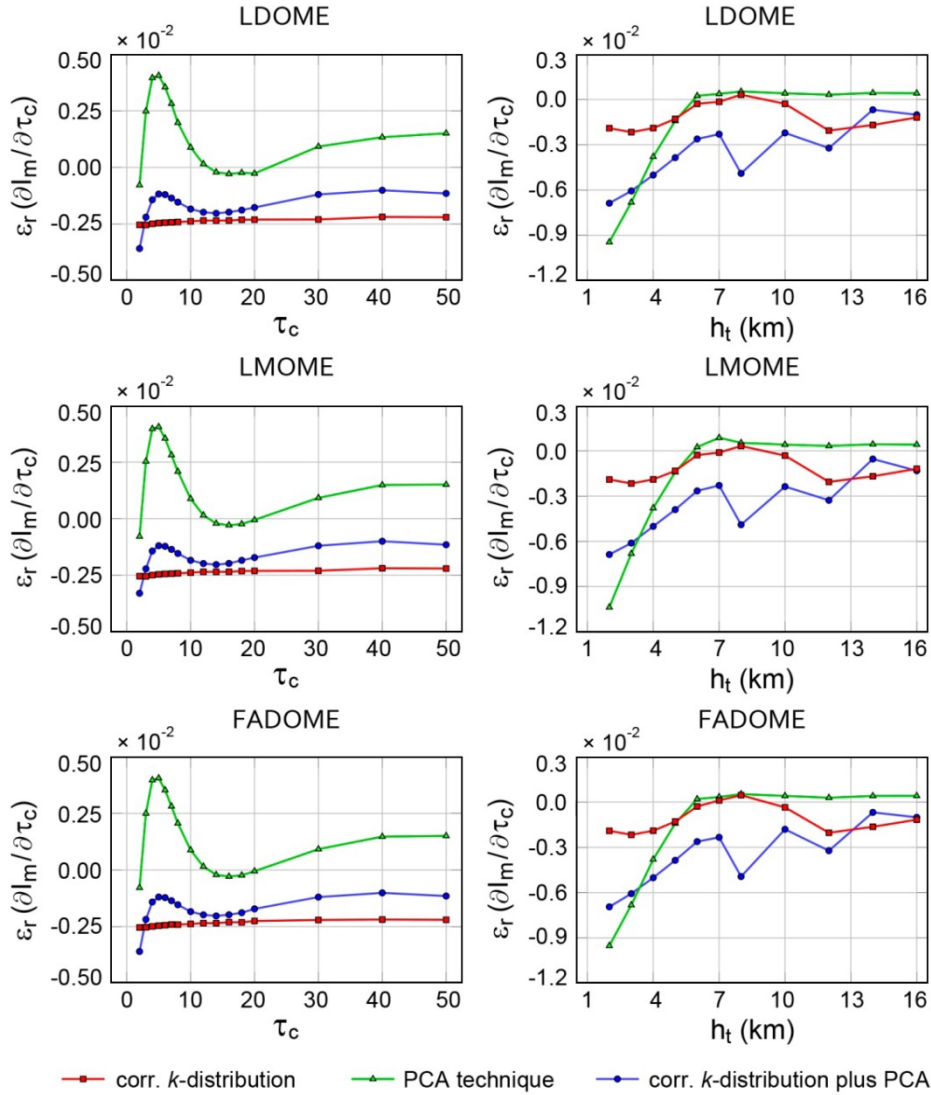


Fig. 3-19: Relative errors in  $\partial I_m / \partial \tau_c$  (left panels) and  $\partial I_m / \partial h_t$  (right panels) when comparing LbL-based simulations with those for correlated k-distribution, PCA technique, and correlated k-distribution plus PCA.

### References

Doicu, A., Trautmann, T.: Discrete-ordinate method with matrix exponential for a pseudo-spherical atmosphere: Scalar case. *J. Quant. Spectros. & Radiat. Transfer*, 110 (1-2), 146-158. doi:10.1016/j.jqsrt.2008.09.014, 2009.

Efremenko, D.S., Molina García, V., Gimeno García, S., Doicu, A.: A review of the matrix-exponential formalism in radiative transfer. *J. Quant. Spectros. & Radiat. Transfer*, 196, 17-45. doi:10.1016/j.jqsrt.2017.02.015, 2017.

Doicu, A., Trautmann, T.: Adjoint problem of radiative transfer for a pseudo-spherical atmosphere and general viewing geometries. *J. Quant. Spectros. & Radiat. Transfer*, 110 (8), 464-476. doi:10.1016/j.jqsrt.2009.01.027, 2009.

Molina García, V., Sasi, S., Efremenko, D.S., Doicu, A., Loyola, D.: Radiative transfer models for retrieval of cloud parameters from EPIC/DSCOVR measurements. *J. Quant. Spectros. & Radiat. Transfer* (in review), 2017a.

Molina García, V., Sasi, S., Efremenko, D.S., Doicu, A., Loyola, D.: Linearized radiative transfer models for retrieval of cloud parameters from EPIC/DSCOVR measurements. *J. Quant. Spectros. & Radiat. Transfer* (in review), 2017b.

### 3.10 UPAS-2 Parallelization Concept

*F. Romahn, M. Pedernana, W. Zimmer, H. Bauer*

In recent years the spatial resolution provided by the atmospheric sensors has increased dramatically. This implicates that the number of ground pixels included in the level 0 data has grown significantly over the last two decades: GOME-1, in the mid 90s, producing roughly 80 MBs of level 1 data per single orbit while the most recent TROPOMI / Sentinel-5 Precursor (S5P) mission, which was launched on October 13, 2017, generates roughly 50 GB per orbit (Table 3-4). This is a big challenge for the level 2 processing where the retrieval of trace gases occurs under the same timeliness requirements specification, independently of the amount of ground pixels to be processed.

Sensor	Timeframe	Size Level 1b for one Orbit
GOME-1	1995-2011	80 MB
SCIAMACHY	2002-2012	~200 MB
GOME-2	since 2006	~ 800 MB
OMI	since 2003	~400 MB
S5P	since 2017	~50 GB

Table 3-4: Data volumes per L1B orbit for various atmospheric sensors.

In order to cope with such amount of level 1 data, it was essential to exploit the parallelization capabilities of modern CPUs for the level 2 processing. Unlike UPAS-1, UPAS-2 was developed having this goal in mind from the beginning. Therefore we used the openMP architecture, as one of its main tasks was the level 2 processing of S5P data.

However, making use of parallelization in a processor is not a straightforward task. A critical design decision is the granularity of the parallelization. For example, one possibility would be to parallelize at ground pixel level (Fig. 3-20 "Per Pixel"). It implies that each pixel is assigned to a different thread which computes in parallel. This approach would be quite easy to implement but has the disadvantage of a big overhead as the assignment of pixels to threads happens very frequently. As there is also no vectorization possible, this results in a low throughput. Another approach is to parallelize the different algorithms themselves, e.g. the radiative transfer model (Fig 3-20 "RT Async"). This method is very efficient as the threads could share most of their input data. On the other hand, the effort regarding the implementation would be very high. In the end it was decided to perform the parallelization at scanline level for UPAS-2 (Fig. 3-20 "Per Scan"). This way, each scanline is assigned to a different thread. It allows for vectorization and also higher throughput than the pixel-wise approach but still has a very moderate implementation effort.

In order to achieve the best scalability with parallelization, the implementation of algorithms, compared to the single threaded case, also had to be slightly optimized. For example, each memory allocation usually blocks the threads until the data is provided and thus hampers the overall performance. Therefore UPAS-2 uses a workspace concept for the threads which allocates all necessary memory only

once at the start of the processor. Then it can be used as temporary data space without having to be allocated again. This approach, together with other optimizations leads to a fairly good scalability as can be seen in Figure 3-21.

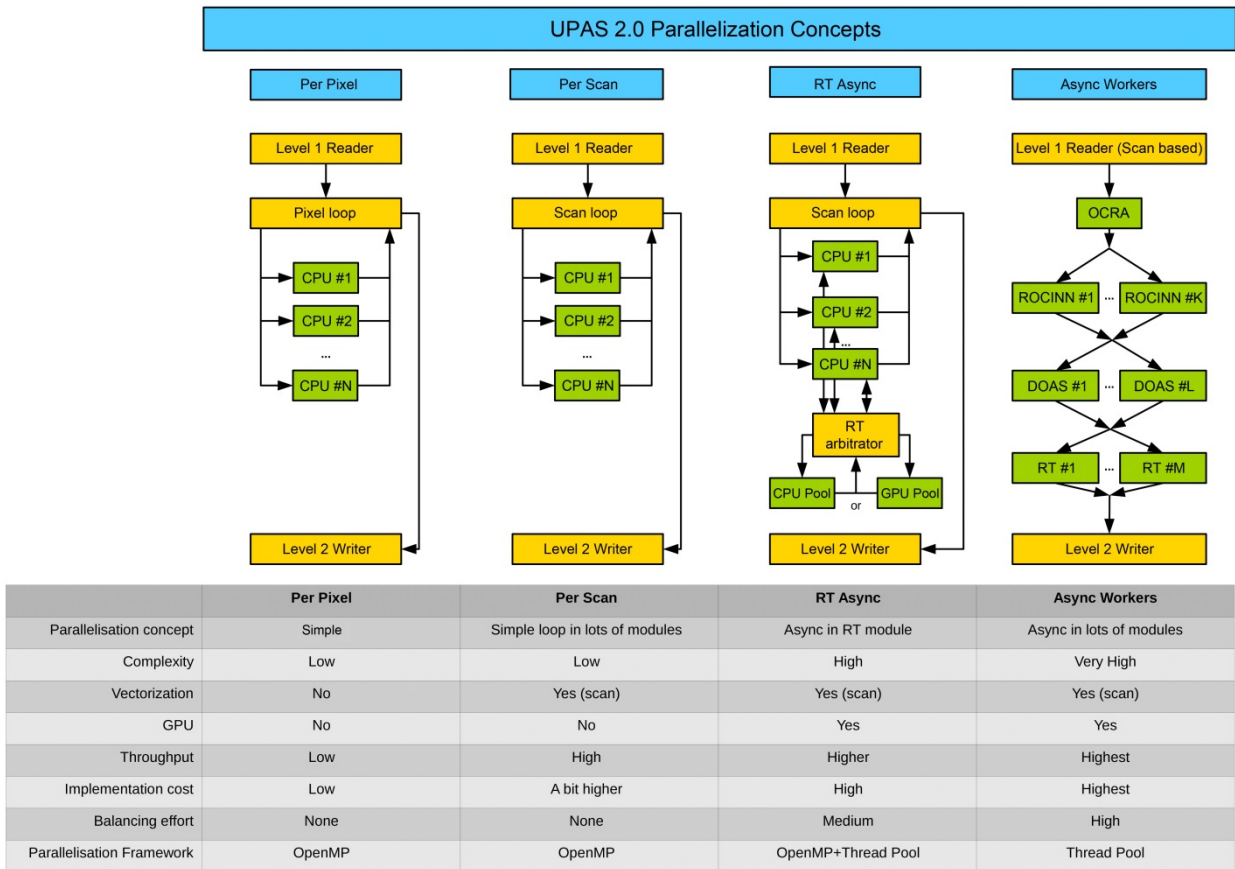


Fig. 3-20: Possible parallelization concepts for UPAS-2.

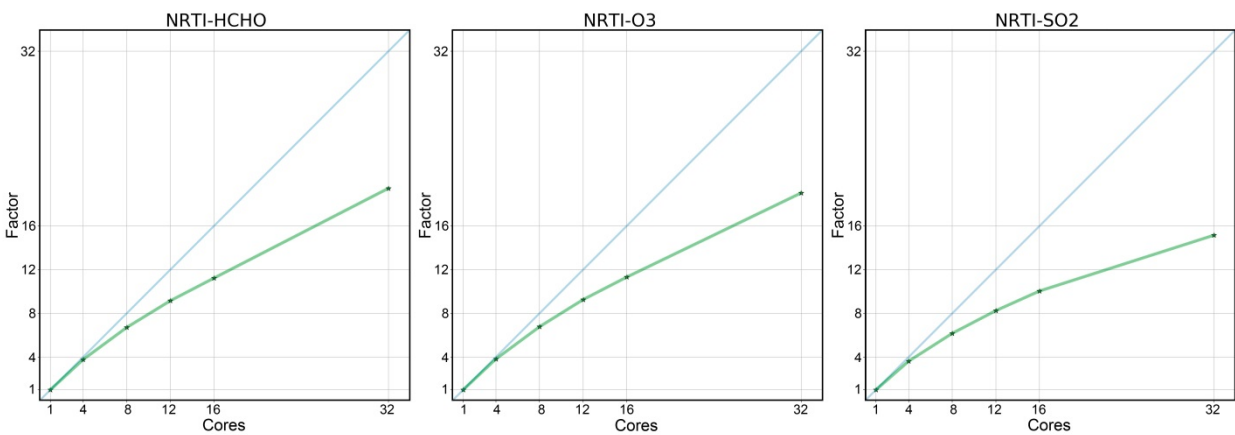


Fig. 3-21: Scalability of UPAS-2 with respect to the number of threads (cores) used for retrieving the NRT products HCHO, O<sub>3</sub> and SO<sub>2</sub>. The benchmarks were performed on a machine with 2x Intel Xeon E5-2695 (2.1 GHz, 18 cores, 36 threads, 45MB cache) and 64 GB RAM.

For the future it is planned to generalize ground pixels and scanlines to the concept of the processing unit. It could basically be seen as a moving window over the whole orbit swath with the dimensions being configurable, e.g. a 3 × 3 or 10 × 2 ground pixel processing unit. Such a concept may be necessary for some algorithms which require information about neighboring pixels. The parallelization would then be performed at processing unit level, an approach which would open up other interesting possibilities, e.g. like row-wise parallelization.

### 3.11 Estimating Ozone Profile Shapes from GOME-2 Measurements using FP-ILM

*J. Xu, D. Loyola, F. Romahn, A. Doicu, K.-P. Heue, M. Coldewey-Egbers*

To efficiently and reliably estimate ozone profile shapes from nadir-viewing satellite UV measurements, we have recently developed a retrieval algorithm called the “Full-physics Inverse Learning Machine (FP-ILM)”, see *Xu et al. (2017)*. Essentially, the implementation of FP-ILM (Fig. 3-22) comprises a training phase to derive an inverse function from synthetic satellite measurements using the radiative transfer model VLIDORT in conjunction with the “smart sampling” technique (*Loyola et al. 2016*), and an operational phase in which the inverse function is applied to real measurements.

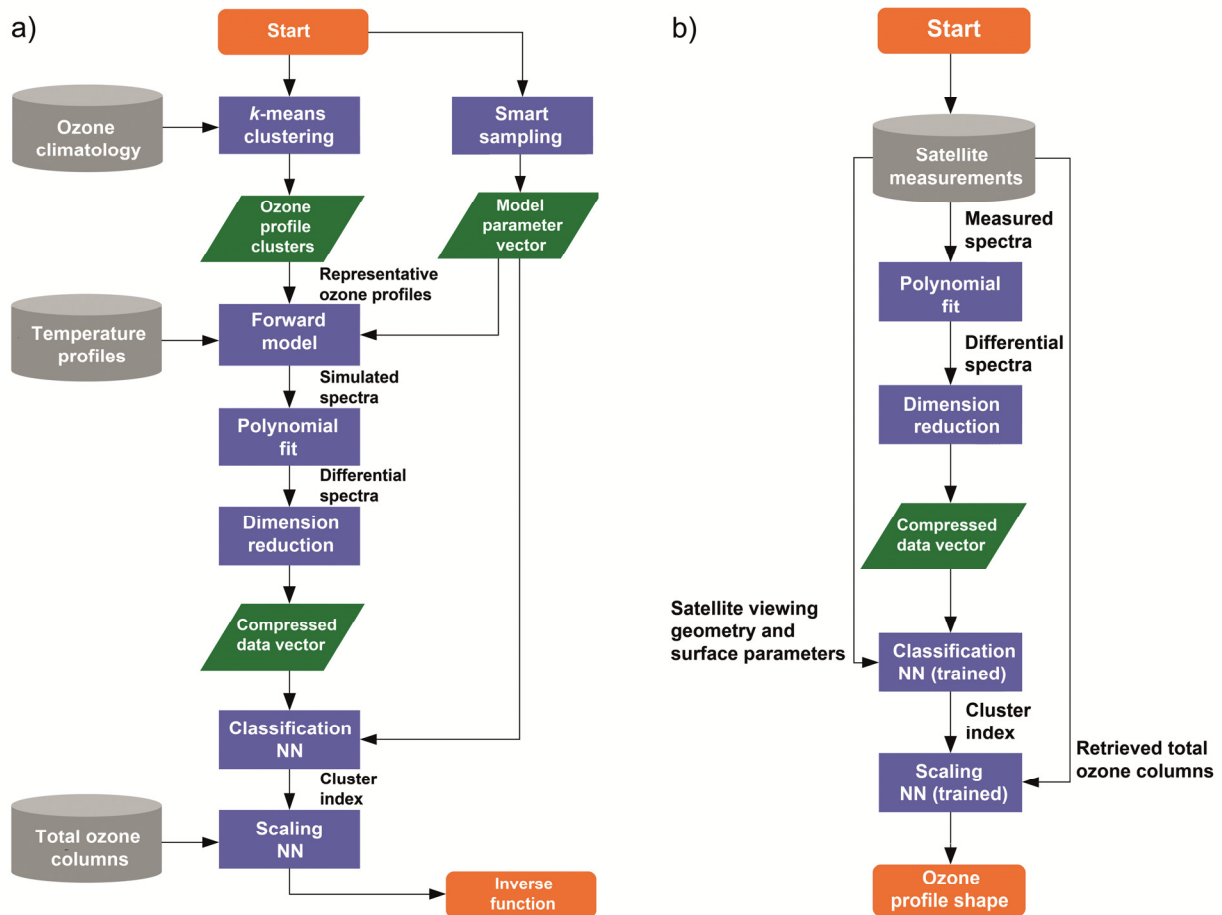


Fig. 3-22: Diagram of FP-ILM during its training (a) and operational (b) phases for retrieving ozone profile shapes.

In our case, the clustering process generates 11 ozone profile clusters from two climatologies with sufficient information in the troposphere and lower stratosphere. The classification is done via a neural network and the scaling process is implemented by a neural network ensemble with given total ozone columns.

We have applied FP-ILM to measurements obtained by GOME-2 on the MetOp-A satellite from four seasons in 2008 and compared the retrieved ozone profiles with the RAL retrieval algorithm based on the optimal estimation method (OEM). In Fig. 3-23, mean absolute differences and the corresponding standard deviation with respect to 11 clusters demonstrate that the retrieved ozone profiles between both algorithms tend to reach a good agreement with less than 6 DU differences in most cases. The relative differences are mostly within 5-20% that are mainly found at lower altitudes where the RAL-OEM scheme relies on the a priori information.

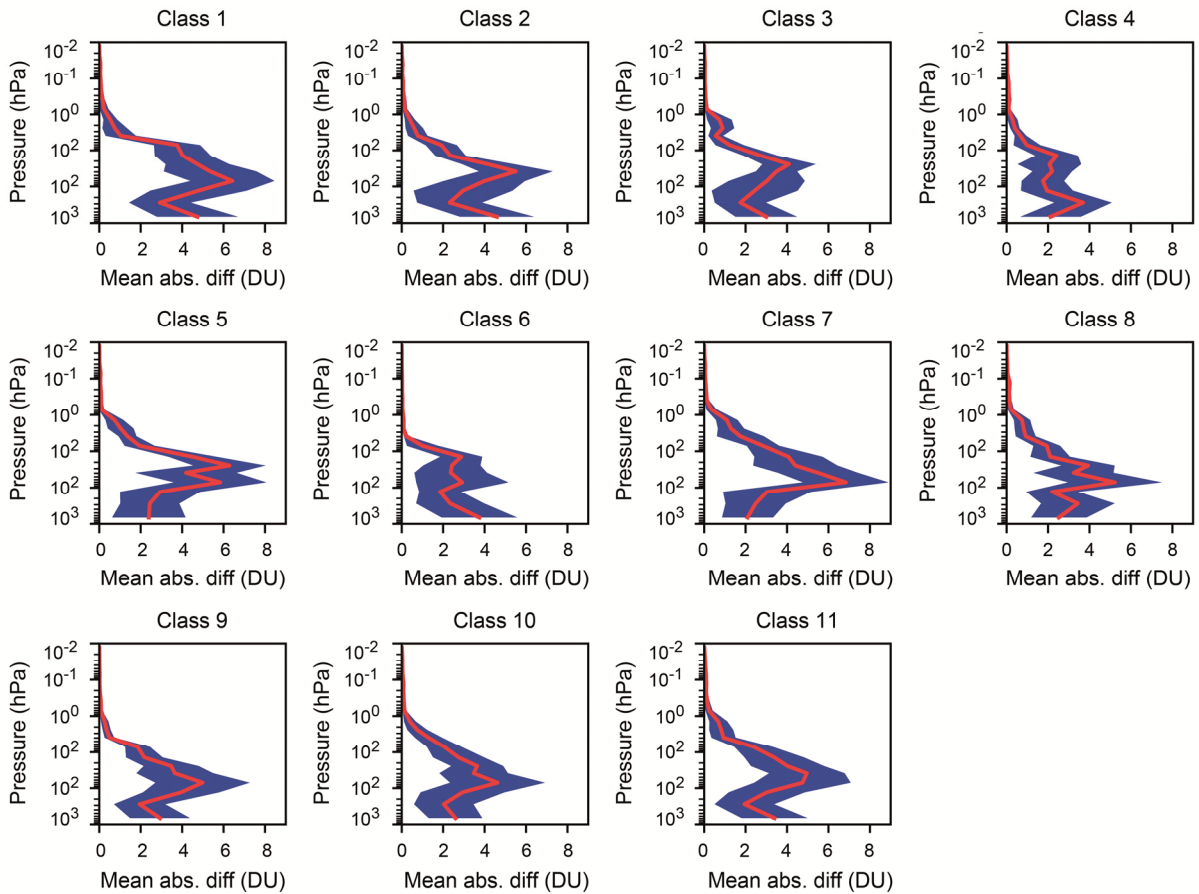


Fig. 3-23: Mean absolute differences of estimated ozone profiles between FP-ILM and RAL-OEM. Blue area indicates the corresponding standard deviation.

The FP-ILM algorithm employs machine learning tools to characterize ozone vertical distributions in a robust way and can be easily adapted to other hyperspectral UV instruments. The integration of the FP-ILM prototype into the UPAS-2 is currently ongoing, which will be tested for near-real-time processing of TROPOMI/S5P measurements. Future work will also focus on comparison of total and tropospheric ozone column retrievals using FP-ILM profiles with conventional approaches.

### References

- Loyola R.D., Pedernana, M., Gimeno García, S.: Smart sampling and incremental function learning for very large high dimensional data. *Neural Networks*, 78, 75-87, doi:10.1016/j.neunet.2015.09.001, 2016.
- Xu, J., Schüssler, O., Loyola R.D., Romahn, F., Doicu, A.: A Novel Ozone Profile Shape Retrieval Using Full-Physics Inverse Learning Machine (FP-ILM). *IEEE Journal of Selected Topics in Applied Earth Observations and Remote Sensing*, 10(12), 5442-5457, doi:10.1109/JSTARS.2017.2740168, 2017.

### 3.12 Stochastic Radiative Transfer Models

*D.S. Efremenko, A. Doicu, D. Loyola, T. Trautmann*

Most real natural media are inhomogeneous and can vary randomly in time and space. The radiative transfer in such media is a very broad topic, but still there is a lack of solution techniques in this field which are used in practice. Real clouds are an inhomogeneous three-dimensional scattering medium. For the new generation of satellite spectrometers with a relatively high spatial resolution, such as Sentinel-5 Precursor, Sentinel-4 and Sentinel-5, it is important to account for the sub-pixel cloud inhomogeneities, or at least, to assess their effect on the radiances at the top of the atmosphere, and in particular, on the trace gas and cloud retrieval results. This assessment has to be probabilistic since the detailed structure of the clouds is unknown and only a small number of statistical properties are given.

The classical approach for simulating the radiance field is based on multidimensional deterministic models. It has the following steps:

- simulation of sampling random realizations of an inhomogeneous cloudy field,
- solution of radiative transfer equation for each realization, and
- averaging of the obtained solutions over the ensemble of cloudiness realizations.

For each realization of a cloud field, a three-dimensional radiative transfer problem has to be solved by using either the Monte-Carlo method (*Marchuk et al. 1980*) or multi-dimensional solvers such as SHDOM developed by *Evans (1998)*. In both cases 3D-modeling is very time-consuming. Due to its computational complexity, this strategy is not used in operational retrieval algorithms.

The alternative approach relies on the stochastic radiative transfer models (SRTM), in which cloud fields are regarded as stochastic scattering media due to their internal inhomogeneity and stochastic geometry. New transport equations, relating the statistical parameters of the clouds to those of the radiance field, are derived. The goal of this approach is to obtain a relatively simple relationship between the statistical parameters of clouds and radiation that can be numerically evaluated in practice. Within this strategy, the computations of the radiance field can be organized as follows:

- simulation of random realizations of an inhomogeneous cloudy field,
- obtaining the relevant statistical structure information from a set of realizations of a cloudy field, and
- solution of the stochastic radiative transfer problem using as input the cloud statistics parameters obtained at the previous step.

The chapter we contributed recently to *Springer Series in Light Scattering (Efremenko et al. 2018)* contains an overview of the work related to this topic and conducted at our department. It provides a consistent description of the stochastic radiative transfer for atmospheric remote sensing. In particular, we have reviewed the stochastic radiative transfer models based on the analytical procedure of statistical averaging of the radiative transfer equation. By representing the radiance and the geometric fields as the sum of their mean values and their random fluctuations, we derived an  $n^{\text{th}}$ -order stochastic model for the solar radiation problem and arbitrary statistics. The stochastic model is expressed in matrix form, and is equipped with appropriate closure relations for the higher-order covariance terms. For broken clouds, the  $n^{\text{th}}$ -order stochastic model reduces to the first-order stochastic model for a two-dimensional radiance vector, whose entries are the mean radiance field and the covariance of the radiance and the indicator fields. Using SHDOM as a reference, we found that the stochastic cloud model is superior to the independent pixel approximation; the relative errors in the domain-averaged radiance are below 2% for the stochastic cloud model, and of about 10% for the independent pixel approximation.

Algorithms for cloud parameters (cloud optical thickness  $\tau_c$  and the cloud-top height  $H$ ) and ozone profiles retrievals are designed based on the SRTMs. The cellular cloud model of *Alexandrov et al. (2010)* is used. The examples of cloud fields are shown in Fig. 3-24. The retrieval accuracy for inhomogeneous cloud scenes is  $\sim 1\%$ . The use of a lookup table for stochastic clouds radiances in conjunction with multi-linear interpolation is robust and does not introduce performance bottlenecks in the retrieval algorithm. For ozone retrievals we have shown that the stochastic cloud errors can only be partially eliminated by a differential radiance model (used in DOAS) based on the independent pixel

approximation. The errors in the retrieved ozone total column are not significant, but the errors in the retrieved ozone partial columns may become large.

The SRTMs are efficient for predicting the shape of the Tikhonov function. If the Tikhonov function has only one minimum (as shown in Fig. 3-25 left), then the Gauss-Newton optimization method can be used. However, if there is a set of local minima (as shown in Fig. 3-25 right), it is likely that the Gauss-Newton techniques converge to a false minimum. In this case a global optimization methods, e.g. the genetic algorithm, should be used. In addition to that, it is shown that the SRTMs can be used for finding the optimal values of regularization parameters to minimize the errors induced by the cloud inhomogeneity.

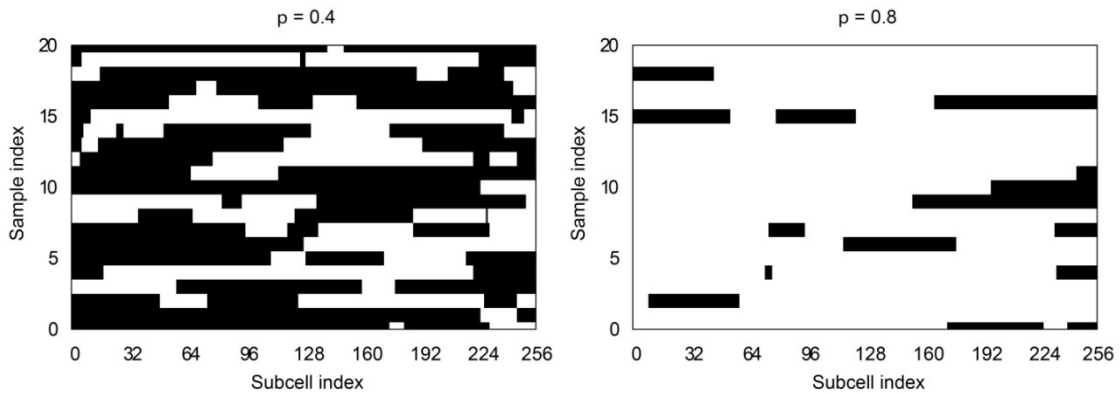


Fig. 3-24: Indicator function for the occupation probabilities  $p = 0.4$  and  $p = 0.8$  for 20 sample realizations: White zones correspond to the clouds while black zones correspond to the clear sky.

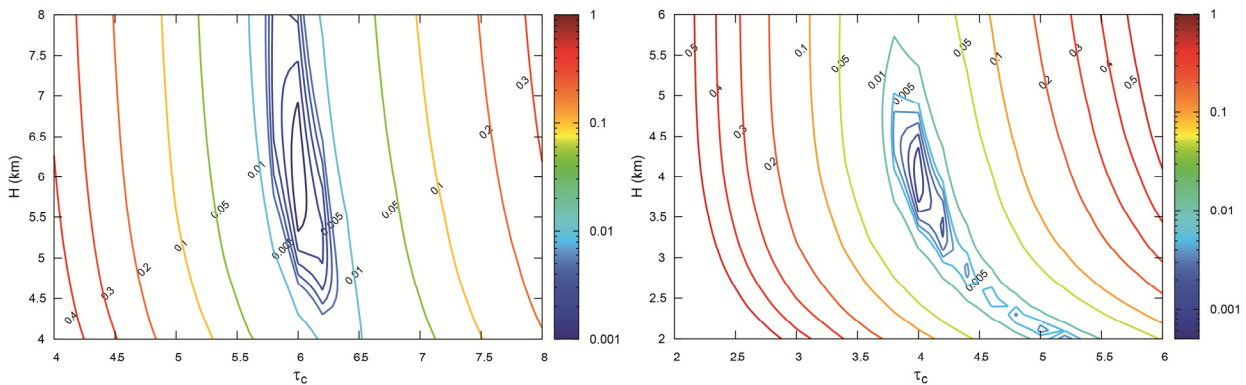


Fig. 3-25: Tikhonov functions in the cases ( $\tau_c = 6, H = 6$  km – left panel) and ( $\tau_c = 4, H = 4$  km – right panel).

The SRTM and retrieval algorithms presented in this chapter will allow the accurate retrieval of cloud and trace gas properties from the next generation of Copernicus atmospheric composition Sentinel missions.

### References

- Alexandrov, M.D., Marshak, A., Ackerman, A.S.: Cellular statistical models of broken cloud fields. Part I: theory. *Journal Atmospheric Science*, 67(7), 2125-2151, 2010.
- Efremenko, D.S., Doicu, A., Loyola, D., Trautmann, T.: Fast stochastic radiative transfer models for trace gas and cloud property retrievals under cloudy conditions. in *Springer Series in Light Scattering: Volume 1: Multiple Light Scattering, Radiative Transfer and Remote Sensing*, edited by A. Kokhanovsky: 231-277, 2018.
- Evans, K.F.: The spherical harmonic discrete ordinate method for three-dimensional atmospheric radiative transfer. *Journal Atmospheric Science*, 55(3), 429-446, 1998.
- Marchuk, G.I., Mikhailov, G.A., Nazarialiev, M.A. et al.: The Monte Carlo methods in atmospheric optics, Vol 12. *Springer Series in Optical Sciences*. Springer, Berlin, 1980.

### 3.13 Intercomparison of 3 Microwave/Infrared High Resolution LbL Radiative Transfer Codes

F. Schreier, M. Milz (Luleå University of Technology)

Line-by-line (LbL) modeling of atmospheric radiative transfer is essential for the analysis of a growing number of high resolution infrared (IR) and microwave remote sensing instruments. Because the quality of the retrieval products critically depends on the accuracy of the radiative transfer codes used as forward model in the inversion process, verification and validation of these codes is crucial, and accordingly several code intercomparisons have been performed. Here an intercomparison of three LbL codes developed independently for atmospheric sounding is presented: ARTS, GARLIC (MIRART) and KOPRA. Note that ARTS – MIRART and KOPRA – MIRART intercomparisons (including some other models) have already been performed in the context of the *Third International Radiative Transfer Modeling Workshop* and the AMIL2DA project, respectively (Melsheimer et al. 2005, von Clarmann et al. 2002).

ARTS – Atmospheric Radiative Transfer Simulator – is a public domain project initiated and developed jointly by the University of Hamburg and Chalmers University, Gothenburg (Bühler et al. 2005, Eriksson et al. 2011, see also <http://www.radiativetransfer.org>). It has originally focused on microwave applications with uplooking (MIAWARA, AMSOS), downlooking (AMSU-B, MHS) and limb viewing instruments (ODIN, SMILES).

GARLIC – Generic Atmospheric Radiation Line-by-line Infrared Code – is the modern Fortran2008 re-implementation of MIRART, originally designed for far and mid IR applications (Schreier et al. 2014, 2015) with arbitrary observation geometries, instrumental field of view and spectral response functions. Among others it has been used to simulate and analyze limb observations with MIPAS and TELIS (TeraHertz Limb Sounder), and thermal and near IR nadir spectra of AIRS, IASI, and SCIAMACHY. Furthermore it has also been applied to exoplanet atmospheric studies.

KOPRA – Karlsruhe Optimized and Precise Radiative transfer Algorithm – is a line-by-line, layer-by-layer model for forward calculation of infrared atmospheric transmittance and radiance spectra for various geometries and was specifically developed for the analysis of mid infrared limb emission sounder data (Stiller et al. 2002). It is used for retrievals of limb and uplooking instruments observing thermal emission and solar absorption spectra (MIPAS – balloon or aircraft, GLORIA or ground based FTIR).

In this intercomparison we consider a thermal infrared nadir sounding application and model the upwelling radiation seen by a space-borne, vertically downlooking observer. In particular we use a HIRS (High resolution Infrared Radiation Sounder) setup and compute radiances for the 19 HIRS infrared channels and a set of 42 atmospheric profiles (the Garand et al. (2001) dataset, comprising pressure, temperature, water vapor, carbon dioxide, ozone etc., defined on 43 altitude levels) representative of most meteorological situations. Absorption of the main molecular absorbers in the infrared is considered ( $O_2$ ,  $N_2$ ,  $H_2O$ ,  $CO_2$ ,  $O_3$ ,  $CH_4$ ,  $N_2O$ , and  $CO$ ) with line spectroscopic data taken from the HITRAN database and additional continuum corrections.

The radiance spectra, i.e. the monochromatic spectra convolved with the HIRS channel functions, converted to equivalent brightness temperatures are visually identical for all 42 Garand atmospheres. A detailed analysis of brightness temperature differences indicates a good agreement between ARTS, GARLIC, and KOPRA for most channels with differences in the sub-Kelvin range, in the same magnitude as reported for the LbL models participating in the Garand et al. (2001) study. However, larger deviations of up to a few Kelvin are observed for a few channels. Potential causes for the discrepancies had been discussed: continua ( $H_2O$ ,  $CO_2$ , ....., notably different versions of the (MT-)CKD continuum), different line strength conversion schemes, various LbL optimization schemes (wing truncation, weak line rejection, .....,), evaluation of path integrals, etc. Switching off the continuum contributions significantly reduced the differences in all but one channel. Furthermore, the impact of the atmospheric layer discretization has been demonstrated with a dense 85 level version of the Garand data set.

In conclusion, the codes generally agree quite well with deviations less than 1 K except for a few channels and/or atmospheres. Averaging over all atmospheres (Fig. 3-26), discrepancies are smaller than 0.5 K except for a few channels, mostly due to the choice of the continuum model used.

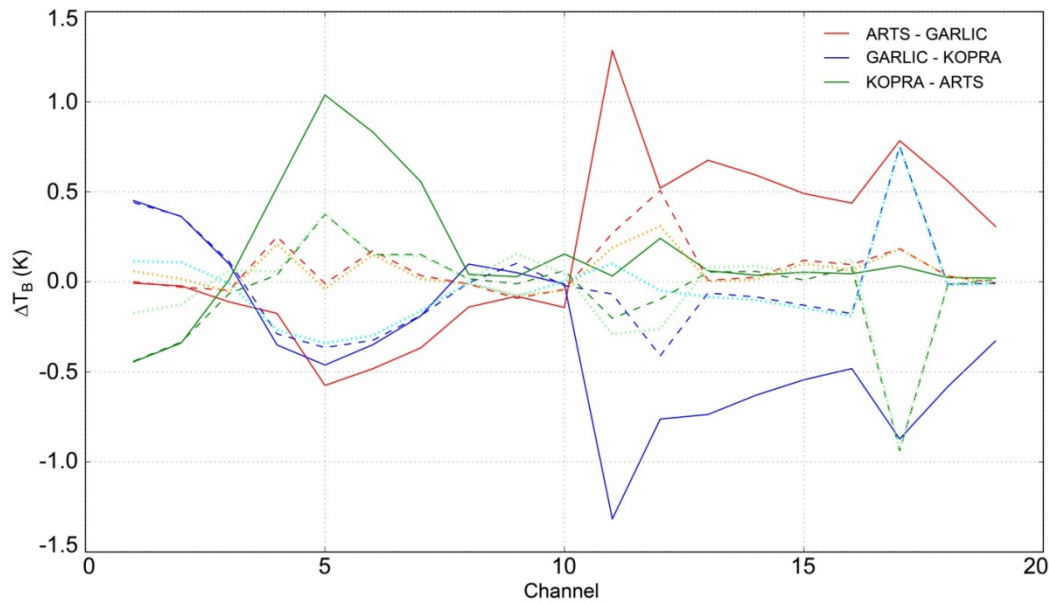


Fig. 3-26: Difference brightness temperatures averaged over all atmospheres as a function of channel number. Solid lines: 43 level atmosphere with continuum, dashed lines: without continuum, dotted lines: 85 level atmosphere without continuum.

### References

- Buehler, S.A., Eriksson, P., Kuhn, T., et al.: A. von Engeln, and C. Verdes. ARTS, the atmospheric radiative transfer simulator. *J. Quant. Spectros. & Radiat. Transfer*, 91, 65-93, 2005.
- Eriksson, P., Buehler, S.A., Davis, C.P., et al.: ARTS, the atmospheric radiative transfer simulator, version 2. *J. Quant. Spectros. & Radiat. Transfer*, 112(10), 1551-1558, 2011.
- Garand, L. et al.: Radiance and jacobian intercomparison of radiative transfer models applied to HIRS and AMSU channels. *Journal Geophys. Research*, 106(D20), 24017-24031, 2001.
- Melsheimer, C., Verdes, C., Buehler, S.A., et al.: Intercomparison of general purpose clear sky atmospheric radiative transfer models for the millimeter/submillimeter spectral range. *Radio Science*, 40, RS1007, 2005.
- Schreier F., Gimeno Garcia, S., Hedelt, P., Hess M., Mendrok, J., Vasquez, M. and Xu, J.: GARLIC – A General Purpose Atmospheric Radiative Transfer Line-by-Line Infrared-Microwave Code: Implementation and Evaluation. *J. Quant. Spectros. & Radiat. Transfer*, 137, 29-50, 2014.
- Schreier F., Gimeno Garcia, S., Vasquez, M., Xu, J.: Algorithmic vs. finite difference Jacobians for infrared atmospheric radiative transfer. *J. Quant. Spectrosc. & Radiat. Transfer*, 164, 147-160, 2015.
- Schreier, F., Milz, M., Buehler, S.A., von Clarmann, T.: Intercomparison of Three Microwave/Infrared High Resolution Line-by-Line Radiative Transfer Codes. *J. Quant. Spectros. & Radiat. Transfer*, in press, doi 10.1016/j.jqsrt.2018.02.032, 2018.
- Stiller, G.P., von Clarmann, T., Funke, B., et al.: Sensitivity of trace gas abundances retrievals from infrared limb emission spectra to simplifying approximations in radiative transfer modelling. *J. Quant. Spectros. & Radiat. Transfer*, 72, 249-280, 2002.
- von Clarmann, T., Höpfner, M., Funke, B., et al.: Modeling of atmospheric mid-infrared radiative transfer: The AMIL2DA algorithm intercomparison experiment. *J. Quant. Spectros. & Radiat. Transfer*, 78, 381-407, 2002.

### 3.14 Atmosphere-water Coupled Radiative Transfer – Actual Status of Validation

*D.S. Efremenko, T. Trautmann*

The radiative transfer (RT) solver Pydome for the coupled atmosphere-water systems is being developed as a part of the AC2020 project. The solver is implemented in Python and has the following features:

- the kernel of the solver is based on the discrete ordinate method with matrix exponential (ME) (*Doicu and Trautmann 2009*),
- the interface between atmosphere and ocean can be described as a flat surface or as rough surface using the Cox-Munk model (*Thomas and Stamnes 2002*),
- the computations of the weighting functions (Jacobians) are performed by using automatic differentiation approach via operator overloading,
- for efficient computations of hyperspectral data, the dimensionality reduction of input optical data is adopted.

Previously, the kernel of the RT module was validated against well-recognized RT models such as SCIATRAN, LIDORT, DISORT, PSTAR etc. The radiance field computed at the layer boundaries was inter-compared. Corresponding results were reported in our previous annual reports.

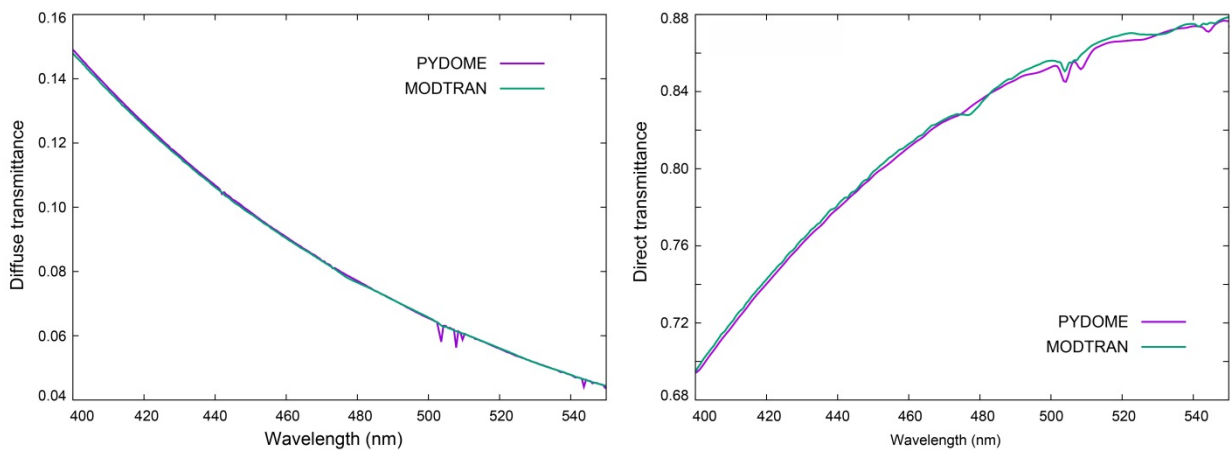


Fig. 3-27: Diffuse transmittance and direct transmittance computed with the Pydome model and MODTRAN – Rayleigh atmosphere.

In 2017 our work was focused on implementation/validation of the whole computational chain starting with atmospheric parameters for calculating the radiance field and the quantities derived from it, such as direct and diffuse transmittance, the spherical albedo. As a reference we used MODTRAN. Some results of the validation are shown in Fig. 3-27 for the Rayleigh atmosphere. The artifacts are due to differences in the convolution routines and atmospheric layering.

The RT kernel has been improved as well. It is known that in the ME formalism the solution is derived at layer boundaries with no explicit information about the solution behavior inside a given layer, while the direct usage of the ME propagator (one-point boundary value problem) is impossible in practice due to positive exponential terms (*Efremenko et al. 2017*). To find the solution inside a layer, the splitting technique is often used in which an additional boundary is

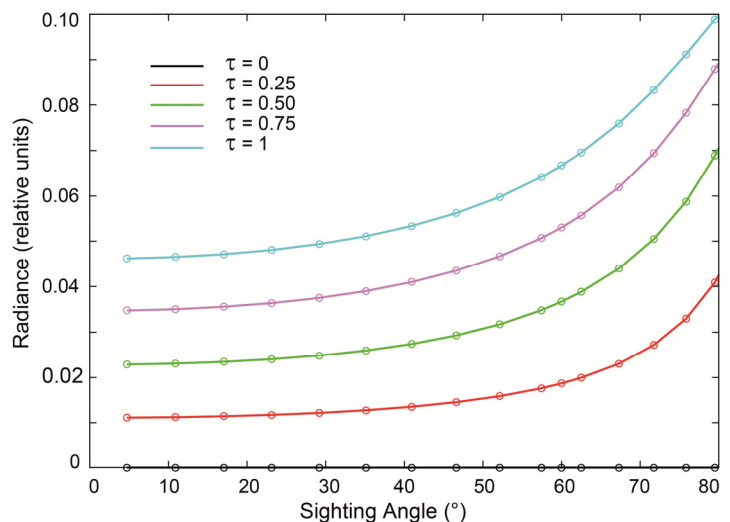


Fig. 3-28: Computations of the reflection function inside the layer of the optical thickness 1. Lines correspond to the new technique, while circles correspond to the splitting approach, in which additional boundaries are introduced inside a layer.

introduced during the layering procedure. This approach makes the solution more time-consuming, especially when the continuous dependence of the radiance from the vertical coordinate is required. In Pydome, a technique for computing the radiance inside a layer is adopted (*Budak et al. 2015*), which is based on mixing two one-point boundary value problems for upward and downward directions, respectively. The positive exponents are excluded and a computationally stable solution can be derived. The results of this method are illustrated in Fig. 3-28. This technique is fast and does not introduce performance bottlenecks in the RT solver.

### References

*Thomas, G., Stamnes, K.:* Radiative Transfer in the Atmosphere and Ocean. Cambridge University Press, 2002.

*Doicu, A., Trautmann, T.:* Discrete ordinate method with matrix exponential for a pseudo-spherical atmosphere: Scalar case. *J. Quant. Spectros. & Radiat. Transfer.* 110, 146-158, 2009.

*Efremenko, D.S., Molina Garcia, V., Gimeno Garcia, S., Doicu, A.:* A review of the matrix-exponential formalism in radiative transfer. *J. Quant. Spectros. & Radiat. Transfer,* 196, 17-45, 2017.

*Budak, V.P., Kaloshin, G.A., Shagalov, O.V., Zheltov V.:* Numerical modeling of the radiative transfer in a turbid medium using the synthetic iteration. *Optics Express* 23, A829, 2015.

## 3.15 Sound Scattering on Bispheres

*T. Rother*

Scanning the relevant literature, and in contrast to the situation in electromagnetic wave scattering, one is faced with only few data sets for sound scattering on bispheres (*Eyges 1957, Peterson and Ström 1974, Turley 2006*). The development of a Lippmann-Schwinger-like T-operator equation and its iterative solution to study sound scattering on bispheres was therefore within the focus of the past year's activities regarding the modeling of multiple scattering effects. These examinations aimed at expanding the data base for sound scattering on different bisphere configurations, to discuss some simplifications and approximations, and to study the importance of the obtained results for modeling electromagnetic wave scattering on bispheres if unpolarized measurements are performed.

In deriving the T-operator equation the separation matrix and the matrix of rotation are employed, as described by *Martin (2002)*. However, since restricting the considerations to bispheres, we can benefit from two simplifications from the very beginning. The first is, one sphere is always centered in the laboratory frame, i.e. the frame at which the scattering measurement takes place. The second utilizes the fact that the transformation into the local coordinate system of the shifted sphere is always described by one rotation and one shift along the new z-axis. However it needs to be mentioned that, in doing so, this new coordinate system does not have axes in parallel to the axes of the laboratory frame. To achieve the latter would require a second rotation that is neglected in the developed approach. The rigorous T-operator equation is iteratively solved afterwards up to the second-order iteration. A comparable iteration scheme was already proposed and used by *Peterson and Ström (1974)*. The role of the reciprocity condition to estimate the accuracy and reliability of the solutions, as it was discussed by *Schmidt et al. (2012)*, is studied for the different orders of iteration. Results are obtained for different bisphere configurations in fixed and random orientation. Neglecting the interaction between the spheres, a simple expression could be derived for the 0<sup>th</sup>-order iteration. If the distance between two identical spheres equals or is larger than the diameter of the spheres the simple expression of the 0<sup>th</sup>-order iteration provides already a solution of the scattering problem that is appropriate for certain applications. Furthermore, a few sum rules could be derived that result in further simplifications, and that provide simple tests for the correct implementation of the separation matrix and the matrix of rotation.

Figs. 3-29 and 3-30 show as an example the iterative solutions up to the second order of the differential scattering cross-sections for randomly oriented bispheres. The size parameter of the spheres with the radius  $a = 1$  mm is fixed to  $k_a = 3.0$ . The two distances are chosen such that the spheres are touching (Fig. 3-29), and that the distance equals the sphere's diameter (Fig. 3-30). Regarding Fig. 3-29 the good agreement between the assumption of the independent scattering and the second iteration is remarkable. This demonstrates that the interaction between the spheres is of more importance for that configuration since it lowers the pure interference term. The opposite effect can be seen in Fig. 3-30 for a larger distance. Now, with the exception of the forward direction, the results for all the considered orders of iteration and the result for the independent scattering are close to each other. It should be emphasized that the analytical expression derived for this zeroth-order iteration can simply be generalized to an arbitrary number of spheres.

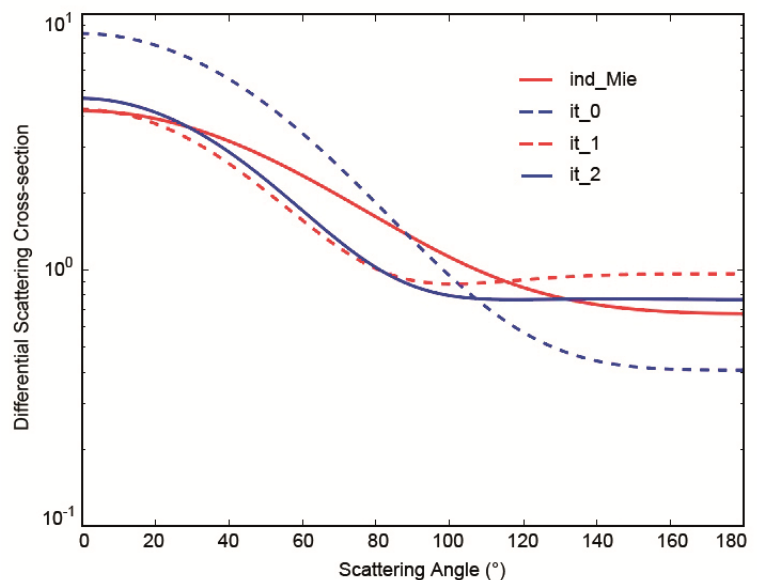


Fig. 3-29: Differential scattering cross-section for randomly oriented, sound-soft and touching bispheres. The different orders of iteration and the independent scattering result (full red line) are shown.

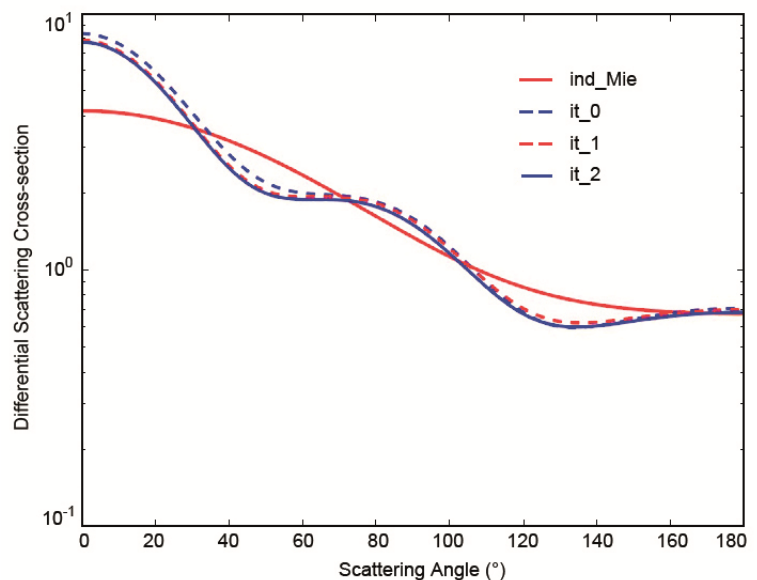


Fig. 3-30: Differential scattering cross-section for randomly oriented, sound-soft bispheres. Distance between the spheres:  $b = 6.0$  mm. The different orders of iteration and the independent scattering result (full red line) are shown.

### References

- Eyges, L.: Some Nonseparable Boundary Value Problems and the Many-Body Problem. *Annals Phys.* 2, 101, 1957.
- Peterson B. and Ström, S.: Matrix formulation of acoustic scattering from an arbitrary number of scatterers. *J. Acoust. Soc. Am.* 56, 771, 1974.
- Turley, S.: Acoustic scattering from a sphere, see: [http://volta.byu.edu/winzip/scalar\\_sphere.pdf](http://volta.byu.edu/winzip/scalar_sphere.pdf), 2006.
- Martin, P. A.: *Multiple Scattering: Interaction of Time-Harmonic Waves with Obstacles*. Cambridge Univ. Press, UK, 2002.
- Schmidt, K., Yurkin, M. and Kahnert, M.: A case study on the reciprocity in light scattering computations. *Optics Express* 20, 23253, 2012.



## 4. Atmospheric Remote Sensing – Applications

### 4.1 First Results: SO<sub>2</sub> Emissions Detected by Sentinel-5 Precursor

*P. Hedelt*

With the launch of Sentinel-5 Precursor (S5P) on October 13, 2017 a new era of atmospheric spectral measurements in the UV range began. S5P provides an unprecedented spatial resolution of  $3.5 \times 7 \text{ km}^2$  while former missions only had much lower resolutions of  $40 \times 80 \text{ km}^2$  (GOME-2) or  $13 \times 24 \text{ km}^2$  (OMI). In the timeframe from November 2017 until April 2018, S5P conducted the commissioning phase. One of its achievements was the optimization of the retrieval algorithms. However, although commissioning phase activities usually interrupted scientific measurements with the scientific algorithms still not being fully optimized, the first results emerging from processed scientific data were already exciting and promised a rich harvest in the years to come.

The sulfur dioxide (SO<sub>2</sub>) algorithm developed by BIRA-IASB and implemented in the operational system at the ground segment by DLR, uses a three window DOAS fit approach for retrieving this trace gas. Weak emissions from anthropogenic sources or degassing volcanoes are detected using the first fit window in the range from 312-326 nm. In order to avoid saturation effects for stronger SO<sub>2</sub> emissions, e.g. from volcanic eruptions with VCDs > 15 DU, the second fit window from 325-335 nm is used. Finally, for explosive volcanic eruptions with VCDs > 250 DU a fit-window in the range 360-390 nm is applied. For each fit-window a corresponding AMF LUT allows the transformation of measured SCDs to SO<sub>2</sub> VCDs.

We developed an algorithm to identify and flag enhanced SO<sub>2</sub> emissions in the S5P data. This algorithm is based on the volcanic detection algorithm developed for GOME-2 and further improved, so that even weak emission of > 0.7 DU can be recorded and attributed to potential emissions by volcanoes or known anthropogenic sources.

#### **Volcanic eruptions**

During the commissioning phase several volcanic eruptions could already be detected by S5P. Major ones comprised

- Ambae: Located in the archipelago of Vanuatu, the volcano's activity could be monitored shortly after the S5P launch once TROPOMI had started with scientific measurements. The enhanced spatial resolution of S5P permitted to study how the SO<sub>2</sub> plumes drifted over the archipelago (Fig. 4-1).
- Mount Agung: This volcano in Indonesia on the island of Bali erupted on November 27, 2017. Fig. 4-2 shows the detection of S5P on the same day together with the corresponding GOME-2 image. The difference between S5P and GOME-2 is very obvious.
- Mount Sinabung: This volcano on the island of Sumatra in Indonesia is active since 2014. A recent explosive eruption occurred on February 19, 2018 at 8:30 h local time with a strong ash and SO<sub>2</sub> plume reaching about 5-7 km altitude (see Fig. 4-3). It was followed by a strong eruption at 20:30 h local time on February 25, accompanied with an ash plume of about 3.8 km height.

#### **Anthropogenic pollution**

First results during the commissioning phase already show a very low background noise level of less than 0.5 DU. Hence, in combination with the very high spatial resolution, also weak emission sources are now clearly detectable in daily measurements. This is a considerable improvement as compared to GOME-2 where monthly averages have to be calculated in order to detect weak emission sources, e.g. from anthropogenic pollution. Fig. 4-4 shows the SO<sub>2</sub> emissions from coal-fired power plants in India. Note that India has overcome China in terms of the amount of anthropogenic pollution. Whereas in China emission control and flue-gas desulfurization devices are installed, this is not the case in India. Also in the region of the Persian Gulf (Fig. 4-5) gas-flaring activities and oil and gas refineries are clearly detectable with S5P.

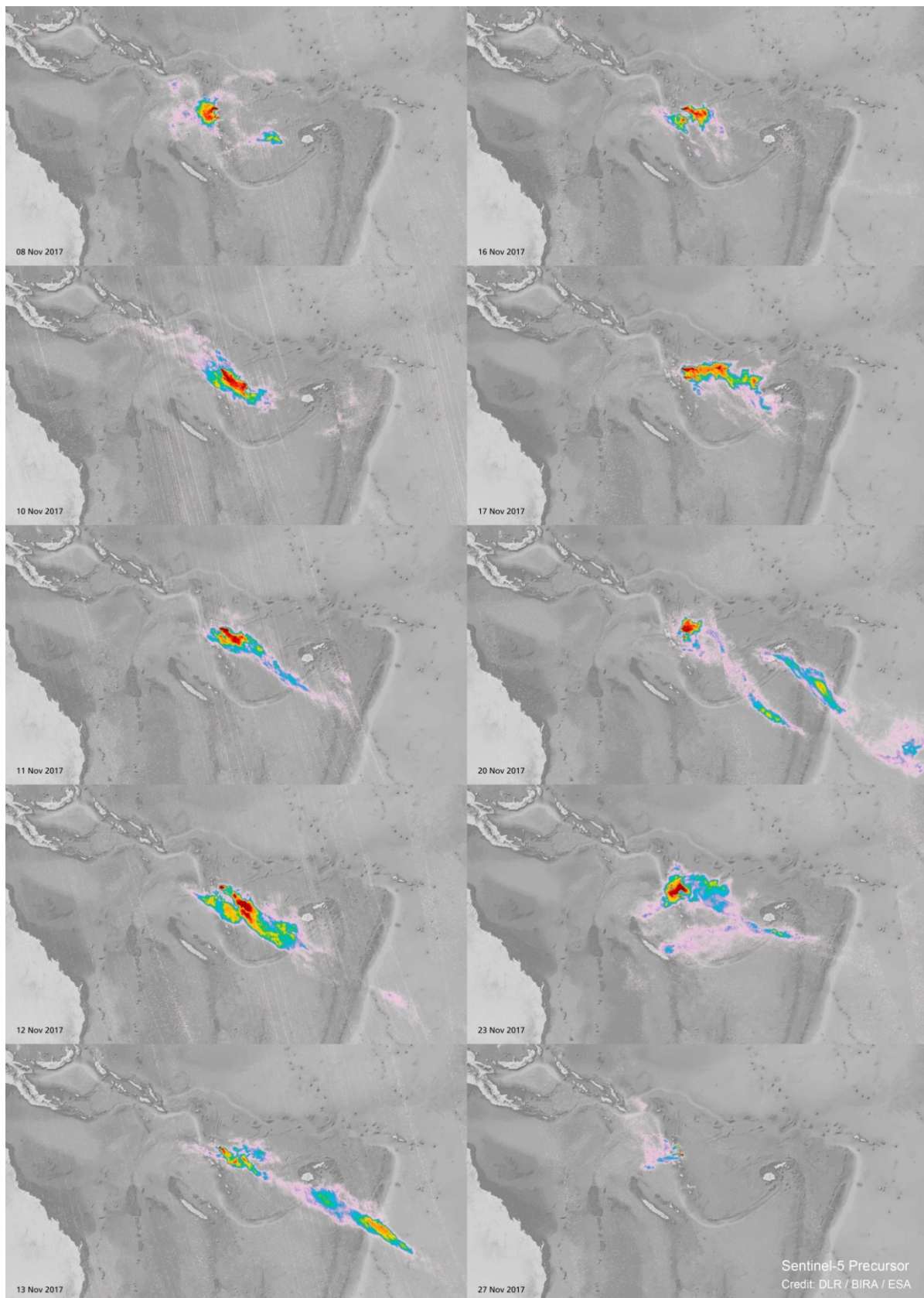


Fig. 4-1: Plumes of volcanic SO<sub>2</sub> from the Ambae eruption drift over the archipelago of Vanuatu between November 8 and 27, 2017. Because of the high spatial resolution of S5P even fine detail of the SO<sub>2</sub> clouds can be imaged.

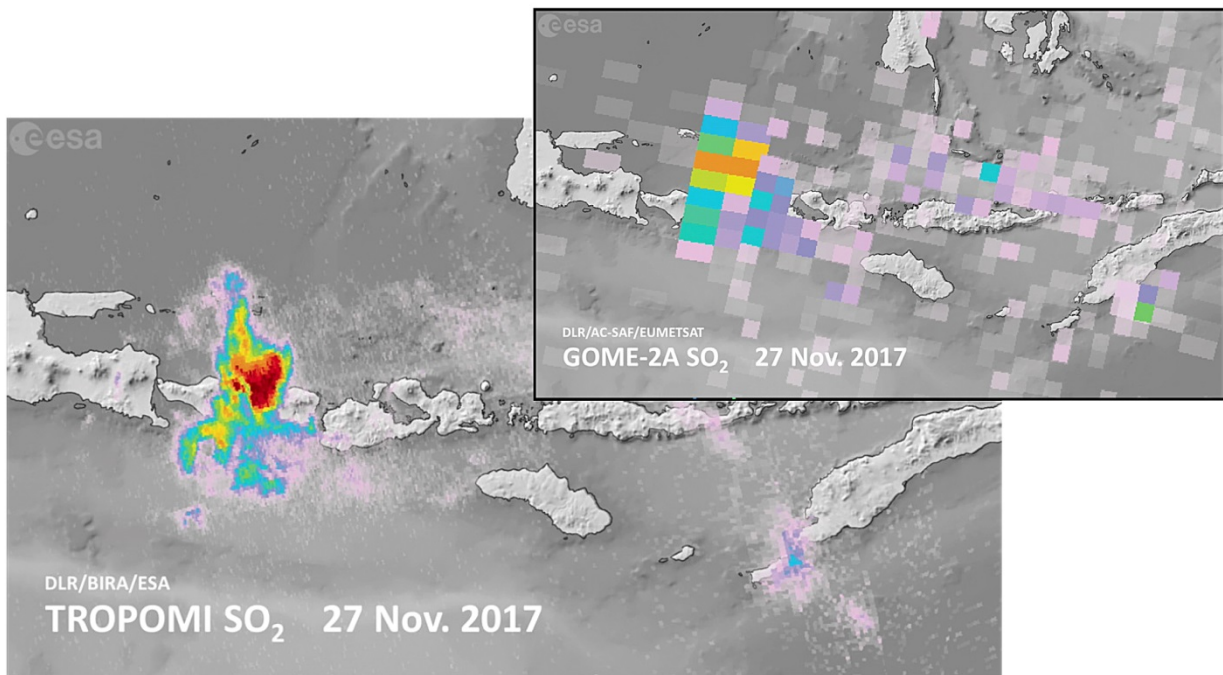


Fig. 4-2: Volcanic SO<sub>2</sub> cloud from the Mt. Agung eruption in Indonesia, measured by S5P and GOME-2 (inset). Clearly visible is the much higher spatial resolution of S5P.

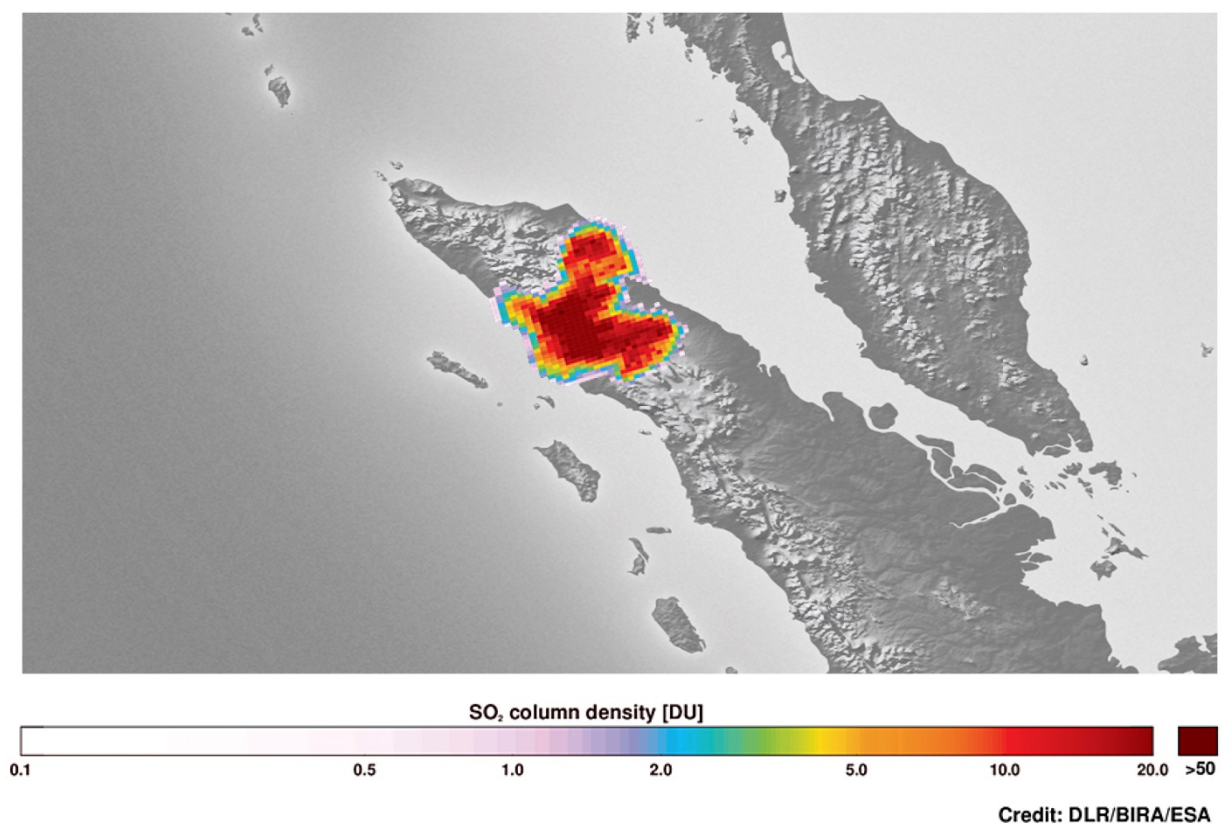


Fig. 4-3: Measurement of the volcanic SO<sub>2</sub> cloud from Mt. Sinabung on February 19, 2018, approx. 3 hours after its eruption at 8:30 h local time.

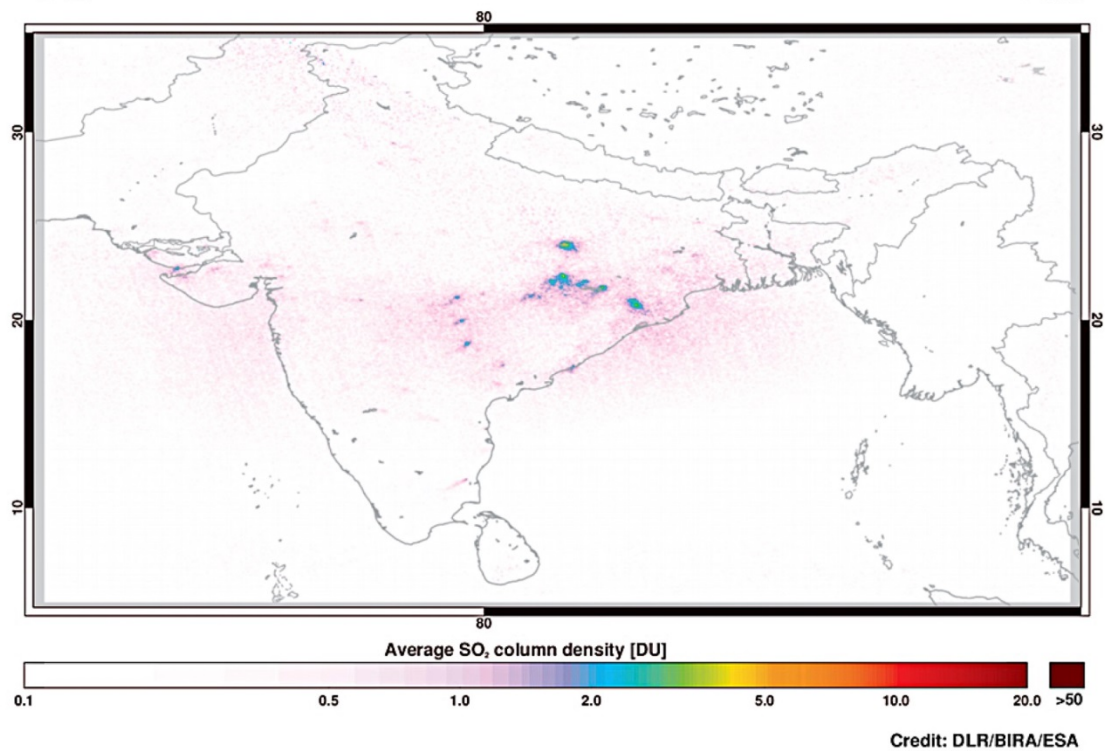


Fig. 4-4: Weak SO<sub>2</sub> emission from coal-fired power plants in India using sulfur-rich coal. The image was created by averaging daily measurements from November 8, 2017 to February 28, 2018 on a common 0.01° × 0.01° grid.

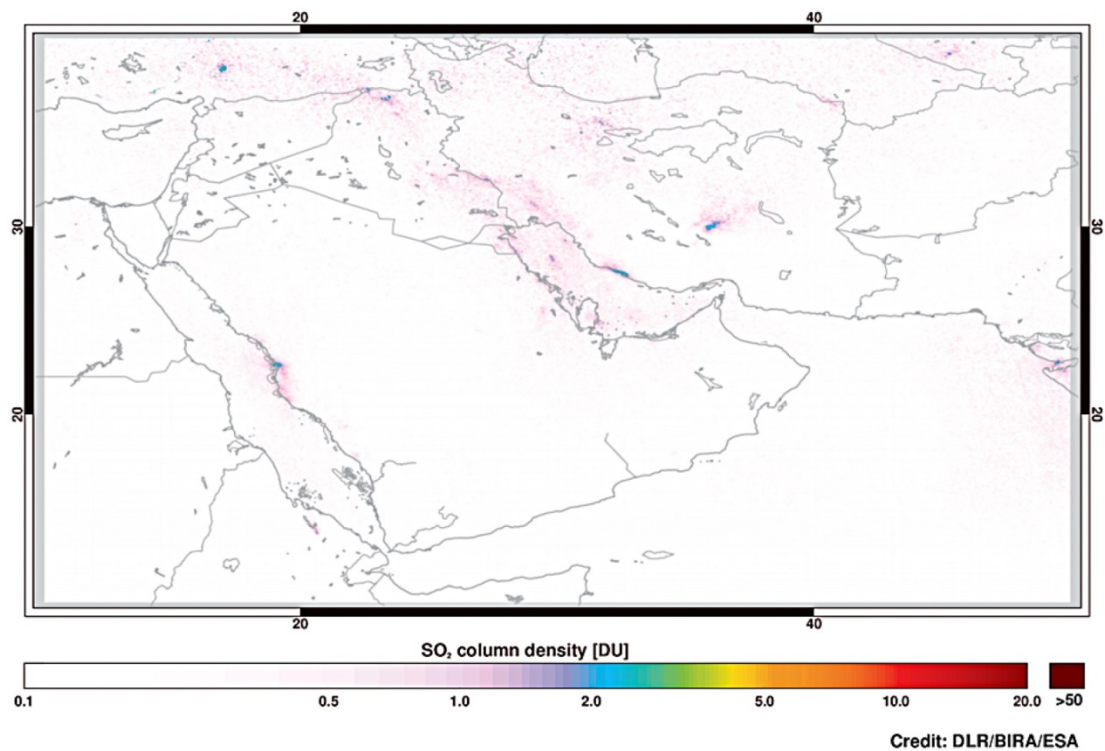


Fig. 4-5: Weak SO<sub>2</sub> emissions from offshore flaring and refineries on the Arabian peninsula and the Persian Gulf. The image was created by averaging daily measurements from November 8, 2017 to February 28, 2018 on a common 0.01° × 0.01° grid.

## 4.2 The GOME-type Total Ozone Essential Climate Variable

*M. Coldewey-Egbers, D. Loyola, K.-P. Heue*

In 2017 we continued our work related to the GOME-type Total Ozone Essential Climate Variable (GTO-ECV) data record created within the framework of the second phase of the European Space Agency's Climate Change Initiative (ESA-CCI). The existing GTO-ECV data record (*Coldewey-Egbers et al. 2015*) has been updated and extended in time. Furthermore, level 3 total ozone data products are now generated quasi-operationally as part of the Copernicus Climate Change Service (C3S). The updated trend analysis indicates that for most regions trends are still not different from zero since the expected onset of recovery is masked by the dominant inter-annual variability in ozone.

### **Update, extension, and ground-based validation of GTO-ECV v3**

Total ozone column observations from GOME (Global Ozone Monitoring Experiment), SCIAMACHY (SCanning Imaging Absorption SpectroMeter for Atmospheric CHartography), GOME-2A, GOME-2B, and OMI (Ozone Monitoring Instrument) were combined into one homogeneous time series, thereby taking advantage of the high inter-sensor consistency which has been achieved through the application of a common retrieval algorithm. GTO-ECV V3 relies on level 2 data retrieved with the direct fitting approach GODFIT V4 (*Danckaert et al. 2017*). Remaining small biases among individual instruments have been removed by using an inter-sensor calibration approach in which OMI is used as the reference standard. The extended data record spans the 22-year period from July 1995 to June 2017.

Compared to the ground-based measurement standard (Brewer, Dobson as well as UV-VIS instruments) the gridded global monthly mean total ozone columns show an excellent agreement with 0.5 to 1.5% peak-to-peak amplitude (*Garane et al. 2017*). Fig. 4-6 displays time series of the percentage difference between satellite observations and ground-based measurements in the northern hemisphere for both the Dobson and the Brewer network and indicates that the GTO-ECV level 3 data record is of the same high quality as the equivalent individual level 2 data products that constitute it. In the northern hemisphere a negligible drift with  $-0.11 \pm 0.10\%$  per decade for Dobson and  $+0.22 \pm 0.08\%$  per decade for Brewer collocations is found. Hence, it can be concluded that the exceptional quality of the temporal stability satisfies well the GCOS requirements of 1-3% per decade which makes the level 3 GTO-ECV V3 data set useful and suitable for longer term analysis of the ozone layer, such as decadal trend studies, the evaluation of model simulations, and data assimilation applications.

### **Operational production as part of the Copernicus Climate Change Service (C3S)**

In the framework of Copernicus which is the European Union's program on monitoring the Earth's environment using satellite and ground-based observations, the Copernicus Climate Change Service (C3S) is a new service providing reliable information for a better understanding of climate change and its impact. It has been implemented by the European Centre for Medium-Range Weather Forecasts (ECMWF) and aims at combining observations of the climate system with the latest science in order to develop qualitative data about the past, current and future states of climate in Europe and worldwide. Regarding ozone and following the developments made in the framework of ESA-CCI an operational ECV production system has been built which delivers a large number of ozone data records to be integrated in the C3S climate data store. For total ozone monthly mean products from five individual sensors (GOME, SCIAMACHY, OMI, GOME-2A, and GOME-2B) as well as the merged GTO-ECV are provided. Except for GOME and SCIAMACHY, all products are extended on a regular basis (quarterly for the single sensor products and semi-annually for the merged product, respectively).

### **Update on total ozone trends**

Fig. 4-7 illustrates the total ozone trend for the period 1995 to 2016 from the GTO-ECV gridded data record using a standard multiple linear least squares approach that quantifies the relationship between ozone and several explanatory variables such as the QBO, the solar cycle, or ENSO (update of *Coldewey-Egbers et al. 2014*). A linear term is used for the long-term trend. Estimated trends are positive, but still close to zero and statistically not significant for most parts of the globe. The positive trend observed in the North Atlantic region is due to the impact of the North Atlantic Oscillation which modulates total ozone through changes in tropopause pressure.

In *Weber et al. (2017)* we report on updated zonal mean total ozone trends from five different data sets for the period 1979-2016. There are two different versions of merged data sets from the series of SBUV(-2) satellite instruments and two merged data sets that are mainly based upon the series of

European space-borne spectrometers, one of which is the GTO-ECV record. The 5<sup>th</sup> data set is the monthly zonal mean from ground data collected at WOUDC (World Ozone and UV Data Center). For most data sets and regions the trends since the stratospheric halogens reached maximum are not significantly different from zero. However, for some latitudes, in particular the southern hemisphere extratropics and northern hemisphere subtropics, several data sets show small positive trends ( $\leq 1\%/decade$ ) which are barely statistically significant at the  $2\sigma$  uncertainty level. In the tropics two data sets show significant trends of  $+0.5$  to  $+0.8\%/decade$ , while the other show near zero trends. Positive trends since 2000 are observed over Antarctica in September, but near zero trends in October as well as in March over the Arctic. Since uncertainties due to possible drifts between the data sets as well as from the merging procedure used in the satellite data sets or due to the low sampling of ground data are not accounted for, the retrieved trends can only be considered being at the brink of becoming significant, but there are indications that we are about to emerge into the expected recovery phase. Nevertheless, the recent trends are still considerably masked by the observed large year-to-year variability in total ozone.

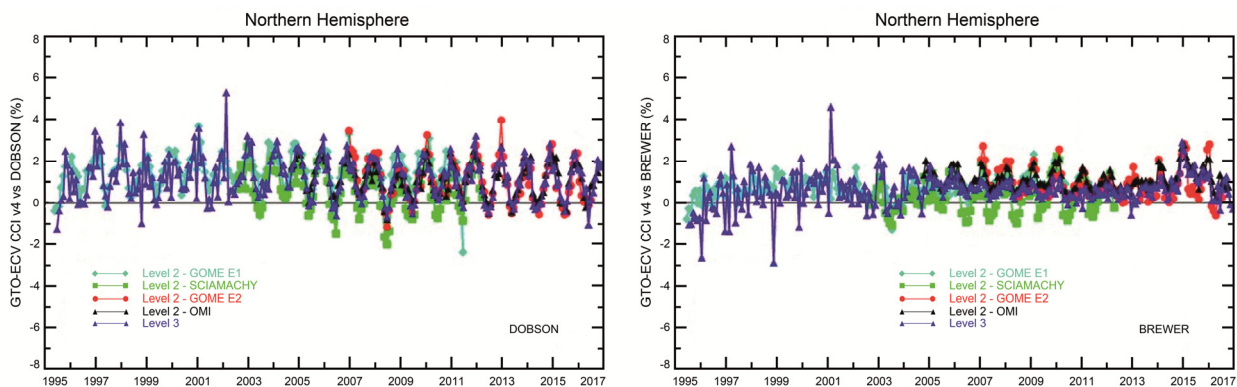


Fig. 4-6: Time series of the percentage difference between satellite observations and ground-based measurements in the Northern Hemisphere for the Dobson network (left panel) and for the Brewer network (right panel). Light blue line: GOME level-2 comparison, green line: SCIAMACHY level-2 comparison, red line: GOME-2A level-2 comparison, black line: OMI level-2 comparison, and purple line: level-3 GTO-ECV V3 comparison (adapted from *Garane et al. 2017*).

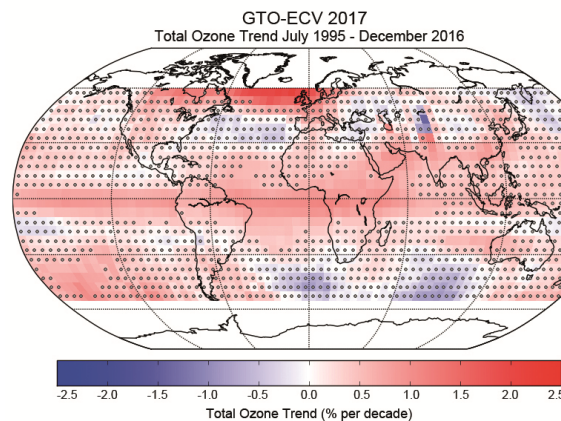


Fig. 4-7: Total ozone trend given as % per decade for the time period 1995-2016 from GTO-ECV using a multiple linear least squares approach. Dots denote that the trend is statistically not significant.

### References

Coldewey-Egbers, M., Loyola, D., Braesicke, P., Dameris, M., Van Roozendael, M., Lerot, C. and Zimmer, W.: A new health check of the ozone layer at global and regional scales. *Geophys. Res. Lett.*, 41, 4363-4372, doi:10.1002/2014GL060212, 2014.

Coldewey-Egbers, M., Loyola, D., Koukoulis, M., Balis, D., Lambert, J.-C., Verhoelst, T., Granville, J., Van Roozendael, M., Lerot, C., Spurr, R., Frith, S.M. and Zehner, C.: The GOME-type Total Ozone Essential Climate Variable (GTO-ECV) data record from the ESA Climate Change Initiative. *Atmos. Meas. Tech.*, 8, 3923-3940, doi:10.5194/amt-8-3923-2015, 2015.

Danckaert T., Lerot, C., Van Roozendael, M., Spurr, R., Romahn, F., Zimmer, W., Heue, K.-P., Coldewey-Egbers, M., and Loyola, D.: Total ozone retrievals from TROPOMI/S5p using a direct-fitting approach: Algorithm Theoretical Basis. Atmos. Meas. Tech., in preparation, 2017.

Garane, K., Lerot, C., Coldewey-Egbers, M., Verhoelst, T., Zyrichidou, I., Balis, D. S., Danckaert, T., Goutail, F., Granville, J., Hubert, D., Koukoulis, M., Keppens, A., Lambert, J.-C., Loyola, D., Pommereau, J.-P., Van Roozendael, M., and Zehner, C.: Quality assessment of the Ozone\_cci Climate Research Data Package (release 2017): 1. Ground-based validation of total ozone column data products. Atmos. Meas. Tech. Discuss., <https://doi.org/10.5194/amt-2017-378>, in review, 2017.

Weber, M., Coldewey-Egbers, M., Fioletov, V. E., Frith, S. M., Wild, J. D., Burrows, J. P., Long, C. S., and Loyola, D.: Total ozone trends from 1979 to 2016 derived from five merged observational datasets – the emergence into ozone recovery. Atmos. Chem. Phys. Discuss., <https://doi.org/10.5194/acp-2017-853>, accepted for publication, 2017.

### 4.3 The Textbook “Green’s Functions in Classical Physics”

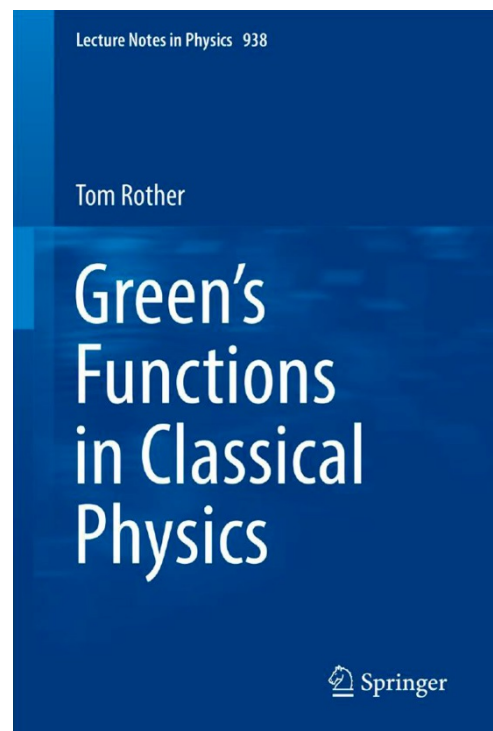
T. Rother

Based on the experience with the Green’s function formalism in electromagnetic wave scattering, this book demonstrates that such an approach can still be applied with benefit in other fields of classical physics. It was released in May 2017 by Springer in the renowned series “Lecture Notes in Physics”. Beside a detailed prologue and an outlook to quantum mechanical applications, this book contains the following chapters:

- Green’s Functions of Classical Particles
- Green’s Functions of Classical Fields
- Green’s Functions and Plane Wave Scattering
- Probability Experiments and Green’s Functions in Classical Event Spaces

The book is written as an introduction for graduate students and researchers who want to become more familiar with the Green’s function formalism not only to solve related differential equations but to understand the conceptual and epistemological importance of these functions. This latter aspect is rarely touched in classical physics. It provides an interesting and sometimes new point of view on several well-known aspects and problems in classical physics like the Kepler motion or the description of classical probability experiments in finite event spaces. Particularly this last topic is strongly related to the famous Bell’s experiment in quantum mechanics and provides an interesting new approach, and, thus, a better understanding of its epistemological consequences. The book is complemented with several exercises, and with some PYTHON code to improve its readability and usage.

T. Rother: *Green’s Functions in Classical Physics*, Lecture Notes in Physics Vol 938, Springer International Publishing, 267 pages, DOI 10.1007/978-3-319-52437-5, ISBN 978-3-319-52436-8, 2017.



#### 4.4 Exoplanet Transit Spectroscopy with the ACE-FTS Infrared Spectral Atlas of Earth

S. Städt, F. Schreier, P. Hedelt, M. Godolt (TU Berlin)

Today, 23 years after the discovery of the first extra-solar planet orbiting a main-sequence star, more than 3700 exoplanets have been detected, including a few dozen *super-Earths*, a few potentially Earth-sized planets, e.g. in the Trappist-1 system, and a few Earth-mass planets. In the last decade the characterization of these remote worlds has gained increasingly more attention. The question of the spectral appearance of terrestrial exoplanets and the possibility to identify signatures of life has been the focus of a series of modeling studies, whereas the quantitative characterization by atmospheric retrieval techniques is so far mainly confined to larger objects such as *hot Jupiters* and Neptune-sized planets.

For an assessment of atmospheric remote methods in the exoplanet domain, sensing Earth seen from outer space is an ideal test case; in fact it is the only planet that can be used for validation of exoplanet retrieval codes (to some extent, solar system planets might be used, too). However, data from space-borne missions dedicated to Earth observation have been rarely used to demonstrate the capabilities of exoplanet atmospheric studies.

The Canadian Atmospheric Chemistry Experiment – Fourier Transform Spectrometer (ACE-FTS) observes the Earth’s limb in solar occultation. Hundreds of spectra recorded in the 2004-2008 time frame have been averaged by *Hughes et al. (2014)* to compile five “infrared spectral atlases” for various seasons and latitude bands. We used the ACE-FTS infrared atlas to generate effective height spectra of Earth’s atmosphere and to compare these with model spectra generated with GARLIC, our Generic Atmospheric Radiation Line-by-line Infrared Code in order to assess the visibility and detectability of atmospheric gases in transit spectra.

For an exoplanet seen from afar it is impossible to distinguish between limb spectra corresponding to individual tangent heights. Using (primary) transit observations one essentially measures the effective height

$$h(\nu) = \int_0^{\infty} (1 - \tau(\nu, z_t)) dz_t$$

where the integral includes all limb transmission spectra  $\tau(\nu, z_t)$  with tangent altitude  $z_t$  essentially terminating at “top-of-atmosphere” (ToA). Exoplanet observations actually measure the ratio of radiation intensities that is related to the additional transit depth

$$\delta d_t(\nu) = \frac{(R_p + h(\nu))^2 - R_p^2}{R_s^2}$$

with  $R_p$  and  $R_s$  being the planetary and solar radius.

##### **Radiative transfer forward model validation and detectability study**

Our analysis has demonstrated that 10 gases substantially contribute to Earth’s transit spectrum as observed by the ACE-FTS instrument: CO<sub>2</sub>, O<sub>3</sub>, H<sub>2</sub>O, CH<sub>4</sub>, N<sub>2</sub>O, N<sub>2</sub>, HNO<sub>3</sub>, O<sub>2</sub>, and the CFCs CCl<sub>3</sub>F and CCl<sub>2</sub>F<sub>2</sub> ordered according to the relative change of the residual norm (Fig. 4-8). However, the transit spectrum modeled with these 10 “main” gases only still shows some visible discrepancies, that can be attributed to small contributions of CO, NO, NO<sub>2</sub>, OCS, CF<sub>4</sub>, ClONO<sub>2</sub>, and N<sub>2</sub>O<sub>5</sub>.

The comparison of spectra modeled with the 17 “main” gases and with 23 molecules is shown in Fig. 4-9. Although the residual is somewhat larger, the selection of the relevant molecules is especially important for the quantitative estimate of concentrations using inversion techniques. However, the importance of these gases for the modeling does not necessarily imply their detectability in noisy low resolution spectra.

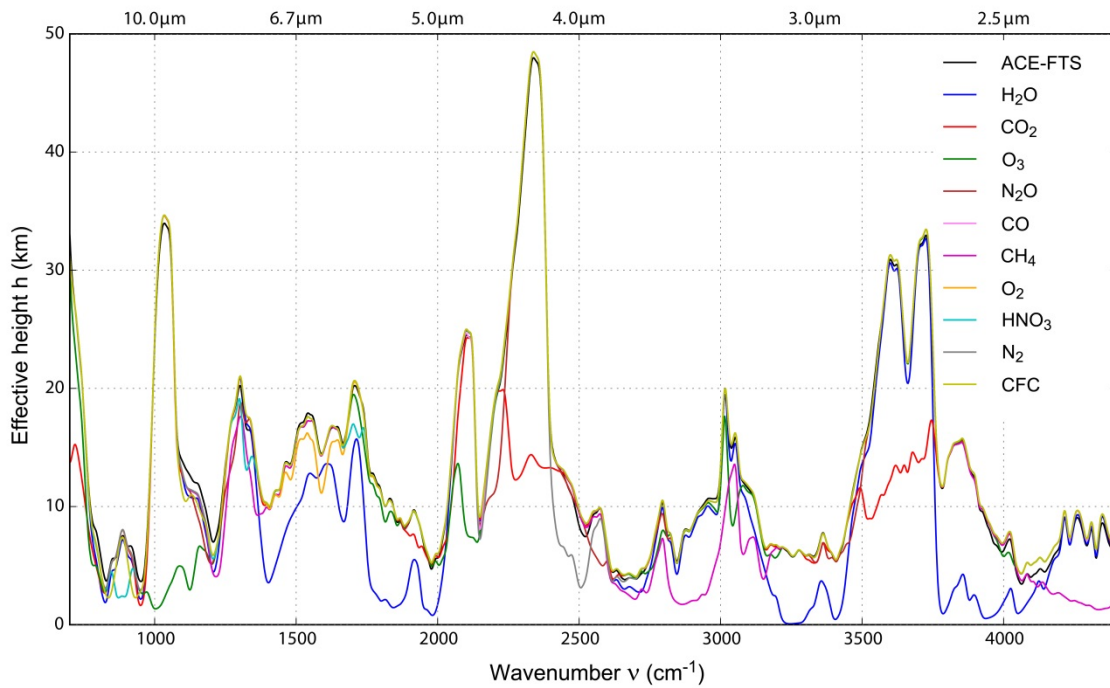


Fig. 4-8: Impact of a missing species on the global effective height spectrum (low resolution  $\Gamma = 10 \text{ cm}^{-1}$ ).

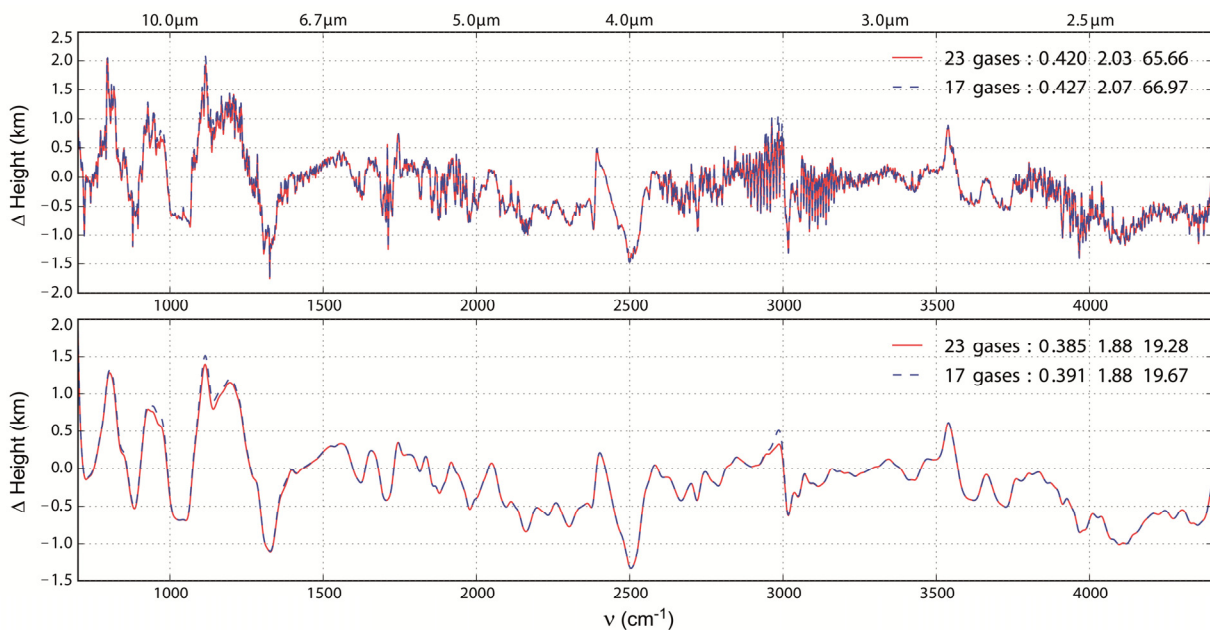


Fig. 4-9: Comparison of transit spectra residuals modeled with the 23 or with 17 gases. Moderate resolution  $\Gamma = 1 \text{ cm}^{-1}$  (top) and low resolution  $\Gamma = 10 \text{ cm}^{-1}$  (bottom). The numbers in the legend indicate the mean, maximum and norm residuum.

### ***Retrieval feasibility study***

For the quantitative estimation of atmospheric state parameters from spectroscopic observations, inversion by numerical optimization techniques is well established for Earth and solar system planets. More recently, these techniques have also been applied successfully for remote sensing of exoplanets. So far these retrievals are confined mostly to large objects such as *hot Jupiters*, whereas the analysis of smaller objects such as *super-Earths* and Earth-like exoplanets is clearly more challenging. Furthermore, retrievals of exoplanets have a difficulty in common, namely the choice of the initial guess and the lack of a priori atmospheric knowledge.

As far as we know, the method of nonlinear least squares fitting has not been applied yet to Earth-like or terrestrial exoplanets. A nonlinear least squares solver is coupled to our GARLIC forward model and

tries to minimize the residual between the synthetic “measurement” spectrum and the model spectrum for best estimate of the atmosphere with a random start concentration of the molecules. Here we use the set of AFGL atmospheres to investigate the whole range of possible results in the molecular abundances retrieval. We also do not know exactly the resolution and noise level of the data in future and therefore use different assumptions to simulate the data.

The analysis of the results showed that it is possible to retrieve the molecular abundances of an atmosphere with the right T-p profile. The residuals corresponding to the retrieved atmosphere (Fig. 4-10) with random start concentrations versus the same atmosphere are all close to zero, which is proof that the retrieval works. The lower residual for the lower resolution is caused naturally by the smaller measurement vector length. The comparison of the relative H<sub>2</sub>O VCDs shows a slightly smaller difference between the atmospheres in higher resolution (Fig. 4-11 left) than to the lower resolution (Fig. 4-11 right). Low resolution spectra are suitable for a retrieval with the right T-p profile, but have a deficit to retrieve the right profile concentration.

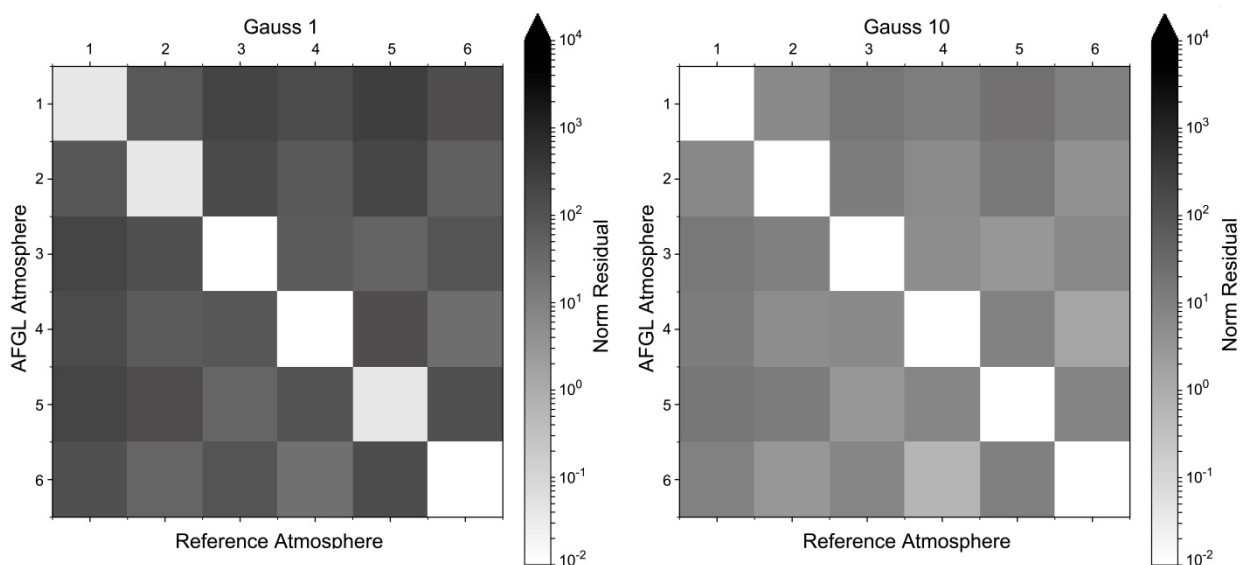


Fig. 4-10: Comparison of the norm residuals with different resolutions of the six AFGL atmospheres with  $\Gamma = 1 \text{ cm}^{-1}$  (left) and  $\Gamma = 10 \text{ cm}^{-1}$  (right). White pixel means no difference, while black means big difference.

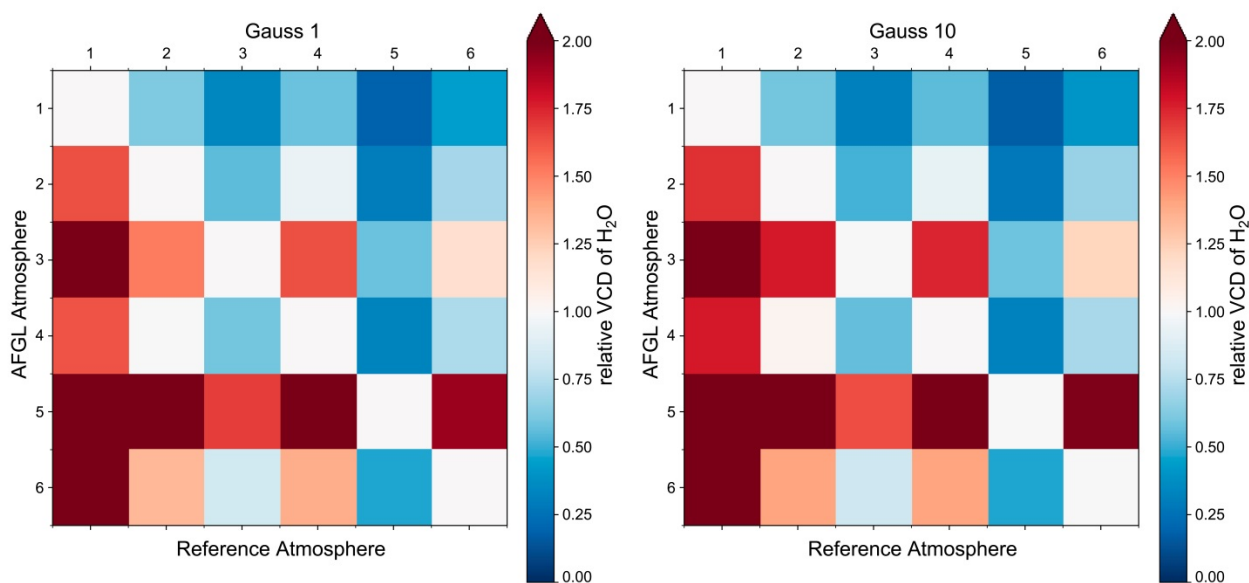


Fig. 4-11: The relative VCDs of the corresponding H<sub>2</sub>O concentrations. If the retrieved column divided by the reference column is 1, the concentrations are the same after the retrieval.

## References

Hughes, R., Bernath, P., and Boone, C.: ACE infrared spectral atlases of the Earth's atmosphere. *J. Quant. Spectros. & Radiat. Transfer*, 148, 18-21, doi: 10.1016/j.jqsrt. 2014.06.016., 2016.

Schreier, F., Städt, S., Hedelt, P., and Godolt, M.: Transmission Spectroscopy with the ACE-FTS Infrared Spectral Atlas of Earth: A Model Validation and Feasibility Study. *Molecular Astrophysics*, in press. doi: j.molap.2018.02.001, 2018.

## 4.5 Molecular-Level Computational Astrobiology at ELSI

*M. Meringer, R. Bose (NISER), M. Ilardo (UCPH), C. Butch, R. Gillams, C. Giri, H.J. Cleaves (all ELSI)*

The Earth-Life Science Institute (ELSI) of the Tokyo Institute of Technology was launched in December 2012 as part of Japan's World Premier International Research Center Initiative, a program similar to the Excellence Initiative for German Universities. ELSI's research mission is to elucidate how our planet was formed and how its early environment allowed for the rise of initial life and its subsequent evolution to complexity. By exploring both the origin and evolution of the Earth and the origins and evolution of life, scientists at ELSI are creating a new field called "Bioplanetology" and provide an interdisciplinary research hub for it.

Since its very beginnings ELSI supports our astrobiology-related in silico studies of the chemical space surrounding the molecules of life on Earth and impacts on hypothetical biologies that might have developed on other solar system bodies or elsewhere in the universe. Among the algorithmic core components of these studies are so-called "structure generators" (Meringer 2010), which allow the complete and non-redundant computational enumeration of small organic compounds with given elemental composition and optional structural constraints.

Targets of our first studies were monomeric building blocks of functional biomolecules, namely amino acids (Meringer et al. 2013, Ilardo et al. 2015) and nucleotides (Cleaves et al. 2015). The methodology of applying structure generation to problems arising from astrobiology has recently been published as a review (Meringer and Cleaves 2017a). The latest results of our research line offer new insights to the chemical structure space defined by constituents of the reverse tricarboxylic acid (rTCA) cycle (Meringer and Cleaves 2017b), representing the core of life's intermediary metabolism.

Thanks to generous funding by the John Templeton Foundation in 2015 the ELSI Origins Network (EON) was established. This framework offered positions for post-doctoral scientists as well as support for long-term visitors, and allowed us to intensify studies within our research line:

- We were able to extend our focus to another chemical compound class that is believed to have a strong impact on life's origins: Lipids are known to form micelles and bilayers that could have played an important role in early compartmentalization.
- After proving the adaptive properties of the genetically encoded amino acids (Ilardo et al. 2015), we started to investigate if such adaptive features can also be found in subsets of the encoded set, which would show pathways how the amino acid alphabet developed during early evolution.
- We started to generate virtual chemical compound libraries that describe the small molecule inventory potentially available for seeding chemical and biological evolution in diverse environments of our solar system and beyond (Cleaves et al. in preparation).

Such generally small molecule compound libraries could be used for evaluation of astrobiology experiments on future exploration missions to solar system bodies that might harbor life, e.g. the icy moons Europa and Enceladus. Mass spectrometers offer unique ways to analyze the chemical composition of samples collected on such missions. We revisited the data delivered by COSAC (Goesmann et al. 2015), a mass spectrometer on board the lander of ESA's ROSETTA mission, which arrived at comet 67P/Churyumov-Gerasimenko in 2014.

The spectra recorded by COSAC represent a mixture of compounds and a critical step in the interpretation of this data is the fit of the experimental spectrum by reference spectra of pure

compounds. We applied non-negative least squares fitting to the spectrum measured by COSAC in “sniffing mode” and reference spectra of 16 compounds as reported in (Goesmann *et al.* 2015). NNLS finds a slightly better solution than the manual fit published in (Goesmann *et al.* 2015). We calculated an RSS of 0.00206 instead of 0.00343, which reduces the unexplained part of the spectrum from 14.4% to 13.5% , using only 14 of the 16 compounds (no ethylamine and glycolaldehyd). Beyond these slight differences the fits are quite similar and confirm the results of (Goesmann *et al.* 2015, Fig. 4-12).

Forthcoming exploration missions will be equipped with instruments that cover an extended mass range and which offer higher resolution and sensitivity. Sophisticated molecular-level computational methods will become inevitable for processing data of future spectrometry-based life detection techniques.

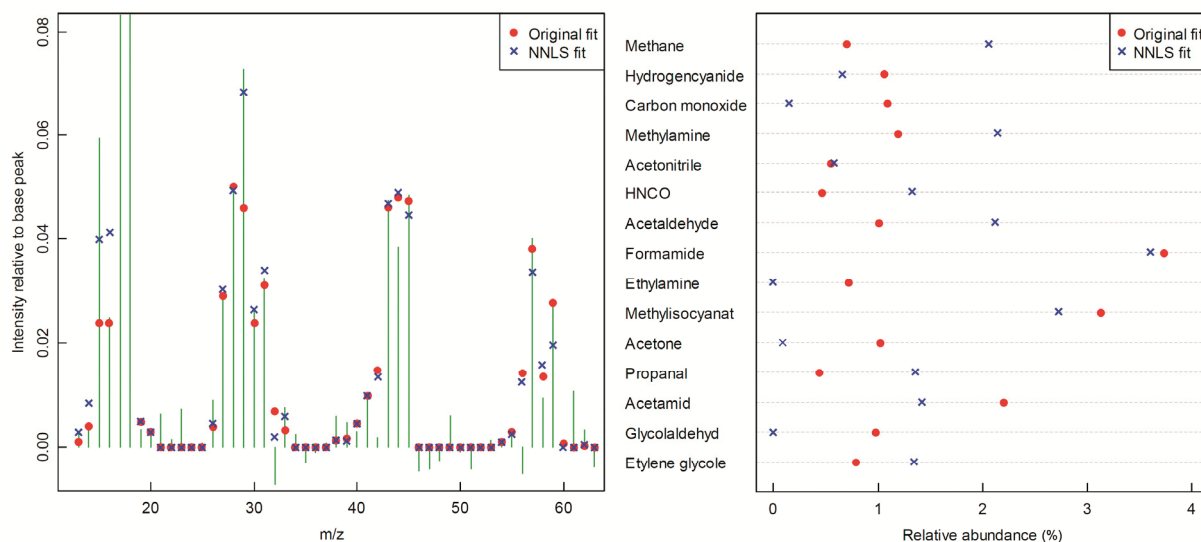


Fig. 4-12: The graphic on the left shows the COSAC spectrum together with the original fit of *Goesmann et al.* (2015) and our NNLS fit (peaks with negative intensities originate from background subtraction). On the right panel relative abundances obtained from the original fit and the NNLS fit are depicted (due to its high abundance water is excluded from the chart).

## References

Meringer, M.: Structure Enumeration and Sampling. Handbook of Chemoinformatics Algorithms. Edited by J.-L. Faulon and A. Bender, Chapman & Hall: 233-267, 2010.

Meringer, M., Cleaves, H.J., and Freeland, S.J.: Beyond Terrestrial Biology: Charting the Chemical Universe of  $\alpha$ -Amino Acid Structures. *J. Chem. Inf. Model.* 53, 2851-2862, 2013.

Ilardo, M., Meringer, M., Freeland, S.J., *et al.*: Extraordinarily Adaptive Properties of the Genetically Encoded Amino Acids. *Scientific Reports* 5 (9414), 2015.

Cleaves, H.J., Meringer, M., Goodwin, J.T.: 227 Views of RNA: Is RNA Unique in Its Chemical Isomer Space? *Astrobiology* 15, 538-558, 2015.

Meringer, M., Cleaves, H.J.: Exploring Astrobiology Using in silico Molecular Structure Generation. *Phil. Trans. R. Soc. A.* 375 (2109), 2017a.

Meringer, M., Cleaves, H.J.: Computational Exploration of the Chemical Structure Space of Possible Reverse Tricarboxylic Acid Cycle Constituents. *Scientific Reports* 7 (17540), 2017b.

Cleaves, H.J., Butch, C., Meringer, M.: The Small Organic Molecule Space of the Universe. In preparation.

Goesmann, F., Rosenbauer, H., Bredehöft, J.H., *et al.*: Organic compounds on comet 67P/Churyumov-Gerasimenko revealed by COSAC mass spectrometry. *Science* 349(6247): aab0689, 2015.

## 5. Documentation

### 5.1 Books

Rother, T.: Green's Functions in Classical Physics. Lecture Notes in Physics, 938. Springer International Publishing, 267 pages, ISBN 978-3-319-52436-8, 2017.

### 5.2 Journal Papers

Afanas'ev, V.P., Gryazev, A.S., Efremenko, D., Kaplya, P.S.: Differential inverse inelastic mean free path and differential surface excitation probability retrieval from electron energy loss spectra. *Vacuum*, 136, 146-155, DOI: 10.1016/j.vacuum.2016.10.021, 2017.

Afanas'ev, V.P., Gryazev, A.S., Efremenko, D., Kaplya, P.S., Kuznetcova, A.V.: Extracting the differential inverse inelastic mean free path and differential surface excitation probability of Tungsten from X-ray photoelectron spectra and electron energy loss spectra. *Journal of Physics: Conference Series*, 941(1), 1-6. DOI: 10.1088/1742-6596/941/1/012019, 2017.

Bougiatioti, A., Argyrouli, A., Solomos, S., Vratolis, S., Eleftheriadis, K., Papayannis, A. and Nenes, A.: CCN activity, variability and influence on droplet formation during the HygrA-CD campaign in Athens, *Atmosphere*, 8(6), 108, DOI: 10.3390/atmos8060108, 2017.

Bramstedt, K., Stone, T. C., Gottwald, M., Noel, S., Bovensmann, H., Burrows, J.P.: Improved pointing information for SCIAMACHY from in-flight measurements of the viewing directions towards sun and moon. *Atmos. Meas. Tech.*, 10, 2413-2423, DOI: 10.5194/amt-10-2413-2017, 2017.

Buchwitz, M., Reuter, M., Schneising, O., Hewson, W., Detmers, R.G., Boesch, H., Hasekamp, O., Aben, I., Bovensmann, H., Burrows, J.P., Butz, A., Chevallier, F., Dils, B., Frankenberg, C., Heymann, J., Lichtenberg, G., De Maiziere, M., Notholt, J., Parker, R., Warneke, T., Zehner, C., Griffith, D.W.T., Deutscher, N.M., Kuze, A., Suto, H., Wunch, D.: Global satellite observations of column-averaged carbon dioxide and methane: The GHG-CCI XCO<sub>2</sub> and XCH<sub>4</sub> CRDP3 data set. *Remote Sensing of Environment*, 203, 276-295, DOI: 10.1016/j.rse.2016.12.027, 2017.

Efremenko, D., Molina García, V., Gimeno García, S., Doicu, A.: A review of the matrix-exponential formalism in radiative transfer. *J. Quant. Spectros. & Radiat. Transfer*, 196, 17-45, DOI: 10.1016/j.jqsrt.2017.02.015, 2017.

Efremenko, D., Loyola, D., Hedelt, P., Spurr, R.: Volcanic SO<sub>2</sub> plume height retrieval from UV sensors using a full-physics inverse learning machine algorithm. *International Journal of Remote Sensing*, 38 (50), 1-27, DOI: 10.1080/01431161.2017.1348644, 2017.

Garane, K., Lerot, C., Coldewey-Egbers, M., Verhoelst, T., Zyrichidou, I., Balis, D. S., Danckaert, T., Goutail, F., Granville, J., Hubert, D., Koukouli, M., Keppens, A., Lambert, J.-C., Loyola, D., Pommereau, J.-P., Van Roozendaal, M., and Zehner, C.: Quality assessment of the Ozone\_cci Climate Research Data Package (release 2017): 1. Ground-based validation of total ozone column data products. *Atmos. Meas. Tech. Discuss.*, <https://doi.org/10.5194/amt-2017-378>, in review, 2017.

Gottwald, M., Fritz, T., Breit, H., Schättler, B., Harris, A.W.: Remote sensing of terrestrial impact craters: The TanDEM-X digital elevation model. *Meteoritics & Planetary Science* 52(7), 1412-1427, DOI: 10.1111/maps.12794, 2017.

Meringer, M., Cleaves, H.J.: Computational exploration of the chemical structure space of possible reverse tricarboxylic acid cycle constituents. *Scientific Reports*, 7, 1-11, DOI: 10.1038/s41598-017-17345-7, 2017.

Meringer, M., Cleaves, H.J.: Exploring astrobiology using in silico molecular structure generation. *Philosophical Transactions of the Royal Society A*, 375 (2109), 1-12. DOI: 10.1098/rsta.2016.0344

- Papayannis, A., Argyrouli, A., Bougiatioti, A., Remoundaki, E., Vratolis, S., Nenes, A., Solomos, S., Komppula, M., Giannakaki, E., Kalogiros, J., Banks, R., Eleftheriadis, K., Mantas, E., Diapouli, E., Tzani, C., Kazadzis, S., Biniotoglou, I., Labzovskii, L., Hey, V.J. and Zerefos, C.S.: An overview from hygroscopic aerosols to cloud droplets: The Hygra-CD campaign in the Athens basin, *Science of the Total Environment*, 574, 216-233, 2017.
- Qin, K., Wang, L., Wu, L., Xu, J., Rao, L., Letu, H., Shi, T., Wang, R.: A campaign for investigating aerosol optical properties during winter hazes over Shijiazhuang, China. *Atmospheric Research*, 198, 113-122, DOI: 10.1016/j.atmosres.2017.08.018, 2017.
- Qin, K., Rao L., Xu, J., Bai, Y., Zou, J., Hao, N., Li, S., Yu, C.: Estimating ground level NO<sub>2</sub> concentrations over central-eastern China using a satellite-based geographically and temporally weighted regression model. *Remote Sensing*, 9, 1-20, DOI: 10.3390/rs9090950, 2017.
- Schreier, F.: Computational Aspects of Speed-Dependent Voigt Profiles. *J. Quant. Spectros. & Radiat. Transfer*, 187, 44-53, DOI: 10.1016/j.jqsrt.2016.08.009, 2017.
- Schreier, F.: An assessment of some closed-form expressions for the Voigt function: II. Utilizing rational approximations for the Gauss function. *J. Quant. Spectros. & Radiat. Transfer*, 202, 81-89, DOI: 10.1016/j.jqsrt.2017.05.035, 2017.
- Theys, Nicolas, De Smedt, I., Yu, H., Danckaert, T., van Gent, J., Hörmann, C., Wagner, T., Hedelt, P., Bauer, H., Romahn, F., Pedernana, M., Loyola, D., Van Roozendael, M.: Sulfur dioxide retrievals from TROPOMI onboard Sentinel-5 Precursor: algorithm theoretical basis. *Atmospheric Measurement Techniques (AMT)*, 10, 119-153. DOI: 10.5194/amt-10-119-2017, 2017.
- Weber, M., Steinbrecht, W., Frith, S., Tweedy, O., Coldewey-Egbers, M., Davis, S., Degenstein, D., Fioletov, V.E., Froidevaux, L., de Laat, J., Long, C., Loyola, D., Roth, C., Wild, J.: Stratospheric Ozone. In: *State of the Climate in 2016, Special Supplement to Bull. Am. Meteorol. Soc.*, 98 (8), 49-51, 2017.
- Weber, M., Coldewey-Egbers, M., Fioletov, V.E., Frith, S.M., Wild, J.D., Burrows, J.P., Long, C.S., and Loyola, D.: Total ozone trends from 1979 to 2016 derived from five merged observational datasets – the emergence into ozone recovery. *Atmos. Chem. Phys. Discuss.*, <https://doi.org/10.5194/acp-2017-853>, in review, 2017.
- Xu, J., Schüssler, O., Loyola, D., Romahn, F., Doicu, A.: A novel ozone profile shape retrieval using full-physics inverse learning machine (FP-ILM). *IEEE Journal of Selected Topics in Applied Earth Observations and Remote Sensing*, 10(12), 5442-5457, DOI: 10.1109/JSTARS.2017.2740168, 2017.

### 5.3 Conference Presentations

- Afanas'ev, V.P., Gryazev, A.S., Efremenko, D., Kaplya, P.S., Kuznecova, A.V.: X-ray photoelectron spectra of Wolfram, determination of differential inelastic scattering cross-sections in Wolfram. In: *Plasma Surface interactions: Proceedings of XX Conference: Plasma Surface Interaction, Moscow, Russia, 2017*.
- Coldewey-Egbers, M., Loyola, D., Heue, K.-P., Dameris, M., Braesicke, P., van Roozendael, M., Lerot, C., Koukouli, M., and Balis, D.: The ESA-CCI total ozone and tropical tropospheric ozone climate data records: long-term trends and model evaluation. *Seminar über ausgewählte Themen der Meteorologie, Institut für Meteorologie, Klimaforschung, Karlsruher Institut für Technologie, 2017*.
- Dameris, M., Jöckel, P., Brinkop, S., Cai, D., Dietmüller, S., Coldewey-Egbers, M., Eichinger, R., Garny, H., Graf, P., Nützel, M. and Pfeiffer, A.: Short- and long-term fluctuations of stratospheric water vapor and ozone in CCMI simulations of EMAC. *CCMI Science Workshop, Toulouse, France, 2017*.
- Efremenko, D., Loyola, D., Hedelt, P.: Inverse learning machines: concepts and examples of usage for SO<sub>2</sub> plume height retrieval. *EUMETSAT 2017 – Meteorological Satellite Conference, Rome, Italy,*

2017.

- Hamidouche, M., Lichtenberg, G., Gottwald, M.: SCIAMACHY Spectral Response Function: Retrieval and Analysis. In: Geophysical Research Abstracts. EGU General Assembly, Vienna, Austria, 2017.
- Hamidouche, M., Lichtenberg, G., Aberle, B., Trautmann, T. (2017) The new MERLIN mission for atmospheric methane: Quality and performance monitoring. EUMETSAT 2017 – Meteorological Satellite Conference, Rome, Italy.
- Hamidouche, M.: SOFIA and Infrared Astronomy. Infrarottechnik - Grundlagen, Trends, moderne Anwendungen, Carl-Cranz-Gesellschaft, Wessling, Germany.
- P. Hedelt, P. Valks, D. Loyola: 10 years of GOME-2 SO<sub>2</sub> data: Volcanic eruptions and anthropogenic emissions. EUMETSAT 2017 – Meteorological Satellite Conference, Rome, Italy, 2017. .
- Hochstaffl, P., Schreier, F., Gimeno-Garcia, S., Lichtenberg, G.: CO Total Column Retrieval from SCIAMACHY: Full-Mission Validation with NDACC and TCCON. 13th International Workshop on Greenhouse Gas Measurements from Space, Helsinki, Finland, 2017.
- Lerot, C., Danckaert, T., van Gent, J., Coldewey-Egbers, M., Loyola, D., Errera, Q, Spurr, R., Garane, K., Koukoulis, M., Balis, D., Verhoelst, T., Granville, J., Lambert, J.-C. and Van Roozendaal, M.: Operational Production of the Total Ozone Essential Climate Variable as Part of the Copernicus Climate Change Service (C3S). AGU Fall Meeting, New Orleans, USA, 2017.
- Lichtenberg, G., Hamidouche, M., Schreier, F., Hochstaffl, P., Meringer, M.: SCIAMACHY: Spectral Calibration in the SWIR Channels. 13th International Workshop on Greenhouse Gas Measurements from Space, Helsinki, Finland, 2017.
- Liu, S., Valks, P., Pinardi, G., De Smedt, I., Yu, H., Beirle, S.: An improved retrieval of NO<sub>2</sub> column for GOME-2 instrument. DOAS workshop 2017, Yokohama, Japan, 2017.
- Liu, S., Valks, P., Pinardi, G., De Smedt, I., Yu, H., Beirle, S. (2017) Improved retrieval of total and tropospheric NO<sub>2</sub> column for GOME-2. EGU General Assembly, Vienna, Austria, 2017.
- Liu, S., Valks, P., Pinardi, G., De Smedt, I., Yu, H., Beirle, S.: An improved total and tropospheric NO<sub>2</sub> column retrieval for GOME-2. DPG-Frühjahrstagung, Bremen, Germany, 2017.
- Lutz, R., Loyola, D., Efremenko, D., Romahn, F.: Operational cloud products from GOME-2 and perspectives for Sentinel-5P and Sentinel-4. EUMETSAT 2017 – Meteorological Satellite Conference, Rome, Italy, 2017.
- Lutz, R., Loyola, D., Efremenko, D., Romahn, F.: Operational cloud products from Sentinel-5P and Sentinel-4. EGU General Assembly, Vienna, Austria, 2017.
- Meringer, M.: Generation of Molecular Graphs and Applications in Astrobiology. EON Workshop on Computational Chemistry: From Components to Systems and Back, Tokyo, Japan, 2017.
- Meringer, M.: Computational Approaches towards Life Detection by Mass Spectrometry. International Workshop on Life Detection Technology: For Mars, Enceladus and Beyond, Tokyo, Japan, 2017.
- Meringer, M., Butch, Christopher J., Burger, P.B., Goodwin, J.T., Cleaves, H.J.: Computational Exploration of the Chemical Space of Nucleic Acid-Like Compounds. 18th International Conference on the Origin of Life, San Diego, CA, United States, 2017.
- Molina García, V., Sasi, S., Efremenko, D., Doicu, A., Loyola, D.: Fast radiative transfer models for retrieval of cloud properties in the back-scattering region: application to DSCOVR-EPIC sensor. EGU General Assembly, Vienna, Austria, 2017.
- Montes Rubio, R., Hao, N., Liu, S., Valks, P., Trautmann, T.: Improvement of GOME-2 retrieval on the study of tropospheric air pollutants over China. AOGS 2017, Singapore, 2017.
- Reitebuch, O., Dabas, A., Marksteiner, U., Rompel, M., Meringer, M., Schmidt, K., Huber, D., Nikolaus, I., Marshall, J., de Bruin, F., Kanitz, T., Straume-Lindner, A.-G.: Aeolus Level 1 data processing and instrument calibration. In: ADM-Aeolus CAL/VAL Rehearsal Workshop - Book of Abstracts. ADM-Aeolus CAL/VAL Rehearsal Workshop, Toulouse, France, 2017.

- Reitebuch, O., Freudenthaler, V., Lehmann, V., Nikolaus, I., Potthast, R., Schmidt, K., Wandinger, U., Weissmann, M.: Experimental Validation of ADM-Aeolus with the ALADIN Airborne Demonstrator (EVA4D). ADM-Aeolus Cal/Val Rehearsal Workshop, Toulouse, France, 2017.
- Reitebuch, O., Marksteiner, U., Rempel, M., Meringer, M., Schmidt, K., Huber, D., Nikolaus, I., Dabas, A., Marshall, J., de Bruin, F., Kanitz, T., Straume, A.-G.: Aeolus End-to-End Simulator and Wind Retrieval Algorithms up to Level 1B. 28th Int. Laser Radar Conference ILRC, Bucharest, Romania, 2017.
- Schreier, F.: Py4CA<sub>T</sub>S - PYthon for Computational ATmospheric Spectroscopy. ARTS Workshop, Kristineberg, Schweden, 2017.
- Schreier, F.: Atmosphärische IR-Fernerkundung – Strahlungstransport und Inversion, Carl-Cranz-Gesellschaft, Wessling, Germany.
- Städt, S., Schreier, F., Godolt, M.: Atmospheric Composition Retrieval from Transit Spectra of Terrestrial Exoplanets: A Feasibility Study using Earth Observations. 2nd Annual Workshop of the Deutsche Astrobiologische Gesellschaft, Potsdam, Germany, 2017.
- Städt, S., Schreier, F.: Analysis of Earth spectra using the radiative transfer code GARLIC. 2<sup>nd</sup> Advanced School on Exoplanetary Science, Vietri sul Mare, Italy, 2017.
- Xu, J., Loyola, D., Romahn, F., Doicu, A.: Predicting ozone profile shape from satellite UV spectra. In: Geophysical Research Abstracts. EGU 2017, Vienna, Austria, 2017.
- Zhang, J., Xu, J., Kenntner, M., Schreier, F., Doicu, A.: Estimating atmospheric temperature profile by an airborne microwave radiometer. In: Geophysical Research Abstracts. EGU General Assembly 2017, Vienna, Austria, 2017.

#### **5.4 Attended Conferences**

- 1<sup>st</sup> SPARC LOTUS Workshop, Paris, France, March 13-15, 2017.
- DPG-Frühjahrstagung 2017, Bremen, Germany, March 13-17, 2017.
- European Geosciences Union General Assembly 2017, Vienna, Austria, April 23-28, 2017.
- First International ALTIUS Symposium, Brussels, Belgium, May 2-3, 2017.
- 2<sup>nd</sup> Advanced School on Exoplanetary Science, Vietri sul Mare, Italy, May 22-26, 2017.
- 13<sup>th</sup> International Workshop on Greenhouse Gas Measurements from Space (IWGGMS), Helsinki, Finland, June 6-8, 2017.
- 28<sup>th</sup> International Laser Radar Conference (ILRC), Bucharest, Romania, June 25-30, 2017.
- Asia Oceania Geosciences Society (AOGS) 2017, Singapore, August 6-11, 2017.
- 8<sup>th</sup> International DOAS workshop 2017, Yokohama, Japan, September 4-6, 2017.
- Open ARTS Community Workshop 2017, Kristineberg, Schweden, September 6-8, 2017.
- 3<sup>rd</sup> Convective and Volcanic Clouds (CVC) training school, Nicolosi, Italy, September 28 – October 6, 2017.
- EUMETSAT 2017 - Meteorological Satellite Conference, Rome, Italy, October 2-6, 2017.
- Workshop on Life Detection Technology: For Mars, Enceladus and Beyond, Tokyo, Japan, October 5-6, 2017.
- EON Workshop on Computational Chemistry: From Components to Systems and Back, Tokyo, Japan, October 10-13, 2017.

2<sup>nd</sup> Annual Workshop of the Deutsche Astrobiologische Gesellschaft, Potsdam, Germany, November 8-10, 2017.

AGU Fall Meeting, San Francisco, CA, United States, December 12-16, 2016.

## 5.5 Academic Degrees

### **Master Thesis**

Montes Rubio, R.: Improvement on GOME-2 Satellite Retrieval on the Study of Tropospheric Air Pollutants over China. Master thesis, completed in February 2017, Universitat Politècnica de València, Spain. (Supervisors: Dr. Nan Hao and Dr. Sergio Hoyas Calvo, Universitat Politècnica de València)

Xu, H.: Impact of molecular absorption spectroscopy data on methane retrieval from SCIAMACHY and GOSAT shortwave infrared spectra. Master thesis, completed in July 2017, Department of Electrical and Computer Engineering, Technical University of Munich. (Supervisors: Dr. F. Schreier and Prof. Dr.-Ing. J. Chen, Technical University of Munich)

Zhang, J.: Estimation of Atmospheric Temperature Using Airborne Microwave Remote Sensing. Master thesis, completed in January 2017, Faculty of Civil, Geo and Environmental Engineering, Technical University of Munich. (Supervisors: Dr.-Ing. J. Xu and PD Dr. A. Doicu)

### **Dissertation**

Hochstaffl, P.: Trace gas concentration retrieval from near infrared nadir sounding spaceborne spectrometers. Dissertation, Faculty of Physics, Ludwig-Maximilians-Universität Munich. (Supervisors: Dr. F. Schreier and Prof. Dr. A. Butz, Ludwig-Maximilians-Universität Munich)

Liu, S.: Improvement of total and tropospheric NO<sub>2</sub> column retrieval for GOME-2. Dissertation, Faculty of Civil, Geo and Environmental Engineering, Technical University of Munich. (Supervisors: Dr. P. Valks and PD Dr. A. Doicu)

Molina García, V.: Satellite measurements of cloud properties. Dissertation, Faculty of Civil, Geo and Environmental Engineering, Technical University of Munich. (Supervisor: PD Dr. A. Doicu)

Sasi, S.: Derivation of aerosols and surface properties from UV satellite measurements. Dissertation, Faculty of Civil, Geo and Environmental Engineering, Technical University of Munich. (Supervisor: PD Dr. A. Doicu)

Städt, S.: Retrieval of atmospheric parameters of terrestrial extrasolar planets around cool host stars. Dissertation, Technical University of Berlin. (Supervisors: Dr. F. Schreier, Prof. H. Rauer, Technical University of Berlin)

Wang, Z.: MAX-DOAS observations of trace gases and aerosol from the Environmental Research Station Schneefernerhaus. Dissertation. Faculty of Civil, Geo and Environmental Engineering, Technical University of Munich. (Supervisors: Dr. K.-P. Heue and PD Dr. A. Doicu)

### **Habilitation**

Efremenko, D.: Technology of fast interpretation of optoelectronic systems' signals for determining the atmospheric parameters and solid-state samples parameters. Habilitation, completed in October 2017, Moscow Power Engineering Institute.



## Annex: Abbreviations and Acronyms

AC2020	Atmospheric Composition 2020
ACE-FTS	Atmospheric Chemistry Experiment Fourier Transform Spectrometer
AD-TN	Algorithm Design Technical Note
AFGL	Air Force Geophysics Laboratory
AIRS	Atmospheric Infrared Sounder
ALADIN	Atmospheric Laser Doppler Instrument
ALH	Aerosol Layer Height
AMF	Air Mass Factor
AMSOS	Airborne Microwave Stratospheric Observing System
AMSU-B	Advance Microwave Sounding Unit-B
AOD	Aerosol Optical Depth
ARTS	Atmospheric Radiative Transfer Simulator
ATP	Atmosphärenprozessoren
ATPP	Acceptance Test Plan & Procedures
ATR	Acceptance Test Report
BASCOE	Belgian Assimilation System for Chemical Observations
bePRO	profiling tool developed by BIRA-IASB
BIRA-IASB	Belgisch Instituut voor Ruimte-Aëronomie / Institut d'Aéronomie Spatiale de Belgique
BIRRA	Beer Infrared Retrieval Algorithm
BRF	Bidirectional Reflectance Factor
BU	Binary Unit
C3S	Copernicus Climate Change Service
CAL	Clouds As Layers
CAMS	Copernicus Atmospheric Monitoring Service
CCD	Charged Coupled Device
CCI	Climate Change Initiative
CDOP	Continuous Development and Operations Phase
CF	Cloud Fraction
CKD	CloughKneizysDavies
COSAC	Cometary Sampling and Composition Experiment
COT	Cloud Optical Thickness
CPU	Central Processing Unit
CTH	Cloud Top Height
CUMT	China University of Mining and Technology
CV	Cross Validation
D	Germany
DFD	Deutsches Fernerkundungsdatenzentrum
DISORT	Discrete Ordinate Method Radiative Transfer
DLR	Deutsches Zentrum für Luft- und Raumfahrt
DOAS	Differential Optical Absorption Spectroscopy
DOME	Discrete Ordinate with Matrix Exponential
DSCD	Differential Slant Column Density
DSCOVR	Deep Space Climate Observatory
DU	Dobson Unit
E2S	End-to-End Simulator
ECMWF	European Centre for Medium-Range Weather Forecasts
ECV	Essential Climate Variable
ELSI	Earth-Life Science Institute
ENSO	El Niño Southern Oscillation
ENVISAT	Environmental Satellite
EOC	Earth Observation Center
EON	ELSI Origins Network
EPIC	Earth Polychromatic Imaging Camera
EPS	EUMETSAT Polar System

ESA	European Space Agency
ESL	Expert Support Laboratory
ESRIN	European Space Research Institute
ESTEC	European Space Research and Technology Center
EUMETSAT	European Organisation for the Exploitation of Meteorological Satellites
FADOME	Forward-Adjoint approach using Discrete Ordinate Method with Matrix Exponential
FP-ILM	Full-Physics Inverse Learning Machine
FTIR	Fourier-Transform Infrared
GARLIC	Generic Atmospheric Radiation Line-by-Line Infrared Code
GCA	Geographic Coverage Area
GCOS	Global Climate Observing System
GDP	GOME Data Processor
GEISA	Gestion et Etude des Informations Spectroscopiques Atmosphériques
GLORIA	Gimballed Limb Observer for Radiance Imaging of the Atmosphere
GODFIT	GOME Direct-Fitting
GOME	Global Ozone Monitoring Experiment
GOSAT	Greenhouse Gases Observing Satellite
GTO	GOME-type Total Ozone
GTWR	Geographical and Temporal Weighted Regression
GUI	Graphical User Interface
GWR	Geographical Weighted Regression
HAP	High Altitude Platform
HIRS	High Resolution Infrared Radiation Sounder
HITRAN	High-resolution Transmission
HLOS	Horizontal Line-of-Sight
IASI	Infrared Atmospheric Sounding Interferometer
ID	Identifier
IMAGES	Intermediate Model of Global Evolution of Species
IMF	Institut für Methodik der Fernerkundung
IPA	Institut für Physik der Atmosphäre
IUP-IFE	Institut für Umweltphysik / Institut für Fernerkundung
KNMI	Koninklijk Nederlands Meteorologisch Instituut
KOPRA	Karlsruhe Optimized and Precise Radiative Transfer Algorithm
L0	Level 0
L1	Level 1
L1b	Level 1b
L1bP	Level 1b Processor
L2	Level 2
L2OP	Level 2 Operational Processor
L2PF	Level 2 Processing Facility
L2PP	Level 2 Prototype Processor
L2WG	Level 2 Working Group
LbL	Line-by-Line
LDOME	Linearized Discrete Ordinate Method with Matrix Exponential
LER	Lambertian Equivalent Reflectivity
LIDORT	Linearized Discrete Ordinate Radiative Transfer
LOA	Laboratoire d'Optique Atmosphérique
LUT	Look-Up Table
MAD	Mean Absolute Deviation
MAPE	Mean Absolute Percentage Error
MAX-DOAS	Multi-Axis DOAS
MERLIN	Methane Remote Sensing Lidar Mission
MetOp	Meteorological Operational Polar Satellites of EUMETSAT
MHS	Microwave Humidity Sounder
MIAWARA	Middle Atmospheric Water Vapour Radiometer

MIPAS	Michelson Interferometer for Passive Atmospheric Sounding
MIRART	Modular Infrared Atmospheric Radiative Transfer
MODIS	Moderate Resolution Imaging Spectroradiometer
MODTRAN	MODerate resolution atmospheric TRANsmission
MOME	Matrix Operator with Matrix Exponential
MOZART	Model for Ozone and Related Chemical Tracers
MPC	Mission Performance Center
MPIC	Max-Planck Institut für Chemie
MT-CKD	MlawerTobinCloughKneizysDavies
MTG	Meteosat Third Generation
MTG-S	Meteosat Third Generation Sounder
NDACC	Network for the Detection of Atmospheric Composition Change
netCDF	Network Common Data Format
NIR	Near-Infrared
NISER	National Institute of Science Education and Research
NNLS	Non-Negative Least Squares
NRT	Near-realtime
NSO	Netherlands Space Office
NMVOC	Non-Methane Volatile Organic Compounds
OCRA	Optical Cloud Recognition Algorithm
OEM	Optimal Estimation Method
OLS	Ordinary Least Square
OMI	Ozone Monitoring Instrument
OMNO2	OMI NO2
OZA	Observation Zenith Angle
PCA	Principal Component Analysis
PBLH	Planetary Boundary Layer Height
PDGS	Payload Data Ground Segment
PDR	Preliminary Design Review
PSTAR	Vector Radiative Transfer Model
QBO	Quasi-Biennial Oscillations
QC	Quality Controlled
RA	Reference Area
RAA	Relative Solar Azimuth Angle
RAL	Rutherford Appleton Laboratory
RGB	Red/Green/Blue
RH	Relative Humidity
RI	Relative Light Intensity
RMSE	Root Mean Square Error
ROCINN	Retrieval of Cloud Information using Neural Networks
RT	Radiative Transfer
rTCA	Reverse TCA
RTM	Radiative Transfer Model
S4	Sentinel-4
S4L2	Sentinel-4 Level 2
S5	Sentinel-5
S5P	Sentinel-5 Precursor
S&T	Science & Technology Corporation
SAF	Satellite Application Facility
SBUV	Solar Backscatter Ultraviolet Radiometer
SCD	Slant Column Density
SCIAMACHY	Scanning Imaging Absorption Spectrometer for Atmospheric Chartography
SCIATRAN	Radiative transfer model for SCIAMACHY
SEOM	Scientific Exploitation of Operational Missions
SEOM-IAS	SEOM Improved Atmospheric Spectroscopy
SG	Second Generation

SHDOM	Spherical Harmonic Discrete Ordinate Method
SMILES	Superconducting Sub-Millimeter Wave Limb Emission Sounder
SOST	SCIAMACHY Operations Support Team
SQWG	SCIAMACHY Quality Working Group
SRON	Netherlands Institute for Space Research
STREAM	Stratospheric Estimation Algorithm from Mainz
SRTM	Stochastic Radiative Transfer Model
Suomi-NPP	Suomi National Polar-orbiting Partnership
SWIR	Short-Wave Infrared
SZA	Sun Zenith Angle
TCA	Tricarboxylic Acid
TCCON	Total Carbon Column Observing Network
TELIS	Terahertz and Submillimeter Limb Sounder
TM5-MP	Global Chemistry Transport Model
TNO	Toegepast Natuurwetenschappelijk Onderzoek (Netherlands Organization for Applied Scientific Research)
TOMS	Total Ozone Mapping Spectrometer
TROPOMI	Tropospheric Monitoring Instrument
TWR	Temporal Weighted Regression
UAV	Unmanned Aerial Vehicle
UCPH	University of Copenhagen
UFS	Umweltforschungsstation Schneefernerhaus
UK	United Kingdom
UPAS	Universal Processor for UV/VIS Atmospheric Spectrometers
URD	User Requirements Document
UV	Ultraviolet
UVN	UV-VIS-NIR
VCD	Vertical Column Density
VDDA	VirES Data Dictionary Aeolus
VIIRS	Visible Infrared Imaging Radiometer Suite
VirES	Virtual Workspace for Earth-Observation Scientists
VIS	Visible
VLIDORT	Vector model LIDORT
WOUDC	World Ozone and UV Data Center
WRF	Weather Research & Forecasting
WS	Wind Speed

## DLR at a Glance

DLR is the national aeronautics and space research center of the Federal Republic of Germany. Its extensive research and development work in aeronautics, space, energy, transport and security is integrated into national and international cooperative ventures. In addition to its own research, as Germany's Space Agency, DLR has been given responsibility by the federal government for the planning and implementation of the German space program. DLR is also the umbrella organization for the nation's largest project management agency.

Approximately 8000 people are employed at 20 locations in Germany: Cologne (headquarters), Augsburg, Berlin, Bonn, Braunschweig, Bremen, Bremerhaven, Dresden, Göttingen, Hamburg, Jena, Jülich, Lampoldshausen, Neustrelitz, Oberpfaffenhofen, Oldenburg, Stade, Stuttgart, Trauen and Weilheim. DLR has also offices in Brussels, Paris, Tokyo and Washington, D.C.

### Remote Sensing Technology Institute Institut für Methodik der Fernerkundung

DLR's Remote Sensing Technology Institute (IMF) is located in Oberpfaffenhofen, Berlin-Adlershof, Bremen and Neustrelitz.

IMF carries out research and development for retrieving geoinformation from remote sensing data. It conducts basic research on physical principles of remote sensing and develops algorithms, techniques, and operational processing systems for synthetic aperture radar, optical remote sensing, and spectrometric sounding of the atmosphere. The processing systems are in operational use for national, European, and international Earth observation missions.

For preparation and in support of space missions, IMF operates a suite of optical airborne sensors and laboratories. The institute contributes its expertise to novel sensor and mission concepts.

The German Remote Sensing Data Center (DFD) and IMF form DLR's Earth Observation Center (EOC).



DLR

**Deutsches Zentrum  
für Luft- und Raumfahrt e.V.**

in der Helmholtz-Gemeinschaft

**Institut für Methodik der Fernerkundung**

Oberpfaffenhofen  
82234 Weßling

[www.dlr.de/eoc](http://www.dlr.de/eoc)